7. SITE 931[1]

Shipboard Scientific Party[2]

HOLE 931A

Date occupied: 5 April 1994

Date departed: 5 April 1994

Time on hole: 11 hr, 15 min

Position: 5°8.511′N, 46°37.983′W

Bottom felt (drill pipe measurement from rig floor, m): 3483.4

Distance between rig floor and sea level (m): 10.71

Water depth (drill pipe measurement from sea level, m): 3472.7

Penetration (m): 53.60

Number of cores (including cores having no recovery): 6

Total length of cored section (m): 53.60

Total core recovered (m): 56.99

Core recovery (%): 106

Oldest sediment cored:
Depth (mbsf): 53.60
Nature: Silty clay
Earliest age: Pleistocene

HOLE 931B

Date occupied: 5 April 1994

Date departed: 10 April 1994

Time on hole: 4 days, 3 hr, 15 min

Position: 5°8.521′N, 46°37.984′W

Bottom felt (drill pipe measurement from rig floor, m): 3486.7

Distance between rig floor and sea level (m): 10.74

Water depth (drill pipe measurement from sea level, m): 3475.9

Penetration (m): 421.30

Number of cores (including cores having no recovery): 45

Total length of cored section (m): 421.30

Total core recovered (m): 296.05

Core recovery (%): 70

Oldest sediment cored:
Depth (mbsf): 421.30
Nature: Silty clay
Earliest age: Pleistocene

HOLE 931C

Date occupied: 10 April 1994

Date departed: 10 April 1994

Time on hole: 12 hr

Position: 5°8.531′N, 46°37.986′W

Bottom felt (drill pipe measurement from rig floor, m): 3485.4

Distance between rig floor and sea level (m): 10.87

Water depth (drill pipe measurement from sea level, m): 3474.5

Penetration (m): 32.60

Number of cores (including cores having no recovery): 4

Total length of cored section (m): 32.60

Total core recovered (m): 34.43

Core recovery (%): 105

Oldest sediment cored:
Depth (mbsf): 32.60
Nature: Silty clay
Earliest age: Pleistocene

Principal results: Site 931 (proposed Site AF-10) is the most easterly site to be drilled on the Amazon Fan. It is located on a flat terrace on the western levee of the buried Channel 5 system. The holes penetrate a thin acoustic unit interpreted as muds with minor turbidite silt overlying the Channel 5 system, then the thick Channel 5 levee sequence passing down into high-amplitude reflection packets (HARPs) interpreted as sandy lobes associated with channel avulsion. Three HARP units overlie a thick acoustically incoherent unit (interpreted as a debris flow) that laps out to the west against the crest of the unusually thick Bottom Levee Complex.

The site was selected from a *Ewing* seismic profile (E9209; 1637UTC on 20 Sept.). Following Site 930, we ran a 12-hr seismic survey across proposed Sites 940, 932, 933, and 931.

Hole 931A was cored to 53.6 mbsf and recovered 56.99 m. Hole 931B was cored by advanced piston corer (APC) to 76.8 mbsf, then by extended core barrel (XCB) to 421.3 mbsf. Recovery was poor from 142.2 to 219.1 mbsf (15.6%) in alternating sand and mud. Total hole recovery was 296.1 m (70.3%). Temperature measurements were obtained using the ADARA at 67.3 mbsf, and using the WSTP at 103.5 mbsf and 142.2 mbsf, yielding a mean geothermal gradient of 34°/km. There was gas expansion in many cores. Methane was found throughout the hole, with a sharp increase at 10 mbsf, and peaks at about 50 mbsf and 400 mbsf. Only trace amounts of ethane and propane were detected in a few deep cores.

Because some pipe had to be raised to retrieve a stuck core barrel, Hole 931B was conditioned for logging prior to taking the final two cores. On the first logging run, the sonic and natural gamma tools of the Quad combo flooded. They were replaced, and the tool was run to 251 mbsf where a bridge prevented further passage downhole. The hole was logged from 251 to 90 mbsf, the pipe was raised to 72 mbsf, and the interval 150 to 72 mbsf was logged. A similar procedure was used on subsequent log runs with the FMS, geochemical, and GHMT combinations. Hole condi-

[1]Flood, R.D., Piper, D.J.W., Klaus, A., et al., 1995. *Proc. ODP, Init. Repts.*, 155: College Station, TX (Ocean Drilling Program).

[2]Shipboard Scientific Party is as given in the list of participants in the contents.

tions were good, except in a few parts of the interval from 140 to 240 mbsf, where sand beds had washed out. Hole 931C was then cored to 32.6 mbsf and recovered 34.43 m (105.6% recovery).

Five lithologic units are recognized:

Unit I (0–0.57 mbsf) is a Holocene nannofossil- and foraminifer-rich clay that is bioturbated and contains about 50% carbonate.

Unit II (0.57–189.63 mbsf) consists of mud with interbedded laminae and beds of silt and very fine sand. The mud contains about 3% carbonate. Subunit IIA (0.57–6.70 mbsf) comprises bioturbated and color-banded mud. Subunit IIB (6.70–27.50 mbsf) consists of mud with <20% silt laminae. These two subunits represent sediment that accumulated since the abandonment of Channel 5. Subunit IIC (27.50–199.20 mbsf), corresponding to the crest of the Channel 5 levee, contains mud with thin to thick beds of silt and fine sand, which increase in frequency and thickness toward the base of the subunit. The thickest sand beds contain mud clasts. Recovery was low in the lower 70 m of Subunit IIC and included abundant sand beds, equivalent to the seismically identified HARPs. Logging indicated two major sequences of upward-diminishing sand abundance (fining-upward cycles), with their bases at 198 mbsf and 158 mbsf. Individual sand packets up to several meters thick appear to be separated by muddier units at the base of these cycles. Sand in the lower cycle includes abundant wood fragments.

The upper part of Unit III (199.8–257.7 mbsf) appears to correlate with the lowest HARP in the seismic data. Recovery in this interval was low, consisting of muddy sand, containing some mud clasts, alternating with mud containing silt laminae. Most of this interval was logged and apparently consists of alternating sand and mud. Core-catcher samples contain bathyal benthic foraminifers (*Bolivina striata*) from the continental slope to a water depth of 2000 m, which suggests a reworked component in Unit III.

The lower part of Unit III (257.8–349.25 mbsf) consists of various types of overconsolidated mud, in places clearly occurring as clasts, some of which consist of foraminifer- and nannofossil-rich clay. Benthic foraminifers in this part of the unit are deep-water taxa such as *Uvigerina*. The lower part of the unit is interpreted as a mud-clast conglomerate deposited by one or more debris flows.

Unit IV (349.25–349.46 mbsf) consists of a highly bioturbated dark gray (10Y 4/1) foraminifer-nannofossil-bearing clay with <35% carbonate.

Unit V (349.46–421.3 mbsf) consists of a sequence similar to Subunits IIA and IIB, with bioturbated and color-banded mud (Subunit VA, to 360.87 mbsf) overlying mud with silt laminae (Subunit VB). This unit is correlated with a levee in the Bottom Levee Complex.

Foraminifers are rare except in Units I (Holocene) and IV. In Unit IV and the upper 5 m of Unit V, the foraminiferal assemblage is an interglacial assemblage between 0.1 and 0.43 Ma. The nannofossils are Zone CN14b (0.26–0.46 Ma). The lowermost clasts in the debris flow (Unit III) have interglacial microfossil assemblages similar to those in the underlying Units IV and V. Higher in Unit III are clasts with a CN15a nannofossil assemblage. The Lake Mungo Excursion was detected at 76.5 mbsf. The first *P. obliquiloculata* below the Holocene occurred at 238.4 mbsf, in the upper part of Unit III, where it may be reworked. However, foraminifer abundances are very low from 90 to 238 mbsf, so the *P. obliquiloculata* zonal marker (40 ka) may not have been detected.

A detailed pore-water profile was made in Hole 931C from 0 to 32 mbsf by taking one sample per 1.5 m. A pronounced peak in alkalinity and phosphate occurs at 6 mbsf, with phosphate decreasing to background values by 10 mbsf, just below the limit of sulfate reduction. Pore-water iron peaks at 12–16 mbsf. These distributions suggest that once iron is no longer removed as sulfide, it is precipitated as vivianite (iron phosphate), which forms small blue microcrystalline nodules. High total sulfur values are found in sediment at 12–15 mbsf. Total organic carbon averages 1.0% in the upper part of the hole, decreasing to about 0.8% near the base of the hole.

Downhole variations in mud mineralogy (determined by XRD) show much scatter and are difficult to interpret because of grain size effects. Higher kaolinite/illite ratios occur in places in Unit II between 30 and 100 mbsf, in a carbonate clay clast in Unit III, and in Unit V.

Magnetic susceptibility data show a small-scale correlation with silt-mud alternations, but also show a longer period variation over tens of meters. These correlate with variations in illite to quartz ratio from XRD data. Susceptibility measured with the GHMT logging tool shows a strong correlation with log indicators of sand/mud ratio such as natural gamma and aluminum.

Units I and II show variations in porosity and bulk density that suggest normal consolidation. Many of the blocks in Unit III appear overconsolidated. Unit V shows profiles that suggest normal consolidation, but the water content of this sediment is rather high for the depth of burial, which may indicate that the debris flow inhibited dewatering. Within Subunit IIC, at least three cycles of variation in resistivity, probably related to sediment fabric, can be distinguished.

The preliminary data from Site 931 indicate that the Bottom Levee Complex (Unit V) is of middle Pleistocene age. The lower part of the debris-flow deposit (Unit III) contains no material diagnostic of an upper slope or shelf source. The presence of deep-water benthic foraminifers suggests that it may have originated by local failure of the deep levee or levees of an adjacent channel. The upper part of Unit III and the lower part of Subunit IIC are correlated with three HARPs in the seismic reflection profile. The logging data suggest that the HARPs consist of the sandy parts of fining-upward sequences and comprise packets of sand up to several meters thick separated by thinner mud.

SETTING AND OBJECTIVES

Introduction

Site 931 (proposed Site AF-10) was intended to provide a long biostratigraphic section on the southeastern margin of the Amazon Fan and to sample the Bottom Levee Complex at about 370 mbsf. It was also the first site to drill through sandy units (HARPs) at the base of a levee. Obtaining logs from the hole was a high priority because of its long stratigraphic section and the presence of several characteristic acoustic facies.

Setting

Site 931 is the most easterly site drilled during Leg 155. It is located on a flat terrace on the western (left) levee of Channel 5 about 1 km from the channel (Figs. 1 and 2). This terrace may have been formed by the cutoff of a meander loop. The age of Channel 5 is uncertain from seismic profiles, but it appears to immediately pre-date the Yellow Channel-levee System in the central part of the fan. Channel 5 may originate at a place on the continental slope different from the modern Amazon Canyon.

The site was selected from a *Ewing* seismic profile (E9209; 1637UTC on 20 Sept.). High-resolution seismic data for the upper 0.5 s were obtained from the Leg 155 *JOIDES Resolution* pre-site survey (Fig. 3).

The surficial sediment at the site, interpreted from 3.5-kHz subbottom profiles, shows a surface drape of acoustically stratified sediment about 16 ms thick overlying a more reflective unit, 12 ms thick, that thickens toward the channel (Fig. 2). The seismic reflection data show, below this unit, a thick interval of levee-crest strata (about 160 ms thick) associated with the Channel 5 system (Fig. 3). This overlies a unit of high-amplitude subparallel reflections, termed a high-amplitude reflection package (HARP) by Manley and Flood (1988) and Flood et al. (1991), that may represent sandier deposits formed in the early stages of channel avulsion before progradation of a new channel-levee complex. Multiple HARP units were predicted because three channels lie close to one another at this site. The HARP units overlie a thick acoustically incoherent unit with surface hyperbolic diffractions (interpreted as a debris flow) that laps out to the west

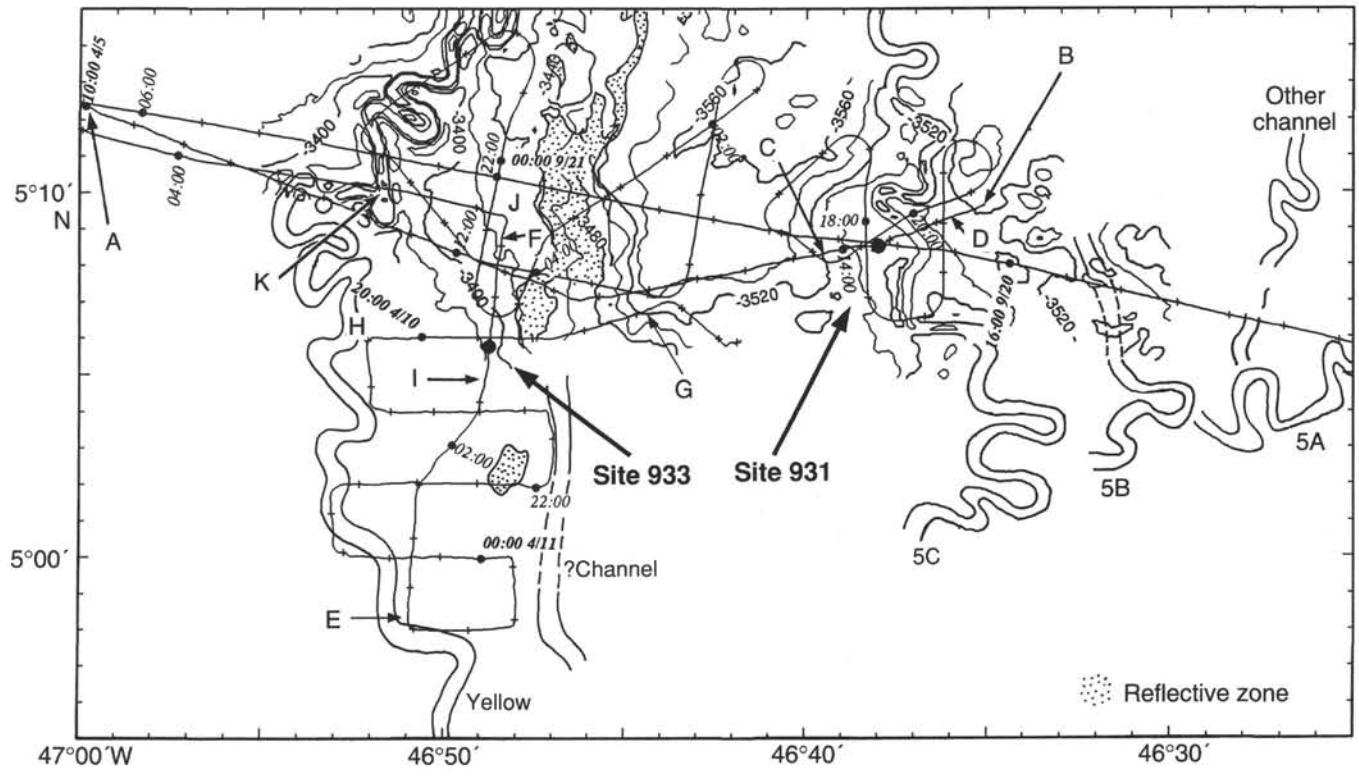

Figure 1. Location of Sites 931 and 933 showing *JOIDES Resolution* and other seismic tracks. Bathymetry from Flood et al. (1991) and from *Ewing* cruise 9209. A–B is seismic profile in Fig. 3. C–D is 3.5-kHz profile in Fig. 2. E–F and G–H are seismic profiles in Fig. 2 of "Site 933" chapter (this volume). I-J-K is 3.5-kHz profile in Fig. 1 of "Site 933" chapter. Channels are based on GLORIA sidescan sonar images (Damuth et al., 1988). The reflective zone is observed on GLORIA images.

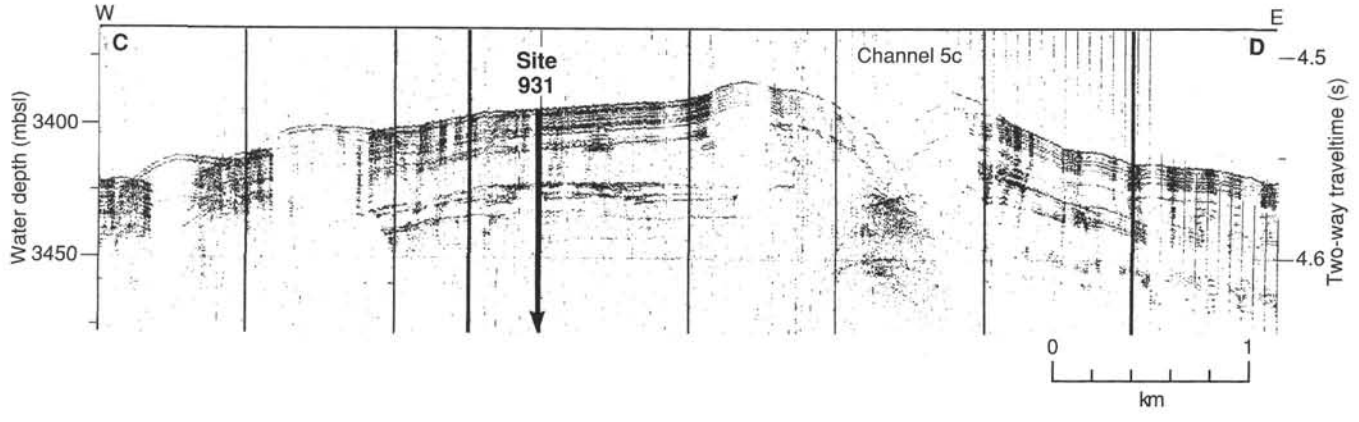

Figure 2. A 3.5-kHz profile through Site 931.

against the crest of the Bottom Levee Complex. It is unusually thick, showing more than 500 ms of channel aggradation, compared with the 300-ms thickness of typical channel-levee systems observed in the Upper and Lower Levee complexes in similar water depths. The crestal sediment of this deep levee was sampled at Site 933.

Objectives

The principal objectives at Site 931 were:

1. To sample the anticipated hemipelagic section above the Channel 5 levee as a biostratigraphic and paleomagnetic reference section.
2. To date the Bottom Levee Complex.
3. To stratigraphically sample the expanded section in the Channel 5 levee. This is the only site planned to penetrate this expanded interval.
4. To characterize facies in the crest of a levee system.

Secondary objectives include characterizing and sampling the HARP at the base of the Channel 5 levee and a possible debris flow below the Channel 5 levee.

The logging objectives were to characterize the various acoustic facies by their log response and to obtain geochemical and magnetic susceptibility profiles of the entire section. It was expected that these might show changes in the mineralogy of the detrital load reaching the fan, reflecting climatic change on land.

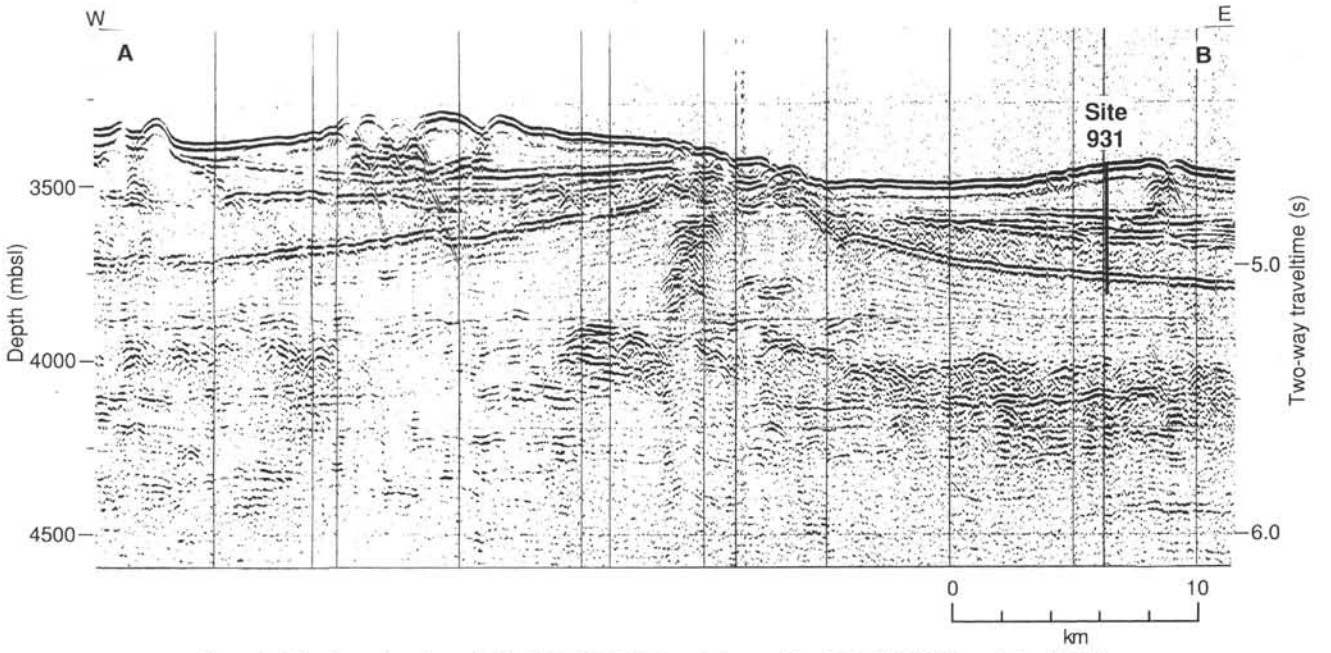

Figure 3. Seismic section through Site 931. (*JOIDES Resolution* profile, 1000–1437 UTC on 5 April 1994).

OPERATIONS

Seismic Survey: Site 930 to Site 931 (AF-10)

At 2136 hr 4 April, we began a seismic-reflection survey from Site 930, over proposed sites AF-6, -8, -19, -11, and -9 and -10. The survey lasted about 12 hr.

Hole 931A

After the seismic gear was retrieved, the ship returned to the GPS coordinates 05°08.529′N, 46°37.981′W, and we dropped a beacon at 1203 hr 5 April. We assembled a bottom-hole assembly (BHA) similar to that used at Site 930 and ran the bit to the seafloor. Depending on the ship's draft, the distance from sea level to rig floor was approximately 10.71 m for Hole 931A, 10.74 m for Hole 931B, and 10.87 m for Hole 931C. The 3.5-kHz depth recorded indicated a depth of 3489.4 mbrf.

We positioned the bit at 3480.0 mbrf, and Hole 931A was spudded at 1820 hr 5 April. Core 1H recovered 6.15 m of sediment (Table 1). The mud line was then defined to be 3483.4 mbrf. Cores 1H through 6H were taken from 3483.4 to 3537.0 mbrf (0–53.6 mbsf) with 53.6 m cored and 56.99 m recovered (106%). In most of the cores recovered at Site 931, sediment began to extrude from the core liner due to gas expansion once the liner was taken out of the core barrel. Core disturbance was minimized by drilling small holes in nearly all of the core liners to allow gas to escape. During APC coring, several core liners collapsed, in some cases significantly disturbing the recovered sediment.

Hole 931B

We moved the ship 20 m to the north and spudded Hole 931B at 2345 hr 5 April. The bit was positioned at 3478.0 mbrf and Core 1H recovered 0.84 m of sediment. The mud line was defined to be at 3486.7 mbrf. Cores 1H through 9H were taken from 3486.7 to 3563.5 mbrf (0–76.8 mbsf) with 76.8 m cored and 82.97 m recovered (108.0%). We used the Tensor tool for core orientation on Cores 3H through 9H and the ADARA temperature shoe while taking Cores 6H and 8H.

We then switched to XCB coring. XCB Cores 10X through 45X were taken from 3563.5 to 3908.0 mbrf (76.8–421.3 mbsf) with 344.5 m cored and 213.72 m recovered (62.0%). Although there is no reported recovery for Core 24X, there were a few small pieces of rock, and the small amount of sediment in the core catcher was taken for paleontological analysis. The combined APC/XCB recovery for Hole 931B was 70.4%. We used the WSTP temperature tool prior to Cores 11X, 13X, and 17X. During retrieval of the core barrel containing Core 43X, the barrel became stuck at 203 mbrf. The drill pipe with the stuck core barrel was pulled above the rig floor, removed from the drill string, and the core was retrieved.

Expansion of the cores due to gas sometimes resulted in core material being ejected from the core liner on the rig floor, resulting in severe core disturbance (especially Core 31X) and some loss of core material. Cores 17X, 18X, and 20X (142.2–180.7 mbsf) had no recovery despite drilling the interval with only minimal circulation. Hole 931B was logged above 250 mbsf, and the bit was pulled out of the hole, clearing the seafloor at 0230 hr 10 April.

Hole 931C

We moved the ship approximately 20 m to the north and spudded Hole 931C at 0359 hr 10 April. The bit was positioned at 3469.1 mbrf, and Core 1H recovered 4.1 m of sediment. The mud line was defined at 3474.5 mbrf. Cores 1H through 4H were taken from 0 to 32.6 mbsf, recovering 57.0 m of sediment (106%). The beacon was recovered, and the bit cleared the drill floor at 1430 hr 10 April.

LITHOSTRATIGRAPHY

Introduction

Three holes were drilled at Site 931 to a maximum depth of 421.3 mbsf: Hole 931A (0 to 53.6 mbsf), Hole 931B (0 to 421.3 mbsf), and Hole 931C (0 to 32.60 mbsf). Incomplete recovery, especially within Cores 931B-11X through -26X and Cores 931B-29X through -37X, limited our ability to determine precise unit boundaries (Figs. 4 and

Table 1. Site 931 coring summary.

Core	Date (1994)	Time (UTC)	Depth (mbsf)	Length cored (m)	Length recovered (m)	Recovery (%)
155-931A						
1H	April 5	2235	0.0–6.1	6.1	6.15	101.0
2H	April 5	2330	6.1–15.6	9.5	9.95	105.0
3H	April 6	0010	15.6–25.1	9.5	10.24	107.8
4H	April 6	0055	25.1–34.6	9.5	10.30	108.4
5H	April 6	0130	34.6–44.1	9.5	10.37	109.1
6H	April 6	0225	44.1–53.6	9.5	9.98	105.0
Coring totals				53.6	57.0	106.30
155-931B-						
1H	April 6	0405	0.0–0.8	0.8	0.84	100.0
2H	April 6	0450	0.8–10.3	9.5	10.05	105.8
3H	April 6	0555	10.3–19.8	9.5	10.33	108.7
4H	April 6	0655	19.8–29.3	9.5	10.39	109.3
5H	April 6	0750	29.3–38.8	9.5	10.25	107.9
6H	April 6	0910	38.8–48.3	9.5	10.40	109.5
7H	April 6	1005	48.3–57.8	9.5	9.46	99.6
8H	April 6	1135	57.8–67.3	9.5	10.31	108.5
9H	April 6	1225	67.3–76.8	9.5	10.94	115.1
10X	April 6	1350	76.8–84.3	7.5	7.87	105.0
11X	April 6	1605	84.3–93.9	9.6	7.86	81.9
12X	April 6	1700	93.9–103.5	9.6	6.76	70.4
13X	April 6	1925	103.5–113.2	9.7	5.50	56.7
14X	April 6	2020	113.7–122.8	9.1	6.09	66.9
15X	April 6	2110	122.8–132.5	9.7	4.71	48.5
16X	April 6	2215	132.5–142.2	9.7	5.24	54.0
17X	April 7	0040	142.2–151.8	9.6	0.00	0.0
18X	April 7	0155	151.8–161.5	9.7	0.00	0.0
19X	April 7	0305	161.5–171.2	9.7	5.86	60.4
20X	April 7	0420	171.2–180.7	9.5	0.00	0.0
21X	April 7	0530	180.7–190.2	9.5	3.47	36.5
22X	April 7	0635	190.2–199.8	9.6	0.00	0.0
23X	April 7	0800	199.8–209.4	9.6	2.67	27.8
24X	April 7	0910	209.4–219.1	9.7	0.00	0.0
25X	April 7	1035	219.1–228.7	9.6	5.97	62.2
26X	April 7	1200	228.7–238.4	9.7	4.49	46.3
27X	April 7	1345	238.4–248.0	9.6	9.94	103.0
28X	April 7	1530	248.0–257.7	9.7	7.06	72.8
29X	April 7	1655	257.7–267.3	9.6	6.79	70.7
30X	April 7	1805	267.3–276.9	9.6	0.31	3.2
31X	April 7	2000	276.9–286.6	9.7	10.50	108.2
32X	April 7	2215	286.6–296.2	9.6	9.14	95.2
33X	April 8	0055	296.2–305.8	9.6	6.47	67.4
34X	April 8	0240	305.8–315.5	9.7	5.34	55.0
35X	April 8	0430	315.5–325.1	9.6	5.08	52.9
36X	April 8	0635	325.1–334.8	9.7	9.41	97.0
37X	April 8	0900	334.8–344.4	9.6	5.83	60.7
38X	April 8	1055	344.4–354.1	9.7	9.41	97.0
39X	April 8	1230	354.1–363.7	9.6	7.65	79.7
40X	April 8	1410	363.7–373.4	9.7	8.76	90.3
41X	April 8	1550	373.4–382.9	9.5	8.92	93.9
42X	April 8	1720	382.9–392.4	9.5	9.18	96.6
43X	April 8	2045	392.4–401.9	9.5	10.24	107.8
44X	April 9	0055	401.9–411.6	9.7	9.96	102.0
45X	April 9	0230	411.6–421.3	9.7	6.60	68.0
Coring totals				421.3	296.1	0.30
155-931C-						
1H	April 10	0825	0.0–4.1	4.1	4.14	101.0
2H	April 10	0910	4.1–13.6	9.5	9.83	103.0
3H	April 10	0955	13.6–23.1	9.5	10.31	108.5
4H	April 10	1045	23.1–32.6	9.5	10.15	106.8
Coring totals				32.6	34.4	105.60

Note: An expanded version of this coring summary table that includes lengths and depths of sections, location of whole-round samples, and comments on sampling disturbance is included on the CD-ROM in the back pocket of this volume.

5). Expansion of methane gas during core recovery commonly affected the sediment by disrupting the primary sedimentary structures in many silt and sand beds and by producing void spaces within many of the core sections. Rotary (XCB) drilling disturbance (biscuits) in Cores 931B-26X through -40X further hampered description and identification of lithology (see "Lithostratigraphy" section in the "Explanatory Notes" chapter, this volume).

The sequence recovered consists of a thin carbonate-rich section (Unit I) overlying color-banded and mottled clay and silty clay containing discrete laminae and thin beds of both silt and very fine sand (Unit II). This lithology, in turn, overlies an apparently chaotic assemblage of contorted sandy mud, silt, and clay units intercalated with presumed displaced mud blocks and clasts (Unit III). At the base of the chaotic assemblage at approximately 350 mbsf, another thin carbonate-rich interval (Unit IV) overlies color-banded and mottled silty clay containing silt laminae and thin beds (Unit V).

Description of Lithostratigraphic Units

Unit I

Intervals: 155-931A-1H-1, 0–57 cm; 155-931B-1H-CC (core is highly disturbed and exact unit thickness is uncertain); 155-931C-1H-1, 0–63 cm
Age: Holocene
Depth: 0–0.57 mbsf

Unit I consists of brown (10YR 5/3) calcareous clay containing foraminifers and nannofossils. The unit contains approximately 50% carbonate (see "Organic Geochemistry" section, this chapter) and is moderately bioturbated and shows slight color mottling throughout. The unit contains a distinctive brown (10YR 4/3) iron-rich crust (interval 155-931A-1H-1, 53–56 cm). Similar diagenetic crusts were analyzed previously and correlated throughout the Amazon Fan and adjacent Guiana Basin (e.g., Damuth, 1977; see "Introduction" chapter, this volume). The base of Unit I is marked by a distinctive color change from brown (10YR 5/3) to olive gray (5Y 4/2) at 0.57 mbsf (interval 931A-1H, 57 cm).

Unit II

Intervals: 155-931A-1H, 57 cm, through -6H-CC, 15 cm (bottom of the hole); 155-931B-2H-1, 0 cm, through -23X-1, 0 cm (top of unit not preserved); 155-931C-1H, 63 cm, through -4H-CC, 26 cm (bottom of hole)
Age: late Pleistocene–Holocene
Depth: 0.57–199.80 mbsf

Unit II consists of terrigenous clay, silty clay, silt, and very fine sand. The sediment ranges in color from olive gray (5Y 4/2) to very dark gray (5Y 3/1). Distinct black (N1) color banding, mottling, and soft micronodules (less than 1 mm diameter and that commonly appear in burrow fills) are common throughout much of Unit II. The dark color banding and mottling are not grain-size related, but are caused by diagenetic hydrotroilite, which imparts an ephemeral black color to the sediment (see "Introduction" chapter, this volume). The base of Unit II is arbitrarily placed at the first occurrence (top) of a sequence that includes a muddy sand unlike the material recovered in Unit II. Wireline log Unit 3 (182–220 mbsf; "Downhole Logging" chapter, this volume) is interpreted to contain sand-rich intervals unlike Unit II, so the actual base of this unit may be closer to 184 mbsf, which is the top of a 15-m interval of no recovery (Fig. 4).

Unit II has been subdivided into three subunits based on the frequency of silt laminae and thin to thick beds of silt and very fine sand. The carbonate content of Unit II decreases from a maximum of 14.7% near the top of Subunit IIA (Sample 931A-1H, 64–65 cm) to values of about 1% or less throughout the rest of the unit.

Subunit IIA

Subunit IIA extends from the base of Unit I at 0.57 mbsf to a depth of 6.70 mbsf (from Section 931A-1H-1, 57 cm, through -2H-1, 60 cm). The unit consists of dark olive gray (5Y 3/2) slightly to moderately bioturbated, mottled, and color-banded clay. Carbonate content is elevated only in the upper tens of centimeters.

Subunit IIB

Subunit IIB extends from 6.70 to 27.50 mbsf (from Section 931A-2H-1, 60 cm, through -4H-2, 90 cm) and is characterized by dark olive gray (5Y 3/1 to 5Y 3/2) silty clay with subtle light and dark color

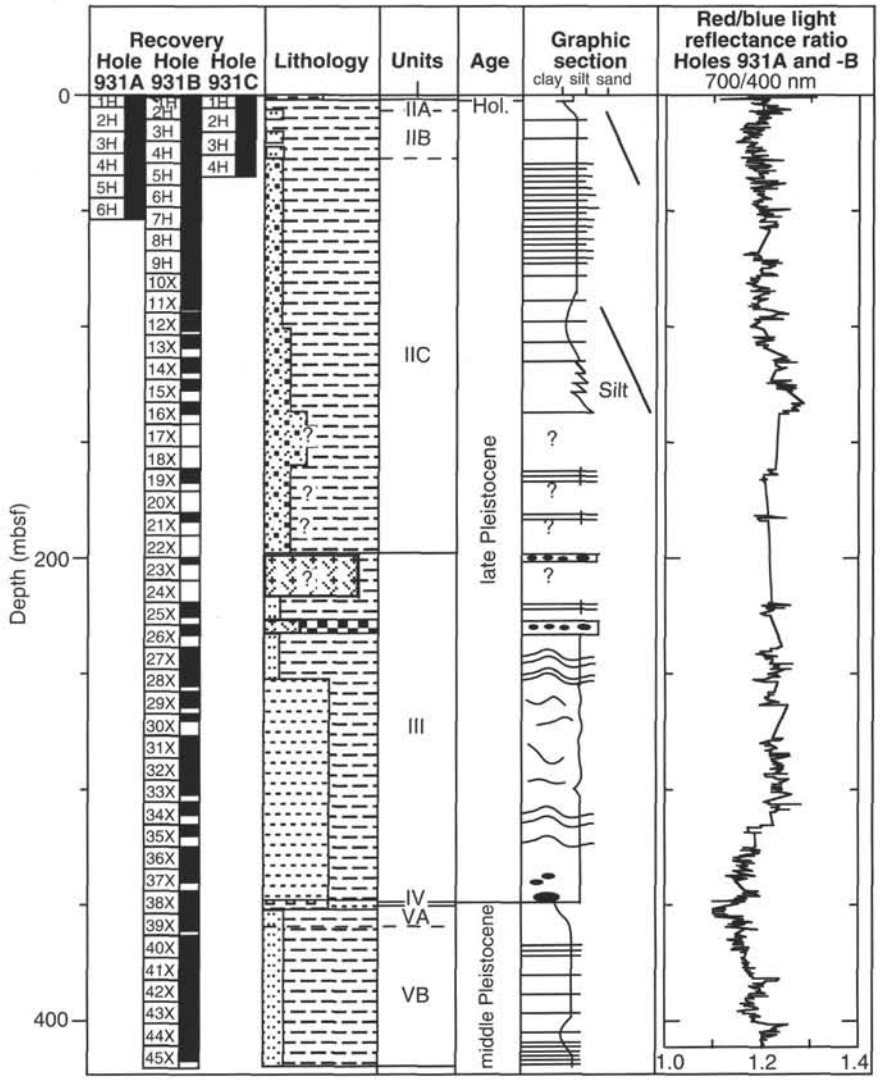

Figure 4. Composite stratigraphic section for Site 931 showing core recovery in all holes, simplified summary of lithology for Hole 931B, depths of unit boundaries, age, a graphic section with generalized grain-size and bedding characteristics, and downhole variations in light-reflectance values. The lithologic symbols are explained in Figure 1 of "Explanatory Notes" chapter, this volume.

bands. The contacts between the lighter and darker elements of the color bands are gradational and undulatory on a millimeter scale. Couplets of lighter and darker bands are about 0.5–1.0 cm thick. The laminae make up less than 20% of Subunit IIB. Mottling decreases downward throughout this subunit. The subdivision between Subunit IIA and IIB is the uppermost occurrence of silt laminae.

Subunit IIC

Subunit IIC extends from 27.50 to 199.80 mbsf (from Section 931A-4H-2, 90 cm, through 931B-23X-1, 0 cm) and consists primarily of dark olive gray (5Y 3/1 to 5Y 3/2) silty clay. The transition from Subunit IIB to IIC is placed at the uppermost occurrence of thin beds of silt and very fine sand. The silty clay contains color bands (Fig. 6) and intercalated laminae of silt and thin to thick beds of silt and very fine sand. The intensity and frequency of the color banding decreases with depth in the subunit, though it does not disappear completely. Mottling decreases with depth, and is absent from sediment recovered from 113.7 mbsf to the bottom of the subunit at 199.80 mbsf (interval 931B-14X-1, 0 cm, through -23X-1, 0 cm).

Some of the silt and sand beds exhibit parallel lamination, and a few display cross-lamination. Many beds are normally graded into overlying silty clay. Based on their sequences of primary sedimentary structures, these are either Bouma T_{bde} or T_{cde} turbidite beds. The thick beds tend to be massive (possibly as a result of gas expansion) and consist of well-sorted silt (Fig. 7A). Two beds are thicker than 1 m (Core 931B-16X; Fig. 5). Some of the thick beds contain mud clasts, 1–2 cm in diameter (Fig. 7B).

The frequency of laminae and beds of silt and sand are best illustrated by Figure 5. From 27.5 to 85.0 mbsf, there are no apparent trends in bed thickness or abundance. From 85.0 to 100.0 mbsf, color-banded silty clay and clay predominate over laminae and graded beds of silt and sand. From 100.0 to 137.5 mbsf, there is a fining- and thinning-upward sequence from thickly bedded, normally graded silt at the lower limit of recovery in this interval to thinly bedded and laminated silt and very fine sand and color-banded silty clays at the top. The base of the fining-upward sequence occurs in the interval 137.5–160.0 mbsf, but was not recovered.

Unit III

Intervals: 155-931B-23X-1, 0 cm, through -38X-4, 35 cm
Age: late Pleistocene
Depth: 199.80–349.25 mbsf

Unit III consists of muddy sand, silty clay, and clay. The upper limit of this unit is defined by the first occurrence of muddy sand (at interval 931B-23X-1, 20 cm). This upper contact is situated at the base of a 15-m interval of no recovery. Only 2.67 m of sediment was recovered in Core 931B-23X, and Core 931B-24X was empty except for some sandy mud containing a few indurated fragments lodged in

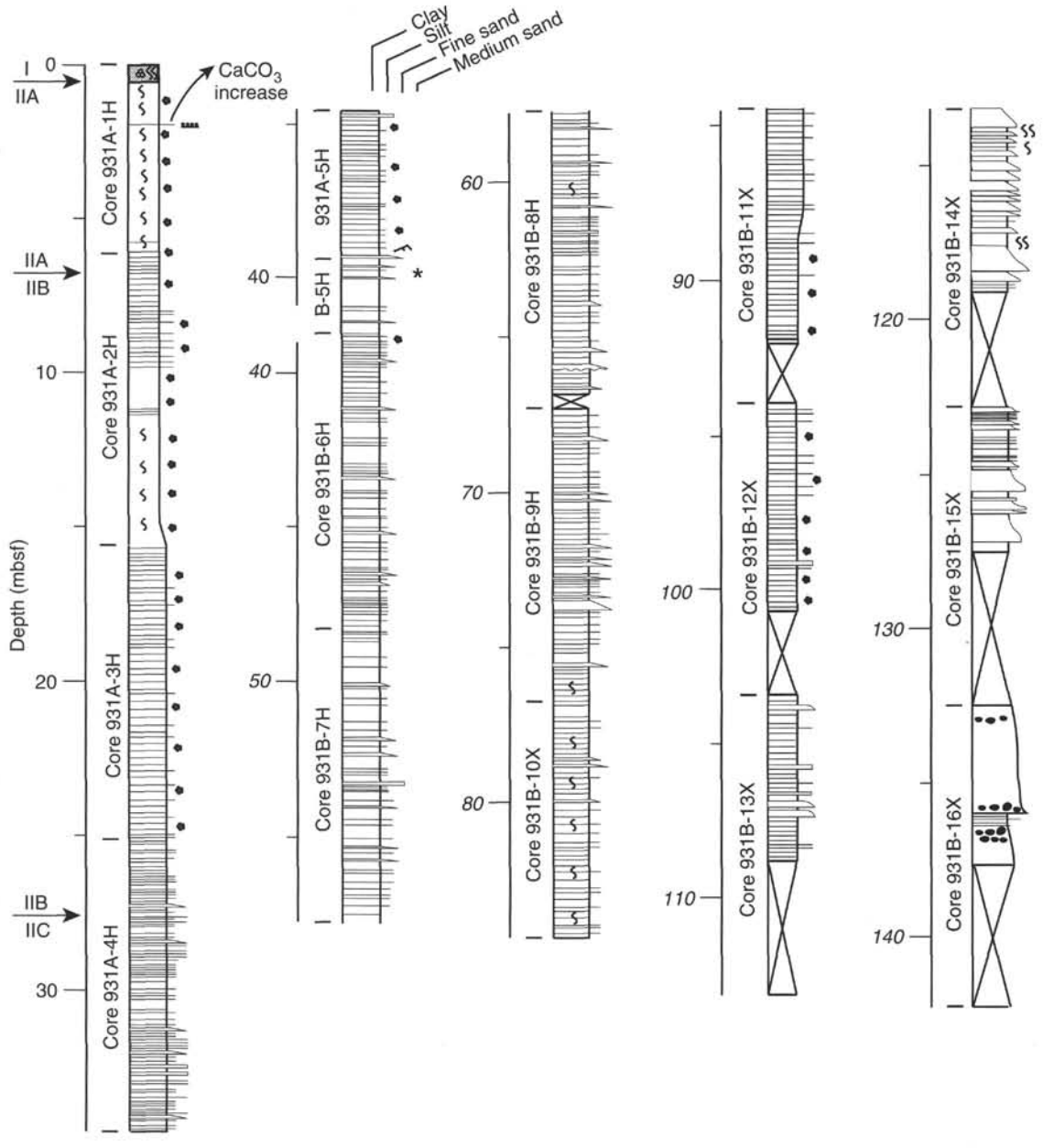

Figure 5. Graphic sedimentological columns for Site 931 showing grain-size variation (width of columns), bed thickness, and sedimentary structures; symbols and preparation of these columns are explained in the "Lithostratigraphy" section of the "Explanatory Notes" chapter, this volume. Arrows indicate the position of unit and subunit boundaries. The upper part of the column is shown in strike section of the foldout (back pocket, this volume) for comparison of levee sequences on the middle and upper fan. The columns are based on Holes 931A and 931B. The shallowest positive tie between Holes 931A and 931B is a distinctive sand bed base (* in the figure) at 36.9 mbsf in Hole 931B (interval 155-931B-5H-6, 84 cm), which correlates with the base of the same bed at a depth of 39.8 mbsf in Hole 931A (interval 155-931A-5H-4, 69 cm). The depth discrepancy is accounted for in this figure by using two offset depth scales (roman font for Cores 931A-1H through -5H; *italic font* for Cores 931B-5H through -45X).

the core catcher. A thin section cut from one of these fragments revealed carbonate-cemented, laminated silty clay similar in lithology to sediment in Core 931B-25X.

The sediment recovered from Unit III includes very dark gray (5Y 3/1) sandy mud with scattered 0.5- to 1-cm mud clasts (interval 931B-23X-1, 20 cm, through -23X-2, 95 cm; and 931B-26X-1, 24 cm, through -28X-CC, 5 cm). Some of the sandy mud intervals display contorted bedding (Cores 931B-27X and -28X). Dark gray (5Y 3/1) silty clays containing laminae and thin beds of silt and very fine sand (Fig. 8) alternate with the sandy mud intervals.

The interval 931B-29X-1, 72 cm, through -38X-4, 35 cm, consists of dark gray (5Y 3/1 to 5Y 3/2), faintly color-banded, mottled (?bioturbated) and highly contorted silty clay and clay (Fig. 9). Mud and carbonate-rich clasts, 2 to 25 cm in thickness, are intercalated within this lithology (Fig. 10). A sharp contact at the base of a 14-cm-long, dark-colored, apparent mud clast marks the base of Unit III at 349.5 mbsf (Fig. 11). Low sediment recovery precludes subdivision of Unit III.

Unit IV

Intervals: 155-931B-38X-4, 35 cm, through -4, 56 cm
Age: middle Pleistocene
Depth: 349.25–349.46 mbsf

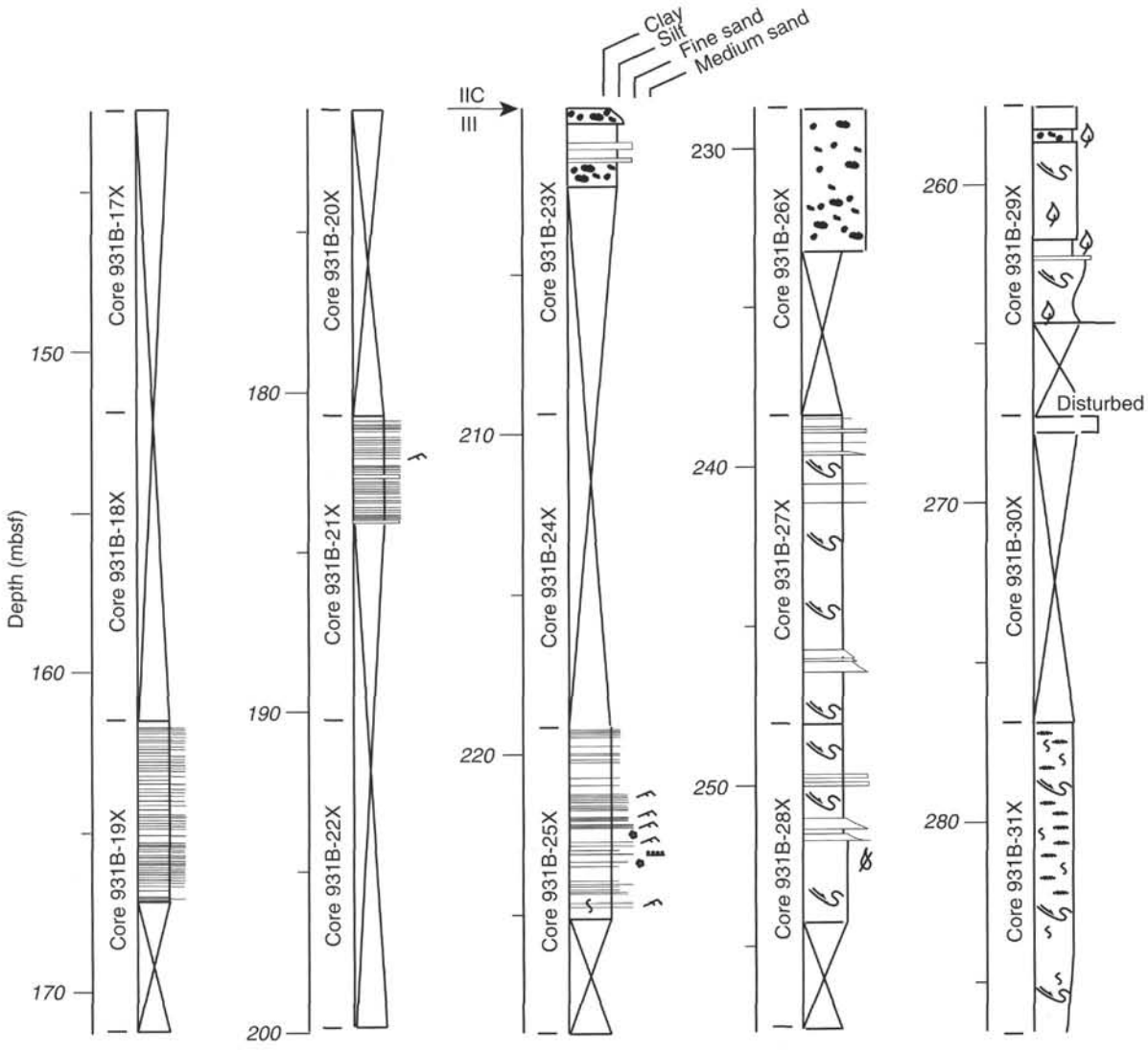

Figure 5 (continued).

Unit IV consists of an intensively bioturbated, dark gray (10Y 4/1) foraminifer-nannofossil-rich clay. The upper boundary of this unit is marked by its sharp contact with the dark-colored (?)mud clast at the base of Unit III at 349.25 mbsf. The lower boundary is at 349.46 mbsf (interval 155-931B-38X-4, 56 cm) where there is a gradation in color (10Y 4/1 to 5Y 3/1) and a lithologic transition from clay to silty clay. The entire unit is shown in Figure 11 and contains a maximum of approximately 20% carbonate (Sample 931B-38X-4, 40–41 cm).

Unit V

Intervals: 155-931B-38X-4, 56 cm, through -45X-CC, 30 cm
Age: middle Pleistocene
Depth: 349.46–418.10 mbsf

Unit V consists of faintly mottled, slightly bioturbated and color-banded, very dark gray (5Y 3/1) silty clay with silt laminae and thin (approximately 1 cm thick) silt beds (Fig. 12). The upper limit of this unit is the first appearance of silty clay below Unit IV. Some of the silt beds are normally graded. This unit, which is the lowermost at this site, has been subdivided into two subunits on the basis of the occurrence of silt laminae and beds.

Subunit VA

Subunit VA extends from 349.46 to 360.87 mbsf (from Section 931B-38X-4, 56 cm, through -39X-5, 77 cm) and consists of faintly mottled and color banded, very dark gray (5Y 3/1) silty clay (Fig. 2).

Subunit VB

Subunit VB extends from 360.87 mbsf to 418.10 mbsf (from Section 931B-39X-5, 77 cm, through -45X-CC) and is identified by the uppermost occurrence of silt laminae below Unit IV (Fig. 5). The subunit consists of very dark gray silty clay containing silt laminae and thin (1 cm thick) silt beds. Some of the beds are graded, but in general, the narrow range of silt size hampers visual recognition of subtle grading.

Mineralogy

Smear-slide Synthesis

Laminae and thin beds of coarse silt to fine sand in Unit II consist of well-sorted, angular to subangular grains of quartz (25%–50%), feldspar (5%–20%, mainly plagioclase), and accessory minerals (5%–15%). Terrigenous accessory minerals include common micas,

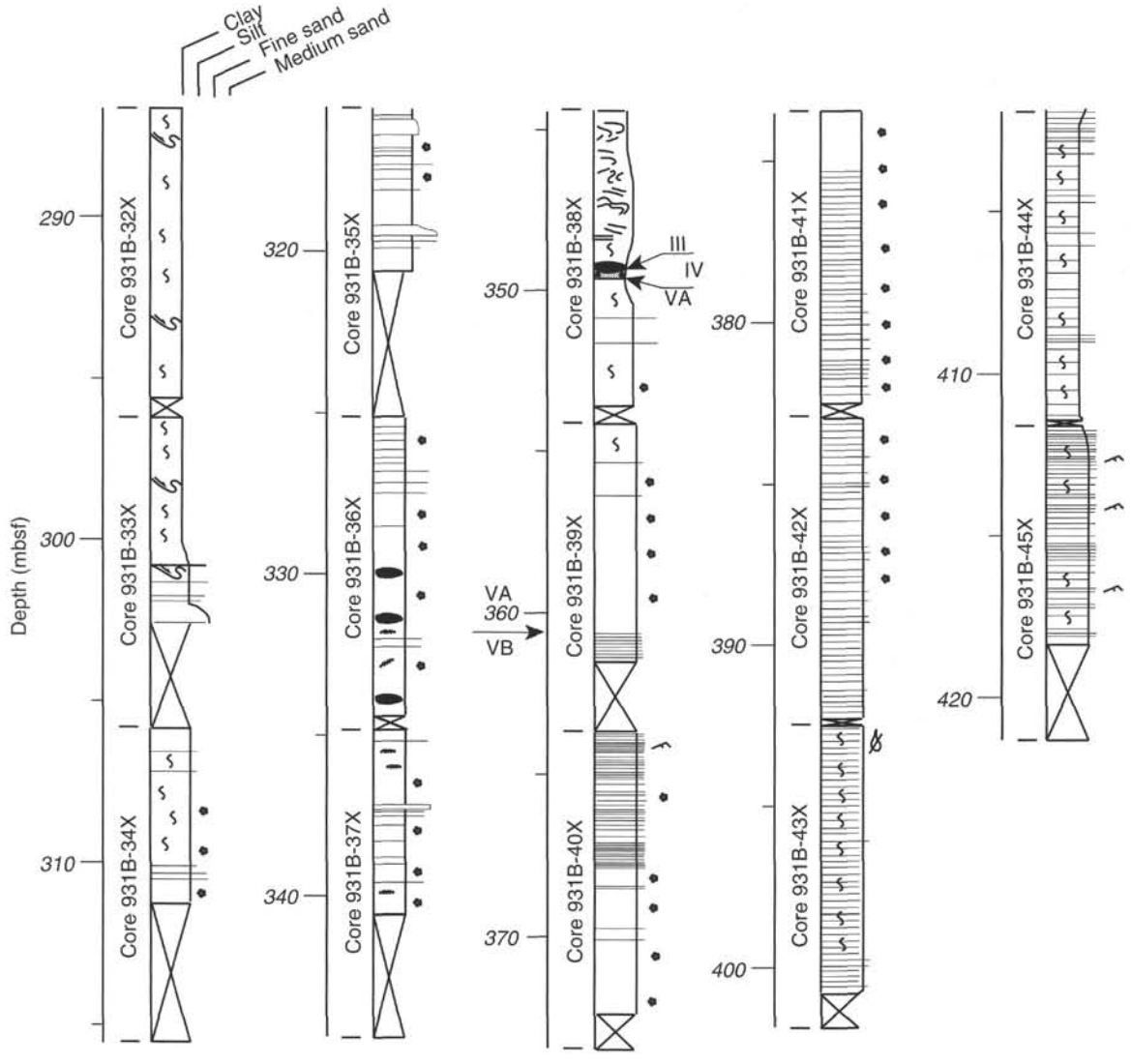

Figure 5 (continued).

hornblende and pyroxene, and minor zircon, spinel, and monazite. Diagenetic accessory minerals include widespread black hydrotroilite and blue-green vivianite. Except for Units I and IV, biogenic components are rare and consist of rare planktonic foraminifers. Small pieces of wood and shell fragments occur in Unit III.

X-ray Diffraction

X-ray diffraction analysis was performed on a bulk sample of the dominant lithology from most cores recovered at Site 931 (Table 2). The most abundant minerals throughout the section are quartz, plagioclase, augite, and the clay minerals smectite, illite (+mica) and kaolinite. Quartz has the highest peak intensity. A few samples contain K-feldspar, calcite, and hornblende. Sample 931B-37X-4, 40–41 cm, with the highest relative peak intensity for calcite of any sample, was taken in an interval with drilling deformation, but is probably from a clast. When normalized to the intensity of the primary quartz peak, all clay minerals irregularly decrease in relative abundance from the seafloor to Core 931B-16X at about 135 mbsf, and then increase in relative abundance from Core 931B-28X (about 250 mbsf) to the base of the hole at about 420 mbsf (Fig. 13). Ratios of clay minerals vary in an unsystematic way, with the largest fluctuations being in the ratio of illite (+ mica) to the other clays.

Spectrophotometry

Reflectance was very low throughout the sediment column recovered at Site 931. For all wavelength bands from 400 to 700 nm, reflectance never exceeded 25%. Because the reflectance record is dominated by high-frequency variability resulting from black color banding and mottling, it is impossible to match changes in reflectance to the boundaries of lithologic units (Fig. 4). The average ratio between the reflectance in end-member wavelength bands (650–700 nm = red spectrum, and 450–500 nm = blue spectrum) is near 1.2 (Fig. 4), indicating that reflectance of longer wavelengths (red spectrum) is slightly enhanced compared to that of short wavelengths (Schneider et al., this volume).

BIOSTRATIGRAPHY

Calcareous Nannofossils

Calcareous nannofossils recovered at Site 931 represent a stratigraphic interval from the Holocene (Zone CN15b) through the middle Pleistocene (Zone CN14b). The abundance and preservation of nannofossils vary from good to poor through the sequence recovered (Table 3). Nannofossils are abundant and well preserved in the Ho-

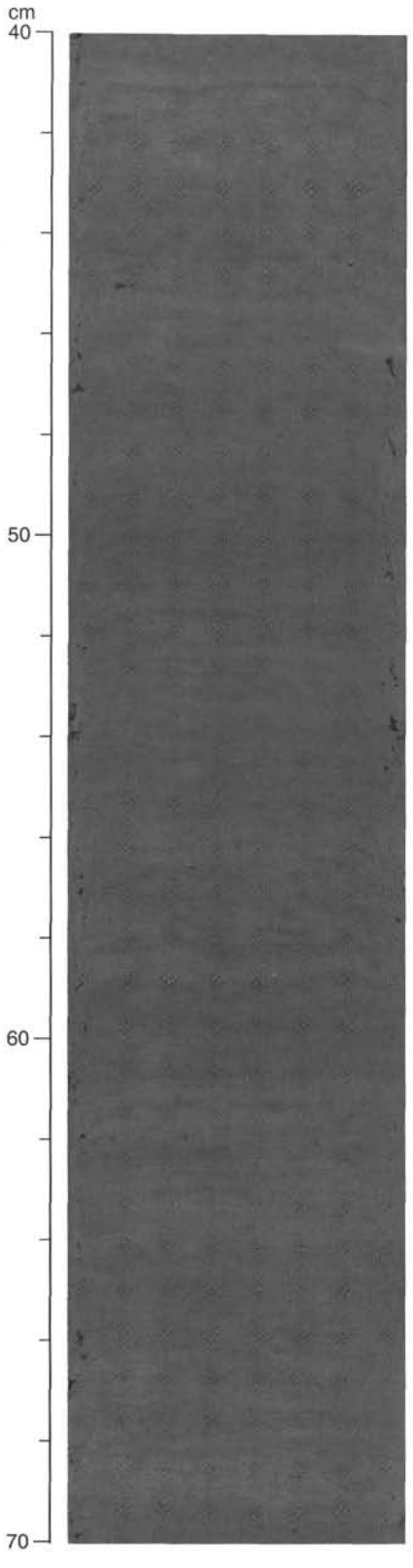

Figure 6. Alternate light-colored (2–6 mm thick) and dark-colored (1–3 mm thick) laminae from Subunit IIC (interval 155-931B-11X-2, 40–70 cm).

locene section (Unit I). The mud-line sample (931A-1H-Ml, 931C-1H-Ml) has a highly diversified and well-preserved *Emiliania huxleyi* acme assemblage (Zone CN15b) down to 0.56 mbsf (Sample 931A-1H-1, 56 cm) just above the iron-rich crust. Below this crust, the nannofossil abundance and preservation rapidly deteriorates in the olive gray clay of Unit II. No calcareous nannofossils are present at 1.25 mbsf (Sample 931A-1H-1, 125 cm). Nannofossils reappear in low abundances and with poor preservation at 7.9 mbsf (Sample 931A-2H-2, 100 cm), and this sporadic occurrence continues downhole in the glacial-age sediment of Unit II.

The nannofossils in the Unit II pre-Holocene interval of color-mottled silty clay is also generally characterized by poor preservation. Nannofossils are rare within the mass transported Unit III from 225 to 320 mbsf (Samples 931B-25X-CC, 29–30 cm, to -35X-CC, 37–38 cm). Nannofossils reappear in relatively high abundance in clasts in the bottom of the mass-transported unit at 334 mbsf (Sample 931B-36X-CC, 40–41 cm), where a nannofossil assemblage of Zone CN15a appears. The nannofossils of the bioturbated dark clay of Units IV (349.25 to 349.46 mbsf) and V (349.46 to 421.3 mbsf) are lacking *E. huxleyi*. This interval falls into Zone CN14b, as a few atypical specimens of *P. lacunosa* are considered reworked at 354.5 mbsf (Sample 931-39X-1, 43 cm). No calcareous nannofossils were found from 360 to 421 mbsf in the mottled silty clay with silt laminae of Subunit VB.

Planktonic Foraminifers

In general, high abundances and a diverse assemblage of planktonic foraminifers characterize the Holocene and middle Pleistocene sections, whereas low abundances and a lack of diversity are characteristic of the late Pleistocene sections (Table 4). The boundary between Ericson Zones Z and Y (disappearance of *G. menardii* and *G. tumida*) is between 6 and 10 mbsf (Fig. 14). However, given the possible downhole contamination of core-catcher samples (see "Biostratigraphy" section, "Site 934" chapter, this volume), the boundary is likely near the bottom of Unit I at a much shallower level.

Foraminifers are rare or absent in the lower part of Unit II from 92.06 to 248.3 mbsf (Sample 931B-11X-CC, 26 cm, through -27X-CC, 35 cm). Because Ericson zones are iteratively based on successive abundance shifts, this foraminifer-barren zone prevents the determination of Ericson zones below 85 m in Hole 931B. Foraminifers are present from 248.24 to 372.45 from the bottom of Unit III to Unit V (Sample 931B-27X-CC, 26 cm, through -40X-CC, 43 cm). The presence of *G. calida calida* and *G. crassaformis hessi* in Unit IV and VA is indicative of a middle to late Pleistocene age. The presence of relatively abundant *G. ruber* (pink) indicates an age younger than 0.43 Ma. The presence of *G. tumida flexuosa* further constrains the age of Units IV and V to between 0.43 and 0.1 Ma (isotope Stages 5, 7, 9, or 11).

Authigenic Minerals

In Hole 931B, vivianite nodules are barren in the upper section of the hole and are present from 10.84 mbsf down to 320.57 mbsf (Fig. 15). Planktonic foraminifers were abundant in the upper sections of the hole from the surface down to 92.06 mbsf and from 264.5 mbsf to 372.45 mbsf. Vivianite nodules are abundant below 361.65 mbsf to the bottom of the hole. Changes in the abundance of planktonic foraminifers and vivianite nodules correspond to lithologic changes. Foraminifer abundances decreases downhole, whereas vivianite nodule abundance increases, in the clays and silt-laminated clays. Foraminiferal abundances increase and the authigenic vivianite abundances decrease in the debris-flow unit. Then the abundances reverse in the silty clay unit at the bottom of the hole (Fig. 15).

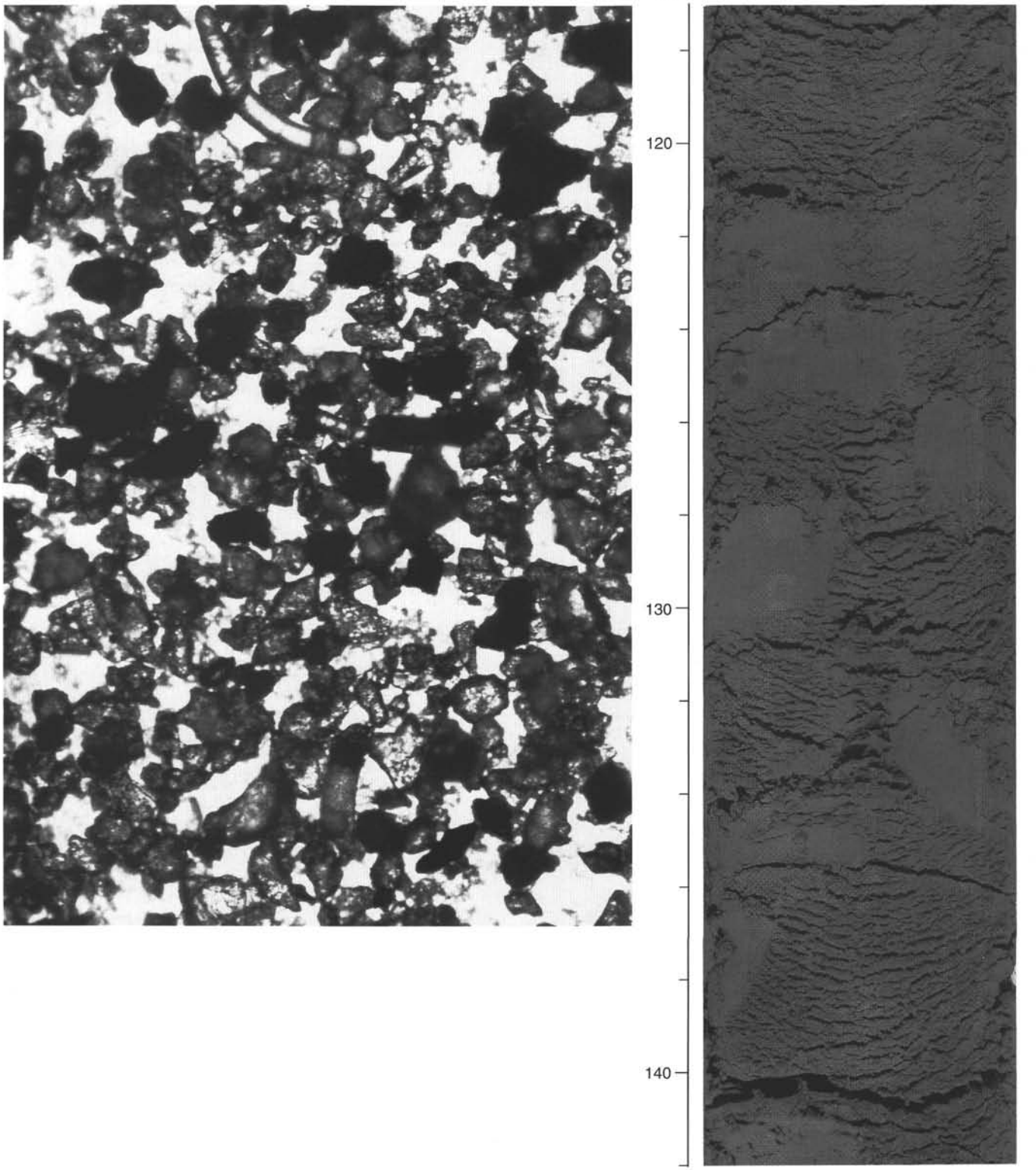

Figure 7. Characteristics of silt deposits in Subunit IIC. **A.** Photomicrograph in plane-polarized light of dry, well-sorted silt grains on the surface of an uncovered glass slide. Scale: 87 mm on photo = 500 µm. **B.** Mud clasts within thick, gas-expanded silt bed in Subunit IIC (interval 155-931B-16X-3, 117–142 cm).

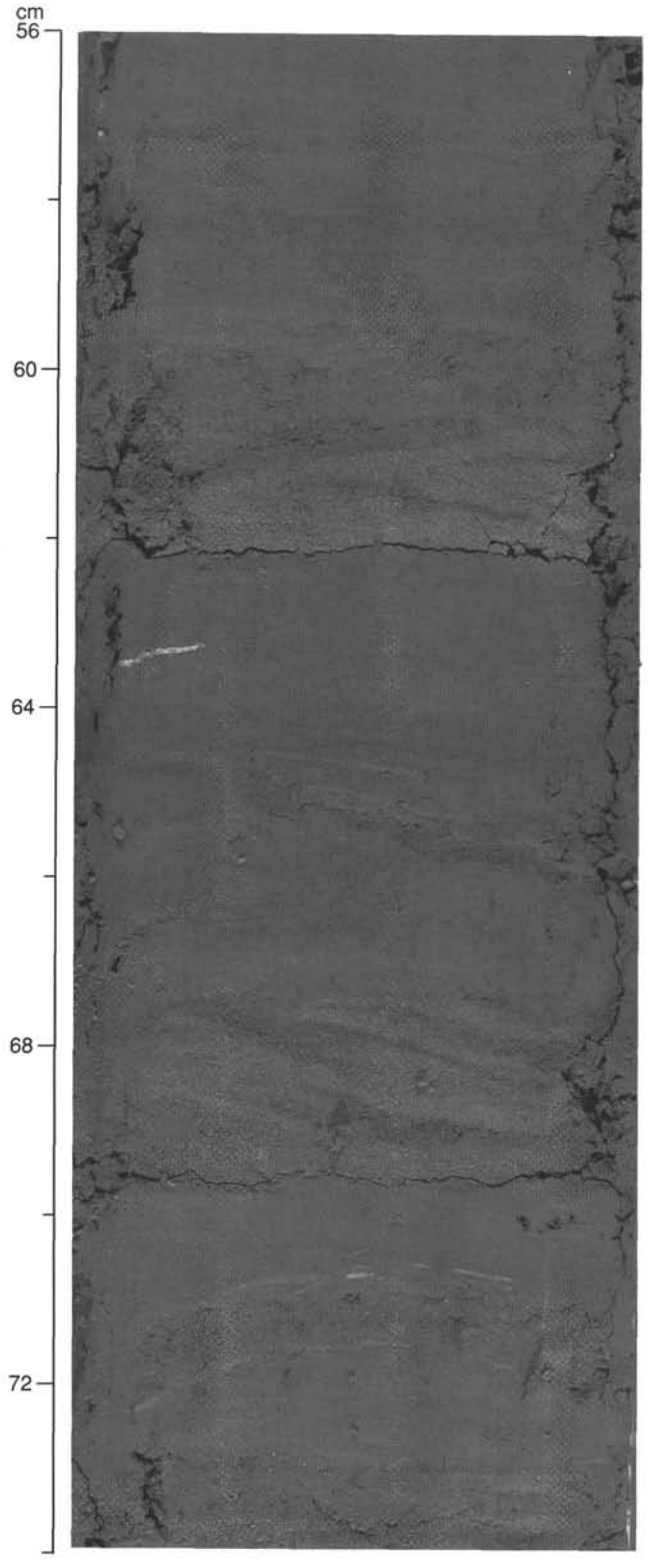

Figure 8. Thin to medium silt and very fine sand beds in Unit III. The beds at 62 and 70 cm show cross-lamination highlighted by the presence of dark-colored hydrotroilite (interval 155-931B-25X-2, 56–74 cm).

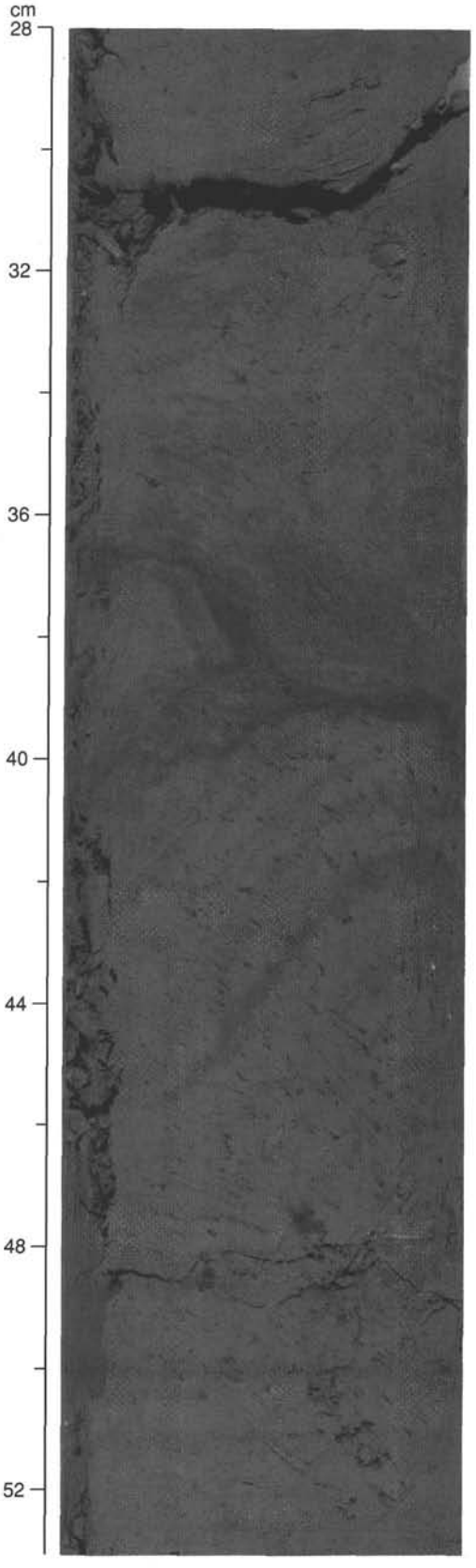

Figure 9. Contorted bedding (e.g., 35–46 cm) within the clays of Unit III (interval 931B-38X-1, 28–53 cm).

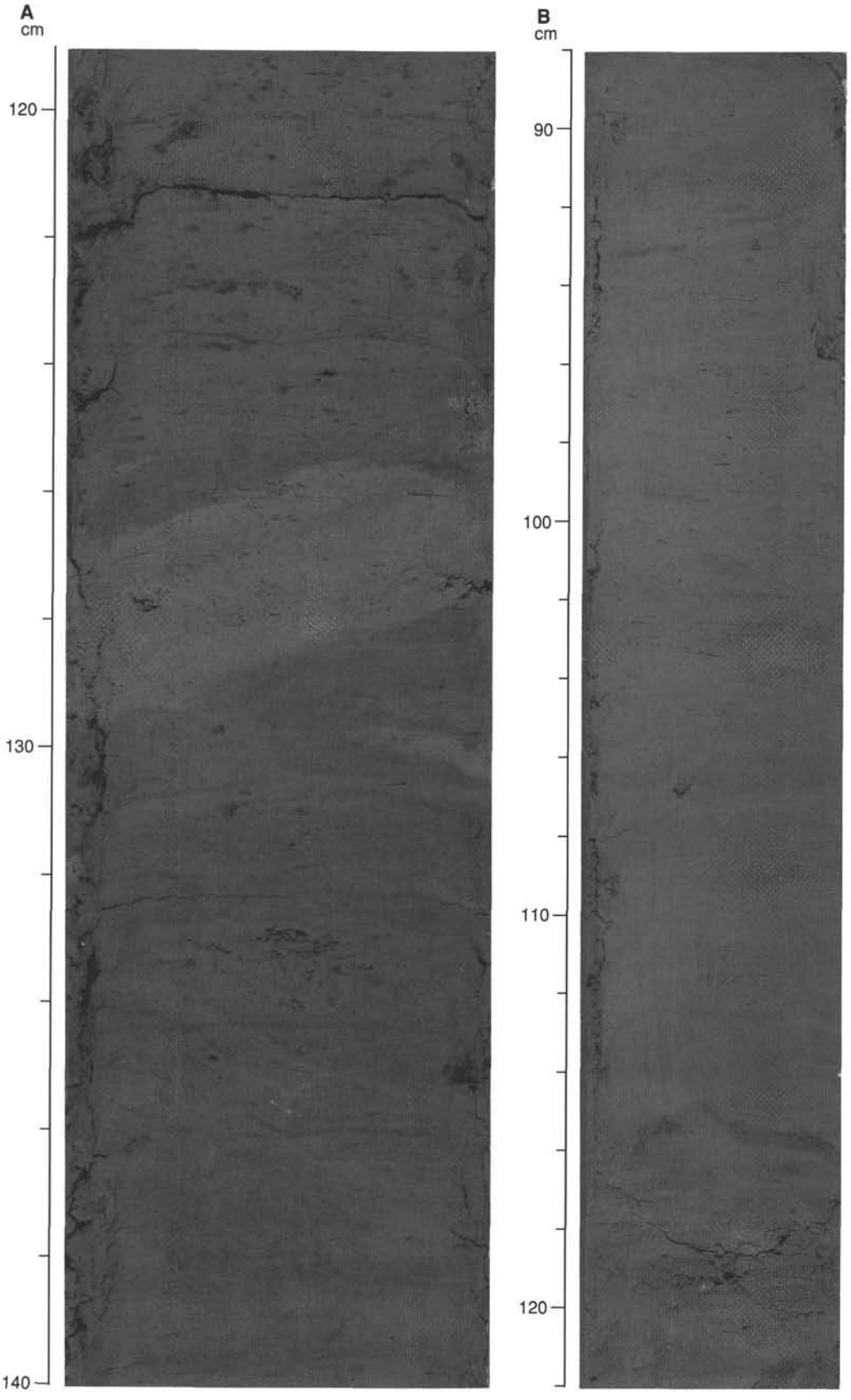

Figure 10. Carbonate-rich clasts in Unit III. **A.** A small clast between scale divisions 126 and 129.5 cm (interval 155-931B-36X-6, 119–140 cm). The thin horizontal bands at about 1.5-cm spacing from about 130 to 140 cm mark the boundaries of drilling biscuits. The 1- to 3-mm black blebs are hydrotroilite. **B.** A large clast between scale divisions 91 and 115 cm (interval 155-931B-36X-5, 88–122 cm).

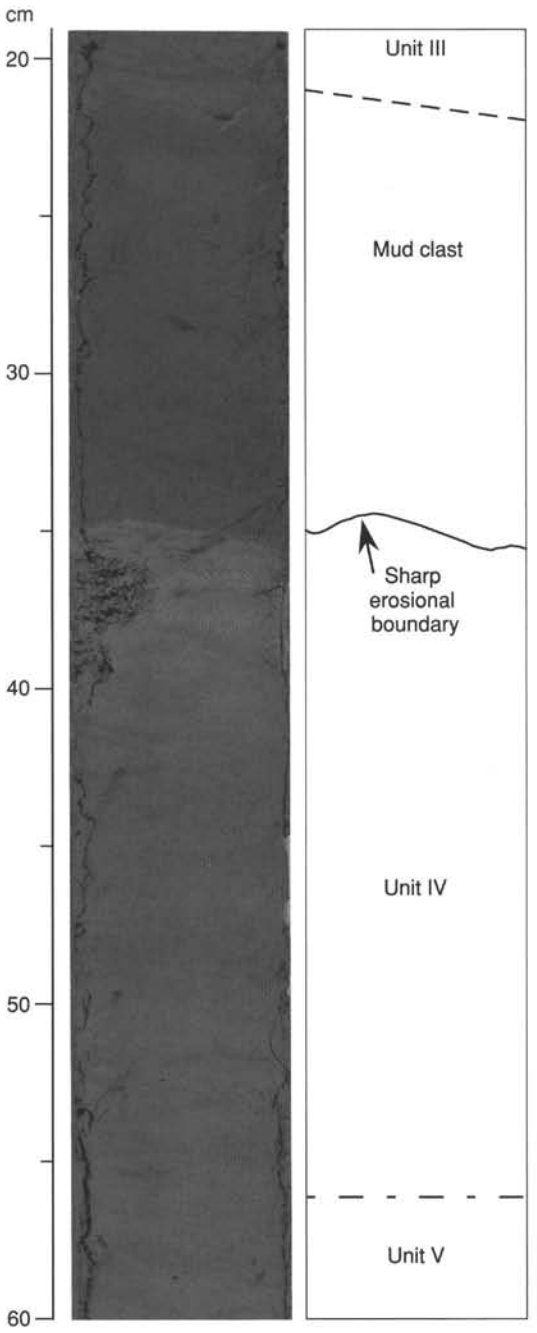

Figure 11. Sharp boundary (at 35 cm) between the base of Unit III and the top of Unit IV. A mud clast (21–35 cm) marks the base of a mass transport (debris flow?) deposit. The top of Unit IV (e.g., 35–56 cm) is identified by its lighter colored carbonate-rich clays (interval 155-931B-38X-4, 19–60 cm).

Benthic Foraminifers

Benthic foraminifers were found sporadically in Holes 931A and 931B (Table 4). The benthic foraminifers found at Site 931 comprise bathyal species *Bulimina marginata, Bolivina striatula,* and *Quinqueloculina* sp. and abyssal species *Uvigerina* spp. and *Pyrgo* spp. *Uvigerina* spp. and *Pyrgo* spp. are found in the finer grained clay units. The bathyal species tend to occur in coarser sediment such as in lithologic Unit III from 225 mbsf (Sample 931B-25X-CC, 20 cm) to 361 mbsf (Sample 931B-28X-CC, 42 cm) and are not as well preserved.

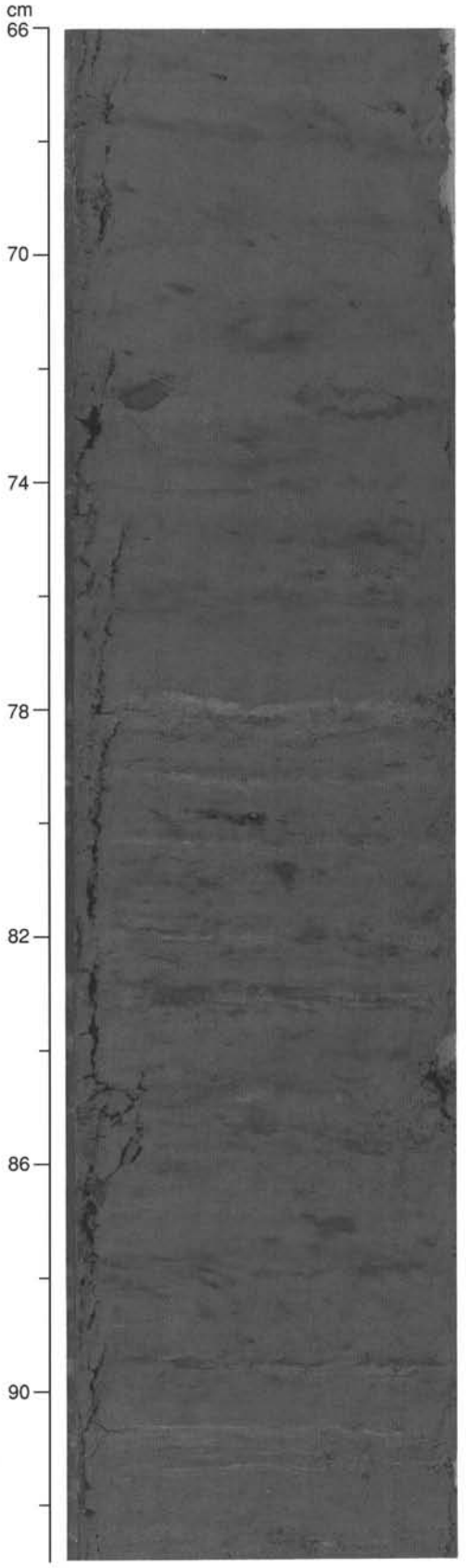

Figure 12. Silt laminae within faintly color-banded, mottled silty clay of Unit V (interval 155-931B-39X-5, 66–93 cm).

Table 2. Relative peak intensities of main minerals in representative lithologies at Site 931.

Core, section, interval (cm)	Relative intensity of primary peaks								
	Smectite	Mica + Illite	Kaolinite	Quartz	Plagioclase	K-feldspar	Augite	Hornblende	Calcite
155-931A-									
1H-4, 50–55	12.0	26.6	14.0	100.0	10.9	*	3.7	*	5.1
155-931B-									
2H-4, 50–51	13.2	25.5	13.5	100.0	11.7	6.0	3.6	*	*
3H-4, 35–36	16.2	30.3	16.2	100.0	9.8	5.1	3.0	*	*
4H-4, 49–50	18.6	35.8	16.4	100.0	8.9	5.5	2.6	*	*
5H-3, 50–51	10.6	20.6	15.8	100.0	10.6	*	3.0	*	*
6H-5, 50–51	12.6	24.0	13.3	100.0	10.1	5.1	3.3	*	*
7H-4, 69–70	13.1	28.6	16.0	100.0	11.0	*	3.2	*	*
8H-4, 87–88	12.1	18.3	12.4	100.0	9.6	*	2.5	2.1	2.1
9H-4, 40–41	13.4	26.5	14.8	100.0	8.1	4.8	3.1	*	*
10H-4, 44–45	13.4	27.8	11.3	100.0	9.7	5.7	3.8	*	*
11X-4, 50–51	9.8	26.6	14.7	100.0	8.6	*	2.7	2.5	2.5
12X-4, 42–43	12.8	16.0	10.9	100.0	7.2	6.8	2.6	*	*
13X-4, 50–51	9.4	23.1	12.7	100.0	8.3	4.8	1.8	0.9	0.9
14X-4, 50–51	17.2	21.1	9.8	100.0	8.7	3.8	1.4	2.6	2.6
15X-2, 54–55	10.7	24.3	10.9	100.0	14.5	4.4	2.6	*	*
16X-3, 94–95	11.8	15.3	9.0	100.0	8.6	3.8	1.7	*	*
19X-4, 49–50	11.2	22.6	13.4	100.0	12.1	5.7	3.0	*	*
21X-2, 143–145	13.1	25.3	12.7	100.0	11.2	*	2.5	*	*
23X-2, 76–77	6.9	20.1	11.1	100.0	9.6	3.5	1.0	1.3	1.3
25X-4, 72–73	12.0	23.7	14.3	100.0	10.7	6.2	2.6	*	*
26X-1, 28–29	6.9	21.4	12.2	100.0	8.4	*	3.3	*	*
27X-4, 53–55	8.1	21.2	9.2	100.0	9.8	4.7	2.4	*	*
28X-3, 73–74	4.5	17.2	7.8	100.0	7.5	*	2.0	*	1.7
29X-3, 64–65	9.8	18.7	8.8	100.0	8.0	4.0	2.0	*	*
31X-4, 77–78	10.4	21.5	12.3	100.0	7.6	*	2.9	*	*
32X-4, 34–35	14.9	30.5	14.9	100.0	11.1	*	2.9	*	*
33X-4, 60–61	7.4	17.8	10.5	100.0	7.1	5.9	2.0	2.0	*
34X-4, 58–59	7.7	16.3	8.1	100.0	11.3	4.9	2.0	*	1.6
35X-4, 10.1–11	9.9	20.2	11.5	100.0	6.4	10.9	2.5	*	*
36X-4, 50–51	11.5	20.2	10.0	100.0	7.5	*	2.4	*	2.9
37X-4, 40–41	*	18.5	15.0	100.0	8.1	*	*	0.3	41.9
38X-3, 84–85	10.2	25.8	12.5	100.0	8.1	5.6	2.6	*	*
39X-4, 16–17	16.0	31.0	16.8	100.0	11.8	*	4.1	*	*
40X-3, 56–58	13.1	31.1	18.3	100.0	11.1	*	3.1	*	*
41X-4, 78–79	19.4	28.6	17.1	100.0	9.3	4.9	3.5	*	2.3
42X-4, 49–50	16.5	23.8	15.7	100.0	9.4	6.2	3.9	*	*
43X-5, 67–68	12.0	25.9	18.7	100.0	12.3	5.6	3.8	*	*
44X-4, 50–51	17.7	38.7	21.8	100.0	9.9	6.7	3.9	*	*
45X-4, 51–52	19.3	39.7	17.2	100.0	9.9	*	3.9	*	*

Notes: See "Lithostratigraphy" section in the "Explanatory Notes" chapter, this volume, for XRD methods. * denotes non-detection.

Siliceous Microfossils

Site 931 is mostly barren of diatoms except for the upper 0.8 mbsf in Holes 931A and 931B (Table 3). Pelagic diatoms of marine origin are rare but well preserved in the mud-line samples of Holes 931A and 931C. These assemblages include warm-water species such as *Coscinodiscus africanus, Actinocyctus curvatulus,* and *C. eccentricus* of late Pleistocene age. More dissolution-prone species (e.g., *Rhizosolenia* sp.) were not present in the mud-line diatom assemblage. The abundance and preservation of marine pelagic diatoms decreases rapidly downhole from the sediment-water interface to a depth of 0.30 mbsf (Sample 931B-1H-1, 29 cm). Except for a few valve fragments of the neritic diatom *Navicula* sp. at 92.06 mbsf (Sample 931B-11X-CC, 35 cm), no other pre-Holocene marine or freshwater diatoms were observed at Site 931. This is most likely a result of dilution by high sedimentation rates combined with dissolution. Siliceous sponge spicules are the only significant amount of pre-Holocene biogenic silica found at Site 931. The spicules occur in a variety of forms and are scattered throughout the cored section (Table 5). Radiolarians are present as fragments in the mud-line samples of Holes 931A and 931C and have been found in a few pre-Holocene core-catcher samples.

Palynology

Palynomorph abundance and preservation varies downhole (Table 5). In general, high abundance and good preservation are characteristic only in the late Pleistocene section, whereas low abundance and poor preservation are characteristic of the Holocene and middle Pleistocene sections.

Pollen and spore assemblages found in the Holocene sections from 0 to 0.83 mbsf include stephanoporate (SP), monosulcus (possible Palmae), and monolete fern spores. The assemblage observed from the late Pleistocene section between 5.6 and 14.0 mbsf include *Alnus,* Proteaceae, *Cecropia,* Ericaceae, Rhizophoraceae, Gramineae, Cyperaceae, tricolporate (TCP), triporate (TP), tricolpate (C), and stephanoporate (SP) types. Fern spores include Cyatheaceae and monolete spores. In general, pollen and spore types may be derived from a range of vegetation communities including Andean rain forest, lowland rain forest, cerrado (grassland/woodland), and riverbank/floodplain forest (várzea). However, *Cecropia* and Gramineae plants are common taxa in dry cerrado communities. The appearance of Rhizophoraceae in Sample 931B-3H-2, 119–121 cm (12.99 mbsf), suggests that coastal mangrove communities were well established on the exposed continental shelf during lower sea levels. The relative proximity of these communities to the fan during glacial periods may have increased mangrove pollen representation in the assemblage. The samples taken from deeper sections within Hole 931B have poor preservation and generally low abundance. The assemblages tend to be dominated by spores and are not diagnostic of a specific terrestrial environment. The high abundance of spores relative to pollen may be a result of rapid sediment accumulation and sorting, or it may be a function of selective preservation of spores under harsh sedimentation conditions (e.g., chemical dissolution or mechanical erosion).

Wood particles have been observed in all sample slides in varying abundance. Macroscopic wood remains, including leaf fragments and intact seeds, have been observed with a high abundance from Pleistocene core-catcher samples between 167 and 233 mbsf (Table 5). Dinoflagellates are present in the mud-line sample of Hole 931A and in a few pre-Holocene samples.

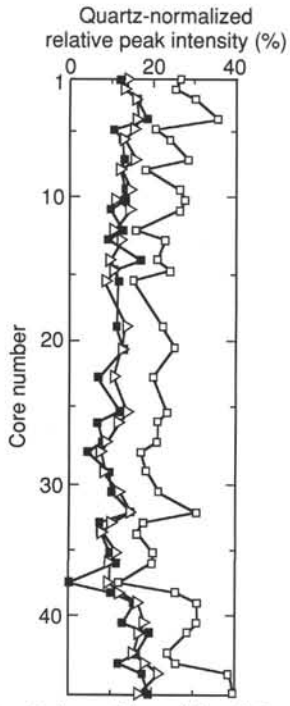

Figure 13. Plots of the relative peak intensities of clay minerals (normalized to a primary peak intensity of 100% for quartz) by core number. All samples come from Hole 931B, except for the shallowest sample, which comes from Hole 931A. Solid squares = smectite; open squares = illite (+ mica); open triangles = kaolinite.

Stratigraphic Summary

High abundances are characteristic of all the calcareous and siliceous microfossil groups (nannofossils, foraminifers, diatoms) in the brown nannofossil and foraminifer clay of Unit I. This section is defined as Zone Z or Holocene. Palynomorphs are rare in this zone. The disappearance of *G. menardii* and *G. tumida* from the foraminifer assemblage at Site 931 places the Ericson Z/Y boundary at between 6 and 10 mbsf in core-catcher samples. This boundary, however, is likely to occur at the bottom of Unit I due to the possible downhole contamination of core catchers. In the dark olive green to dark gray silty clay of Unit II there are extremely low abundances of the siliceous and calcareous microfossil groups. This section is classified as the Y Zone (late Pleistocene). Palynomorphs show high abundance in this zone. The sediment is barren of any age-diagnostic microfossils from 92 to 222 mbsf in Hole 931B. Foraminifers and calcareous nannofossils reappear at 332 mbsf, 17 m above the base of the debris flow of Unit III. The presence of relatively abundant *G. ruber* (pink) indicates an age younger than 0.43 Ma. The presence of *G. tumida flexuosa* further constrains the age of Units IV and V to between 0.43 and 0.1 Ma (isotope Stages 5, 7, 9, or 11). The absence of *P. lacunosa* and *E. huxleyi* in assemblages dominated by *Gephyrocapsa* indicates that the age of Units IV and V is 0.26–0.46 Ma (Zone CN14b).

PALEOMAGNETISM

Remanence Studies

The remanent magnetizations of the archive-halves of all APC cores were measured with the pass-through magnetometer using a demagnetization field of 20–25 mT, with the exception of Core 931B-1H. In general, we measured only selected XCB core sections to confirm the presence of drilling biscuits in the cores. In addition, selected discrete samples from the APC and XCB cores underwent stepwise demagnetization, and their remanent magnetizations were measured with the pass-through magnetometer. The Tensor tool was used on Cores 931B-3H through -9H. The corrected declinations were centered on 0° with standard deviations less than 1°. The improvement in the performance of this instrument can be attributed to the use of the standard battery pack instead of the rechargeable one that was used at Site 930.

The results of stepwise demagnetization show that for most samples within the APC cores, the vertical drill stem overprint is removed by the application of a 10-mT field. This is reflected in the inclinations for the APC cores, which are generally low and centered around 0° (Fig. 16). An apparent excursion, tentatively correlated with the Lake Mungo, was identified in the bottom of Section 931B-9H-7 at 76.5 mbsf. No other geomagnetic excursions or events are apparent in Cores 931A-1H through -6H and Cores 931B-1H through -9H.

Periodic oscillations in declination, which we interpret as secular variation, are discernible from 1 to 15 and 30 to 41 mbsf in Hole 931A. Within biscuited sections of XCB cores (Sections 155-931B-27X-2 and -36X-4), variations in declination and inclination indicated rotation about the vertical and, at times, horizontal axes during drilling.

Magnetic Susceptibility

Whole-core and discrete-sample magnetic susceptibilities were measured in the same manner as at Site 930. In addition, magnetic susceptibility data were acquired during downhole logging.

The susceptibility record of Hole 931B is shown in Figure 17. The record from about 140 to 220 mbsf is incomplete due to low recovery. The whole-core and discrete-sample data show similar trends downhole. The weakest values are associated with the finer grained units (clayey), whereas the strongest values are associated with the coarser (silty) units. However, overall, the long-period changes in susceptibility do not correlate with the small-scale grain-size characteristics as recorded in lithostratigraphy observation.

The downhole comparison of these data with the GHMT logging tool suggests that, despite long intervals of poor recovery, the general pattern of susceptibility change with depth is resolved in the whole-core data. More detailed post-cruise comparisons of the two data sets will allow us to fill in the gaps for the middle portions of the hole.

ORGANIC GEOCHEMISTRY

Volatile Hydrocarbons

Gas analyses were conducted on samples from Hole 931A to 51 mbsf and Hole 931B to 418 mbsf. Headspace methane concentrations at Site 931 increase rapidly below the sediment surface to a maximum value of about 21,400 ppm at 8.30 mbsf. Methane concentrations then range between 13,600 ppm at 65.30 mbsf and 600 ppm at 43.56 mbsf with higher values in coarser sediment. (Fig. 18; Table 6). As at the previous site, the sharp increase of methane levels near the sediment surface likely reflects the onset of methanogenesis.

The vacutainer samples taken from gas expansion voids display much higher concentrations, in some cases by more than two orders of magnitude, than those measured by headspace sampling (Fig. 18). High methane concentrations were measured between 36.10 mbsf and 65.30 mbsf with a maximum value of 707,000 ppm at 46.30 mbsf. High values also occur near the bottom of Hole 931B in Cores 155-931B-43X and -44X (695,000 ppm and 763,000 ppm, respectively). Significant concentrations of hydrocarbons of higher molecular weight were not recorded. The gas compositions observed at Site 931 suggest a biogenic methane source.

Table 3. Calcareous nannofossil and siliceous microfossil abundance data for Holes 931A, 931B, and 931C.

Core, section, interval (cm)	Top interval (mbsf)	Bottom interval (mbsf)	Calcareous nannofossils			Diatoms		Sponge spicules	Radiolarians	Phytoliths	Ericson Zone (inferred from foraminifers)	Age (inferred from foraminifers)
			Abundance	Preservation	Zone	Marine	Fresh water					
155-931A-												
1H-Ml, 0–0	0	0	a	g	CN15b	r	b	c	f	b	Z	Holocene
1H-1, 0–1	0	0.01	a	g		r	b	c	f	b	Z	Holocene
1H-1, 5–6	0.05	0.06				r	b	c	r	b	Z	Holocene
1H-1, 9–10	0.09	0.1				vr	b	c	b	b	Z	Holocene
1H-1, 13–14	0.13	0.14				vr	b	c	b	b	Z	Holocene
1H-1, 19–20	0.19	0.2				b	b	c	b	b	Z	Holocene
1H-1, 26–27	0.26	0.27				tr	b	c	b	b	Z	Holocene
1H-1, 29–30	0.29	0.3				b	b	c	b	b	Z	Holocene
1H-1, 34–35	0.34	0.35									Z	Holocene
1H-1, 41–42	0.41	0.42									Z	Holocene
1H-1, 45–46	0.45	0.46				b	b	r	b	b	Z	Holocene
1H-1, 49–50	0.49	0.5									Z	Holocene
1H-1, 51–52	0.51	0.52									Z	Holocene
1H-1, 54–55	0.54	0.55				b	b	r	b	b	Z	Holocene
1H-1, 58–59	0.58	0.59									Z	Holocene
1H-1, 66–67	0.66	0.67									Z	Holocene
1H-1, 69–70	0.69	0.7				b	b	b	b	b	Z	late Pleist.?
1H-1, 73–74	0.73	0.74									Z	
1H-1, 84–85	0.84	0.85									Z	late Pleist.?
1H-CC, 14–15	6.14	6.15	r	p		b	b	b	b	b	Z	late Pleist.?
2H-CC, 27–28	16.29	16.30	vr	p		b	b	b	b	b	Y	late Pleist.
3H-CC, 30–31	25.83	25.84	tr	—		b	b	b	b	b	Y	late Pleist.
4H-CC, 35–36	35.39	35.40	r	p		b	b	b	b	b	Y	late Pleist.
5H-CC, 58–59	44.96	44.97	tr	—		b	b	b	b	b	?	late Pleist.
6H-CC, 23–24	54.07	54.08	b	—		b	b	b	b	b	Y	late Pleist.
155-931B-												
1H-CC, 83–84	0.83	0.84	a	g	CN15b	r	b	c	r	b	Z	Holocene?
2H-CC, 26–27	10.84	10.85	vr	p		b	b	c	b	b	Y	late Pleist.
3H-CC, 35–36	21.15	21.16	vr	p		b	b	r	b	b	Y	late Pleist.
4H-CC, 39–40	30.18	30.19	vr	p		b	b	r	b	b	Y	late Pleist.
5H-CC, 44–45	39.54	39.55	b	—		b	b	r	b	b	Y	late Pleist.
6H-7, 29	48.09		vr	p		b	b	r	b	b	Y	late Pleist.
6H-7, 30	48.10		tr	—		b	b	b	b	b	Y	late Pleist.
6H-7, 31	48.11		tr	—		b	b	r	b	b	Y	late Pleist.
6H-CC, 44–45	49.19	49.20	b	—		b	b	tr	b	b	Y	late Pleist.
7H-CC, 74–75	57.75	57.76	b	—		tr	b	f	b	b	Y	late Pleist.
8H-CC, 36–37	68.10	68.11	tr	—		b	b	b	b	b	Y	late Pleist.
9H-CC, 96–97	78.23	78.24	tr	—		b	b	b	b	b	Y	late Pleist.
10X-CC, 69–70	84.66	84.67	vr	p		b	b	b	b	b	—	—
11X-CC, 35–36	92.15	92.16	r	p	CN15	tr	b	r	b	b	?	?
12X-CC, 32–33	100.65	100.66	tr	—		b	b	r	b	b	?	Pleist.
13X-CC, 34–35	108.99	109.00	tr	—		tr	tr	r	b	b	—	—
14X-CC, 22–23	119.78	119.79	tr	—		b	b	r	b	b	—	—
15X-CC, 20–21	127.50	127.51	tr	—		b	b	f	b	b	—	—
16X-CC, 18–19	137.73	137.74	tr	—		b	b	f	b	b	—	—
19X-CC, 15–16	167.35	167.36	tr	—		b	b	f	b	b	—	—
23X-CC, 12–13	202.46	202.47	vr	—		b	b	f	b	b	—	—
24X-CC, –	219.10		b			b	b	b	b	b		Pleist.
25X-CC, 29–30	225.06	225.07	vr	—		b	b	r	b	b		
26X-CC, 27–28	233.18	233.19	b			b	b	b	b	b		
27X-CC, 35–36	248.33	248.34	b			b	b	b	b	b		
28X-CC, 36–37	255.05	255.06	b			b	b	b	b	b		Pleist.
29X-CC, 17–18	264.48	264.49	b			b	b	vr	b	b		Pleist.
30X-CC, 30–31	276.90		tr	—		b	b	r	b	b		Pleist.
31X-CC, 23–24	287.39	287.40	b			b	b	vr	b	b		Pleist.
32X-CC, 66–67	295.73	295.74	vr	—		b	b	b	b	b		Pleist.
33X-CC, 46–47	302.66	302.67	b			b	b	b	b	b		Pleist.
34X-CC, 12–13	311.13	311.14	b			tr	b	r	b	b		Pleist.
35X-2, 28	317.28		c	m								Pleist.
35X-2, 31	317.31		tr	—								Pleist.
35X-3, 61	319.11		vr	—								Pleist.
35X-3, 73	319.24		b									Pleist.
35X-CC, 37–38	320.57	320.58	vr	p								Pleist.
36X-5, 105–111	332.15	332.21	a	g	CN15a	b	b	vr	b	b		Pleist.
36X-CC, 40–41	334.50	334.51	a	g		b	b	b	b	b		Pleist.
37X-2, 124–125	337.54	337.55	vr	p		b	b	b	b	b		Pleist.
37X-4, 34–35	339.63	339.64	a	g		b	b	b	b	b		Pleist.
37X-CC, 33–34	340.62	340.61	c	m		b	b	b	b	b		Pleist.
38X-4, 33–34	349.23	349.24	c	m		b	b	b	b	b		Pleist.
38X-4, 39–40	349.29	349.30	a	g	CN14b	b	b	b	b	b		mid Pleist.
38X-4, 48–49	349.38	349.39	a	g		b	b		b	b		mid Pleist.
38X-5, 11–12	350.05	350.06	a	g		b	b		b	b		mid Pleist.
38X-5, 13–14	350.07	350.08	a	g		b	b		b	b		mid Pleist.
38X-CC, 51–52	355.80	353.81	a	g		b	b	b	b	b		mid Pleist.
39X-1, 43	354.93		a	g		b	b		b	b		mid Pleist.
39X-4, 50	359.10		tr	—		bb	b		b	b		mid Pleist.
39X-CC, 35–36	361.74	361.75	r	m		b	b	b	b	b		mid Pleist.
40X-6, 10	370.56		tr	—		b	b		b	b		
40X-CC, 43–44	372.45	372.46	b			b	b		b	b		—
41X-CC, 21–22	381.23	381.24	vr	—		b	b		b	b		—
42X-CC, 23–24	392.07	392.08	b			b	b	vr	b	b		—
43X-CC, 33–34	402.63	402.64	b			b	b	b	b	b		—
44X-CC, 54–55	411.85	411.86	b			b	b	b	b	b		—
45X-CC, 39–40	418.19	418.20	b			b	b	b	b	b		—
155-931C-												
1H-Ml, 0	0.00										Z	Holocene

Table 3 (continued).

Core, section, interval (cm)	Top interval (mbsf)	Bottom interval (mbsf)	Calcareous nannofossils			Diatoms		Sponge spicules	Radiolarians	Phytoliths	Ericson Zone (inferred from foraminifers)	Age (inferred from foraminifers)
			Abundance	Preservation	Zone	Marine	Fresh water					
1H-1, 18–20	0.18	0.20	a	g	CN15b	r	b	c	r	b	Z	Holocene
1H-CC, 11–12	4.09	4.10	r	m		b	b	b	b	b	Z	Holocene?
2H-CC, 31–32	13.92	13.93	tr			b	b	b	b	b	Y	late Pleist.
3H-CC, 27–28	23.90	23.91	b			b	b	b	b	b	Y	late Pleist.
4H-CC, 26–27	33.24	33.25	tr			b	b	b	b	b	Y	late Pleist.

Carbon, Nitrogen, and Sulfur Concentrations

The elemental data from Holes 931A and 931B are presented in Table 7, and the profiles for carbonate, TOC, TN, and TS are shown in Figure 19.

Carbonate (calculated as $CaCO_3$) concentrations are high in the top 0.89 mbsf, ranging from 49% to 11%. Except for elevated values at 340 mbsf, $CaCO_3$ contents remain fairly low throughout the rest of Site 931 (<4%). TOC concentrations are low (<0.5%) in the first 0.89 mbsf, below which they increase to about 1% and then steadily decrease to 0.4%. Several discrete intervals between 100 and 300 mbsf have markedly lower TOC values, ranging from 0.6% to 0.1% (Fig. 19).

Total nitrogen is moderately low in the top 5 m (≤0.07%), increasing to 0.16% at 90.80 mbsf and then steadily decreasing to 0.1% at 350 mbsf (Fig. 19). Between 90.80 and 350 mbsf, several intervals have much lower TN concentrations, with values below 0.05% at 80, 167, 232, and 264 mbsf. TN concentrations of about 0.1% are observed below 350 mbsf. Total sulfur concentrations are less than 0.5% throughout Site 931, except for values of over 6% at 5.6 and 8.6 mbsf. TS concentrations of more than 1% are also observed at 315.70 and 316.04 mbsf.

High carbonate concentrations at Site 931 correspond to carbonate-rich clay in Units I and IV. Relatively high carbonate contents were also measured at 0.64 mbsf (15%) and 0.89 mbsf (11%), below the observed foraminifer-rich clay. The debris flow in Unit III contains foraminifer-rich clay clasts with carbonate contents of 15%, 31%, and 13% at 315.70, 332.09, and 339.10 mbsf, respectively.

The TOC values generally show an inverse relationship with carbonate content. Low TOC concentrations (<0.5%) were observed in the carbonate-rich Units I and IV, and relatively high TOC values (>0.6%) were found in the other units. This distribution suggests lower terrigenous input during the deposition of Units I and IV. Low TOC concentrations were measured (ranging from 0.2% to 0.4%) in several samples from sand and silt layers in Units II and III. Total nitrogen shows a virtually identical downhole distribution to that of TOC, including low values (<0.05%) in sandy and silty sections (Fig. 19).

TS concentrations are generally low (<0.5%; Fig. 19). Two high values, at 5.65 (7%) and 8.65 mbsf (6.5%), correspond to mottled clay sections containing iron sulfide. A sample was analyzed by XRD to identify the sulfide minerals, but no identification could be made because the sulfide mineral was structurally amorphous. Two other high sulfur values, 1.5% and 1.1% TS, were obtained at 315.70 and 316.05 mbsf in Hole 931B. These elevated TS contents also likely reflect higher concentrations of sulfide minerals. As at Site 930, long-term diagenesis of organic matter is suggested by the gradual downhole decrease in TOC and TN from 20 to 400 mbsf (lithologic Units II, III, and V). In contrast to the debris flow at Site 930, however, elevated TN concentrations were not found in the Unit III debris flow from Hole 931B (see "Lithostratigraphy" section, this chapter).

[C/N]a values generally range from 8 to 13 over most of Hole 931A (Table 7). Between 315.70 mbsf and 361.10 mbsf, [C/N]a ratios are noticeably lower, ranging from 3 to 9. Below 361 m (Unit V), [C/N]a ratios remain fairly constant at 8 to 10. The abrupt change below 315 mbsf suggests a possible change in organic matter source that appears to correspond to the bottom part of the Unit III debris flow.

Rock-Eval Pyrolysis

We performed pyrolysis analysis on seven selected samples to measure the Hydrogen Index (HI), often used as an organic type indicator (Table 8). In immature sediment, where terrigenous organic material dominates, the HI values are usually less than 100 mg hydrocarbon (HC) per g TOC. In contrast, organic matter of predominantly marine origin shows HI values in the range of 200 to 400 mg HC/g TOC (Stein, 1991). All samples have HI values lower than 100 mg HC/g TOC except two samples (Samples 931A-1H-1, 64–65 cm, and 931B-6H-7, 65–66 cm; Table 8). These values suggest a predominantly terrigenous origin of organic matter even in samples with elevated $CaCO_3$ concentrations (155-931A-1H-1 and 155-931B-35X-1; Table 7). This method has limitations in the evaluation of organic matter type in sediment with low amounts of organic matter, however, and should be interpreted with caution.

INORGANIC GEOCHEMISTRY

Interstitial Water Analysis

Interstitial water analyses were performed on 16 sediment samples from Hole 931B, and on 18 samples from Hole 931C (Table 9). Samples from Hole 931B were taken between 8.20 and 408.80 mbsf, with a sample frequency of approximately one per 10 m for the upper 36 m and one per 30 m thereafter. To obtain a high-resolution record of pore-water chemistry near the sediment surface, Hole 931C was sampled from 0.20 to 31.69 mbsf with a frequency of approximately every 1.5 m for the first 20 m and every 3 m thereafter. The data are plotted together in Figure 20.

Salinities of the water samples range from 32.0 to 35.0 (Fig. 20A). In general, the shallower samples have slightly higher salinity; below 27.20 mbsf salinity is fairly uniform between 32 and 33.

Chloride concentrations in the upper 3.93 mbsf range from 550 to 553 mM. The values then increase steadily to around 560 mM by 10.05 mbsf and remain near 560 mM until 36.00 mbsf. Chloride concentrations in deeper samples are more variable, ranging from 537 to 558 mM, and are generally lower downhole (Fig. 20B). The lowest value, 537 mM at 201.22 mbsf, is within a debris-flow unit. A low chloride value from Hole 930B, 532 mM at 220.10 mbsf, was also within a debris flow. A possible explanation for these low chloride concentrations is melting of a previously precipitated clathrate. Pore-water pH values range from 8.01 to 7.46. The highest pH was measured at 5.55 mbsf (Fig. 20C) and is coincident with the peak in alkalinity. Below 5.55 mbsf, there is no distinct downhole trend; pore-water pH varies slightly between 7.5 and 7.9.

Pore-water alkalinity increases rapidly in the upper few meters of the core, reaching a maximum of 27.05 mM at 5.55 mbsf (Fig. 20D). Concentrations then decrease to 13.49 mM at 15.38 mbsf and remain around 10 to 12 mM through 291 mbsf. Below that depth, the alkalinity is more variable, with relatively high values of 18.66 mM at 318.40 mbsf and 25.21 mM at 408.80 mbsf.

Pore-water magnesium concentrations are near seawater values in the shallowest sample (54.5 mM at 0.20 mbsf; Fig. 20E) and decrease to under 50 mM by 2.95 mbsf. Below this depth, Mg concentrations vary between 32.1 to 48.4 with an overall gradual decrease downhole. Calcium is also at a maximum near the sediment surface, with concentrations of 12.2 mM at 0.20 mbsf (Fig. 20F). There is a pronounced decrease in calcium concentration over the upper 10 mbsf to 6.3 mM by 10.05 mbsf. Calcium concentrations remain between 4.1 and 6.8 mM below 10.05 mbsf.

Pore-water sulfate, phosphate, and iron concentrations are controlled by various reactions involving oxidation of organic matter in sediment (see "Inorganic Geochemistry" section, "Site 930" chapter, this volume) and by inorganic precipitation of diagenetic minerals. Sulfate reduction is evident in the shallowest sample, at 0.20 mbsf, and is complete by 8.55 mbsf (Fig. 21). Over the same interval, phosphate is initially constant around 10 µM, and increases to 273 µM over the interval from 2.95 to 5.55 mbsf (Fig. 21), while iron concentrations remain less than 30 µM (Fig. 21). Although iron oxide and iron oxyhydroxide reduction is likely in this interval, all reduced iron released to the pore fluids is precipitated as iron sulfide minerals. At the point where dissolved sulfate is completely reduced and iron is no longer being removed as sulfides, around 7 mbsf, the phosphate concentration decreases rapidly, suggesting that available reduced iron is being precipitated as iron phosphate (Fig. 21). This interpretation is substantiated by the presence of millimeter-sized nodules of vivianite (confirmed by X-ray diffraction analyses) found in varying abundances throughout the cores. The pore-water chemistry of samples from Hole 931C indicates that the vivianite nodules are precipitated primarily over the interval 5.55–10.05 mbsf. Dissolved iron concentrations rise slightly over this interval from less than 10 µM to 104.4 µM.

Below 10 mbsf, phosphate concentrations generally remain between 10 and 20 µM, with a slightly higher local maximum of 37.5 µM at 88.70 mbsf (Fig. 20I). Sulfate concentrations remain near zero below 7.05 mbsf (Fig. 20G). Iron concentration are quite variable below 7.05 mbsf. Over the interval 7.05–11.55 mbsf, iron concentrations increase from 8.5 µM to 104.4 µM. From 18.38 to 31.69 mbsf, the concentrations decrease again to 20–30 µM and then increase suddenly to 120.9 µM at 36 mbsf. Below 36 mbsf there is an overall decrease in iron concentration downhole to levels of a few tens of µM with the exception of the sample at 291.00 mbsf, which has a concentration of 127.3 µM (Fig. 20M).

Ammonium concentrations increase rapidly with depth from 0 mM at 0.20 mbsf to 7.73 mM at 36.00 mbsf (Fig. 20H). Values remain between 6.43 and 8.93 mM for most of the rest of the core with the exception of two samples at 318.40 and 347.25 mbsf that have concentrations of around 4 mM.

Dissolved silica concentrations range from 222 to 480 µM with no clear downhole trend (Fig. 20J). Values are erratic, with variations of nearly 200 µM for adjacent samples in the deeper parts of the hole. There is no apparent correlation of pore-water silica with lithology.

Pore-water potassium is most abundant at shallow depths, with concentrations of between 11.9 and 12.9 mM for samples above 3.93 mbsf (Fig. 20K). Concentrations then decrease to 10.1 mM at 13.05 mbsf. Below 13.05 mbsf, K remains relatively constant between 6.5 and 9.8 mM and shows a slight tendency toward lower concentrations downhole.

Concentrations of sodium range from 446 to 477 mM. There is no distinct trend in Na with depth (Fig. 20L) although the minimum value (at 201.22 mbsf) coincides with the minimum value for chlorinity.

Sediment Geochemistry

The major- and trace-element composition of 13 mud samples (Table 10 and Table 11) is similar. The variations in composition are in part due to subtle variations in lithology (i.e., quartz dilution effects). Silica abundances between 58 and 66 wt% are similar to post-Archean average shale (PAAS, 62.8 wt%; Taylor and McLennan, 1985). Alumina is between 18 and 23 wt% (PAAS = 18.9 wt%), consistent with a composition is dominated by clay minerals. Abundances of Fe_2O_3 (6.8% to 8.6%) are noticeably higher than PAAS (6.5%), whereas MgO (1.8 to 2.3 wt%) is much lower (PAAS = 6.5 wt%). CaO exhibits the greatest variability among analyzed elements (0.8 to 3.4 wt%) and is largely a function of the carbonate content of the muds. The amount of CaO contributed by carbonates is relatively small, however, and the overall geochemical composition indicates that these muds are dominantly terrigenous in provenance. In addition, the similarity among samples is an indication that the source was well-mixed prior to deposition on the fan.

The weathering of rock to produce sediment results in the decomposition of feldspar to produce more stable clay assemblages. The intensity of weathering experienced by a sediment can therefore be evaluated using the content of potassium and sodium relative to aluminum (Nesbitt and Young, 1984). The variation in K_2O/Al_2O_3 and Na_2O/Al_2O_3 with depth is shown in Figure 22. Normalizing abundances to alumina filters the effects of quartz dilution. PAAS and average upper crustal abundances (UC) are plotted for reference (Taylor and McLennan, 1985). For both K_2O/Al_2O_3 and Na_2O/Al_2O_3, lower ratios correspond to more extreme weathering conditions. The muds reported here have lower K_2O/Al_2O_3 than average shale, and Na_2O/Al_2O_3 similar to average shale. Both ratios probably record severe weathering conditions in the source.

The slight increase in K_2O/Al_2O_3 and Na_2O/Al_2O_3 for muds between 161.90 and 180.95 mbsf corresponds to the lower portions of lithologic Unit II, where recovery was poor. Although the variations are analytically significant, they are relatively minor, and sedimentary processes related to fan deposition can produce variations of this magnitude (e.g., sorting of feldspar into different size fractions). The peak height on X-ray diffraction patterns of plagioclase relative to quartz (Table 2, also increases slightly over this interval, however, and geochemical logs indicate increased K, U, and Th (see Figs. 28 and 29, "Downhole Logging" section, this chapter.

PHYSICAL PROPERTIES

Index Properties

Index properties were measured for all cores from Hole 931B and from Core 931A-1H in Hole 931A (Table 12). Only one sample, with a water content of 52%, was taken from the carbonate-rich clay of Unit I. In the clays and silty clays of Unit II (0.57–190.2 mbsf), water content decreases gradually with depth from 46% just below the seafloor to 28% at 181 mbsf. Water content varies widely in the upper 65 m of Unit III (199.8–349.25 mbsf) over a range of 16% to 28%. The uppermost part of this unit, recovered in Core 931B-23X, was not sampled for water content, porosity, and bulk density because the bulk properties of the sandy muds were significantly altered by expansion within the core. Samples from the upper 65 m of Unit III display a distinct ~5% decrease in water content between 225 and 230 mbsf. Below 277 mbsf, Unit III is characterized by more uniform and slightly higher water content. This change in the variability of water content coincides with marked increase in clay abundance in the sediment (Fig. 2). Lithologic Unit IV was not sampled for index properties. Water content is approximately 10% higher at the top of Unit V than it is at the base of Unit III. Within Unit V water content gradually decreases downhole from 29% to 22%. The downhole decrease in water content is offset at 374 mbsf to values 2% to 3% higher.

The porosity and wet-bulk density profiles follow the variation of water content at Site 931 (Fig. 23). Porosity decreases from 74% near the seafloor to 48% at 183 mbsf in the lowermost part of Unit II. Wet-bulk density increases from 1.51 to 2.01 g/cm^3 over this interval. In Unit III, porosity and wet-bulk density display greater variability in the upper 65 m of the unit and more uniform profiles over most of the lower part of the unit. From the top to the base of Unit III, porosity

Table 4. Foraminifer abundance data for Holes 931A, 931B, and 931C.

Core, section, interval (cm)	Top interval (mbsf)	Bottom interval (mbsf)	*Globorotalia menardii*	*Globorotalia tumida* (left)	*Globorotalia tumida* (right)	*Globorotalia tumida flexuosa*	*Pulleniatina obliquiloculata*	*Globigerinoides ruber* (white)	*Globigerinoides ruber* (pink)	*Globorotalia hexagonus*	*Neogloboquadrina dutertrei*	*Globorotalia trilobus trilobus*	*Globorotalia inflata*	*Globorotalia truncatulinoides* (left)	*Globorotalia truncatulinoides* (right)	*Globigerina bulloides*	*Globigerinoides trilobus sacculifer*	*Globigerinella aequilateralis*	*Orbulina universa*	*Globigerinita glutinata*	*Globigerinoides conglobatus*	*Globoquadrina conglomerata*	*Neogloboquadrina pachyderma* (right)	*Neogloboquadrina pachyderma* (left)	*Globigerina quinqueloba*	*Globigerina rubescens*	*Globorotalia scitula*	Vivianite nodules	Other planktonic foraminifers	Overall foraminifer abundance	Preservation	Abundance of benthic foraminifers	Ericson Zone	Age
155-931A-																																	
1H-TOP, 0–0	0.00	0.00	C	F	B	B	F	C	C	R	C	C	B	B	B	R	C	R	F	B	R	F	B	B	B	B	B		B	A	G	R	Z	Holocene
1H-CC, 5–14	6.05	6.14	R	B	B	B	R	F	R	B	F	R	B	C	B	B	C	R	F	B	R	R	B	B	B	B	B		F	C	G	F	Z	Holocene
2H-CC, 18–27	16.20	16.29	B	C	B	B	R	R	B	B	C	R	B	C	B	B	R	B	B	B	B	B	B	B	B	B	B		R	F	M	B	Y	late Pleist.
3H-CC, 21–30	25.74	25.83	B	B	B	B	B	F	B	B	C	F	B	F	B	B	F	B	B	B	B	B	B	B	B	B	B		B	F	M	B	Y	late Pleist.
4H-CC, 26–35	35.30	35.39	B	B	B	B	B	F	B	B	C	R	B	C	B	R	F	F	B	B	B	R	B	B	B	B	B		B	R	M	B	Y	late Pleist.
5H-CC, 49–58	44.87	44.96	B	B	B	B	B	B	B	B	B	B	B	B	B	B	B	B	B	B	B	B	B	B	B	B	B		B	B	P	B	?	late Pleist.
6H-CC, 14–23	53.98	54.07	B	B	B	B	B	C	R	B	C	B	B	C	B	B	R	B	B	B	B	B	B	B	B	B	R		R	F	M	B	Y	late Pleist.
155-931B-																																	
1H-CC, 74–83	0.74	0.83	F	F	B	B	F	C	F	B	C	C	B	B	F	B	F	B	F	B	R	R	B	B	B	B	B	B	B	A	G	B	Z	Holocene
2H-CC, 17–26	10.75	10.84	B	B	B	B	R	R	B	B	C	C	B	B	C	B	F	B	R	B	B	B	B	B	B	B	B	F	B	C	G	B	Y	late Pleist.
3H-CC, 26–35	21.06	21.15	B	B	B	B	B	R	B	B	C	C	B	B	F	B	R	B	B	B	B	B	B	B	B	B	B	C	B	R	M	B	Y	late Pleist.
4H-TOP	19.8		B	B	B	B	B	B	B	B	C	C	B	B	C	B	B	B	B	B	B	B	B	B	B	B	B	C	B	R	P	B	Y	late Pleist.
4H-CC, 30–39	30.09	30.18	B	R	B	B	B	C	R	B	C	B	B	B	C	B	F	B	B	B	B	B	B	B	B	B	R	B	R	R	M	B	Y	late Pleist.
5H-CC, 35–44	39.45	39.54	B	B	B	B	B	F	B	B	C	C	B	B	F	B	R	B	B	B	B	B	B	R	B	B	B	C	B	R	M	B	Y	late Pleist.
6H-CC, 35–44	49.10	49.19	B	B	B	B	B	F	R	B	C	F	B	B	C	B	R	B	B	B	B	B	B	B	B	B	B	C	B	R	M	B	Y	late Pleist.
7H-CC, 65–74	57.66	57.75	B	B	B	B	B	F	R	B	C	B	B	C	C	B	F	B	B	B	B	B	B	B	B	B	B	F	B	R	M	F	Y	late Pleist.
8H-CC, 27–36	68.01	68.10	B	B	B	B	B	F	B	B	C	F	B	R	B	B	F	B	B	B	B	B	B	B	B	B	B	C	B	F	M	C	Y	late Pleist.
9H-CC, 87–96	78.14	78.23	B	B	B	B	B	C	R	B	F	F	B	R	B	B	C	R	B	B	B	B	B	B	B	B	B	C	B	F	M	R	Y	late Pleist.
10X-CC, 60–69	84.57	84.66	B	B	B	B	B	C	R	B	F	F	B	R	B	B	F	B	B	B	B	B	B	B	B	B	B	R	B	F	M	B	Y	late Pleist.
11X-CC, 26–35	92.06	92.15	B	B	B	B	B	B	B	B	B	B	B	B	B	B	B	B	B	B	B	B	B	B	B	B	B	C	B	B	-	B	—	—
12X-CC, 23–32	100.56	100.65	B	B	B	B	B	A	B	B	B	B	B	B	B	B	B	B	B	B	B	B	B	B	B	B	B	A	B	B	M	B	?	?
13X-CC, 25–34	108.90	108.99	B	B	B	B	B	A	B	B	B	B	B	B	B	B	A	B	B	B	B	B	B	B	B	B	B	C	B	R	M	B	?	Pleist.
14X-CC, 13–22	119.69	119.78	B	B	B	B	B	B	B	B	B	B	B	B	B	B	B	B	B	B	B	B	B	B	B	B	B	R	B	B	M	B	—	—
15X-CC, 11–20	127.41	127.50	B	B	B	B	B	B	B	B	B	B	B	B	B	B	B	B	B	B	B	B	B	B	B	B	B	R	B	B	M	B	—	—
16X-CC, 9–18	137.64	137.73	B	B	B	B	B	B	B	B	B	B	B	B	B	B	B	B	B	B	B	B	B	B	B	B	B	F	B	B	M	B	—	—
19X-CC, 6–15	167.26	167.35	B	B	B	B	B	B	B	B	B	R	B	B	B	B	B	B	B	B	B	B	B	B	B	B	B	R	B	B	M	R	—	—
21X-CC, 37–46	184.07	184.16	B	B	B	B	B	B	B	B	B	B	B	B	B	B	B	B	B	B	B	B	B	B	B	B	B	R	B	B	P	B	—	—
23X-CC, 12–12	202.37	202.46	B	B	B	B	B	B	B	B	R	B	B	B	B	B	B	B	B	R	B	B	B	B	B	B	B	B	B	B	M	B	—	—
24X-CC	219.1		B	B	B	B	B	C	B	B	C	C	B	C	B	B	B	B	B	B	B	B	B	B	B	B	B	R	B	R	M	B	—	—
25X-CC, 20–29	224.97	225.06	C	R	B	B	C	C	B	B	C	F	B	C	B	B	B	B	B	R	B	B	B	B	B	B	B	F	B	C	M	F	?	Pleist.
26X-CC, 18–27	233.09	233.18	B	B	B	B	B	B	B	B	B	B	B	B	B	B	B	B	B	B	B	B	B	B	B	B	B	F	B	B	P	B	—	—
27X-CC, 26–35	248.24	248.33	B	B	B	B	B	R	B	B	B	B	B	B	B	B	B	B	B	R	B	B	B	B	B	B	B	B	B	B	P	B	RW?	?
28X-CC, 27–36	254.96	255.05	B	B	B	B	C	F	B	B	C	C	B	B	F	B	B	B	B	B	B	B	B	B	B	B	B	R	B	R	M	B	?	Pleist.
29X-CC, 8–17	264.39	264.48	R	B	B	B	B	F	B	B	B	R	B	B	B	B	B	B	B	B	B	B	B	B	B	B	B	B	B	R	M	B	?	Pleist.
30X-CC, 21–30	276.8	276.9	R	B	B	B	C	C	B	R	C	R	B	B	C	B	B	B	B	B	B	B	B	B	B	B	B	F	B	F	M	F	?	Pleist.
31X-CC, 14–23	287.30	287.39	B	R	B	B	C	C	R	B	C	B	B	F	C	B	F	B	R	B	B	R	B	B	B	B	B	B	B	F	M	F	?	Pleist.
32X-CC, 57–66	295.64	295.73	B	C	B	B	C	C	B	B	C	C	B	B	B	B	C	B	R	B	R	R	B	B	B	B	B	R	B	F	M	F	?	Pleist.
33X-CC, 37–46	302.57	302.66	B	R	B	B	B	R	B	B	B	R	B	B	B	B	B	B	B	B	B	B	B	B	B	B	B	C	B	R	M	F	?	Pleist.
34X-CC, 3–12	311.04	311.13	R	B	B	B	C	F	B	B	C	C	B	B	R	B	F	B	B	B	B	B	B	B	B	B	B	F	B	R	M	F	?	Pleist.
35X-CC, 28–37	320.48	320.57	C	C	B	R	B	C	B	B	C	B	B	B	B	B	C	B	F	B	B	R	B	B	B	B	B	B	R	A	G	C	?	Pleist.
36X-4, 83–85	330.53	330.55	B	C	B	B	F	F	B	B	F	F	B	B	C	B	R	R	R	B	B	B	B	B	B	B	B	B	B	C	G	R	?	Pleist.
36X-5, 59–61	331.69	331.71	R	R	B	B	F	F	B	B	C	F	B	B	R	B	B	B	R	B	B	R	B	B	B	B	B	R	B	F	M	R	?	Pleist.
36X-5, 89–91	331.99	332.01	C	C	B	B	F	C	R	B	C	F	B	B	B	B	B	B	B	B	B	B	B	B	B	B	B	B	B	C	G	F	?	Pleist.
36X-5, 100–102	332.10	332.12	F	C	B	B	F	C	F	B	B	F	B	B	F	B	R	B	R	B	B	B	B	B	B	B	B	B	B	A	G	B	?	Pleist.
36X-5, 109–111	332.19	332.21	B	C	B	B	R	C	R	B	B	R	B	B	R	B	B	B	B	B	B	B	B	B	B	B	B	B	B	C	P	R	?	Pleist.
36X-6, 124–126	333.84	333.86	B	C	B	F	F	C	R	R	C	C	B	B	C	B	B	B	B	B	B	B	B	B	B	B	B	R	R	C	G	R	?	Pleist.
36X-CC, 31–40	334.41	334.50	C	C	B	C	F	C	F	B	R	C	B	B	C	B	F	B	R	R	R	B	B	B	B	B	B	B	B	A	G	F	?	Pleist.
37X-CC, 24–33	340.53	340.62	C	C	B	B	C	C	R	B	C	F	B	C	B	B	F	B	F	B	F	B	B	B	B	B	B	B	B	A	M	B	?	Pleist.
38X-4, 31–33	349.21	349.23	B	B	B	B	B	B	B	B	B	B	B	B	B	B	B	B	B	B	B	B	B	B	B	B	B	B	B	B	P	B	—	
38X-4, 36–38	349.26	349.28	B	C	B	B	C	C	B	B	C	C	B	B	B	B	B	B	R	B	R	B	B	B	B	B	B	B	B	A	M	R	?	mid. Pleist.
38X-4, 46–48	349.36	349.38	B	C	B	B	F	C	B	B	C	C	B	B	R	B	R	B	B	B	R	B	B	B	B	B	B	F	R	A	G	F	?	mid. Pleist.

Table 4 (continued).

Core, section, interval (cm)	Top interval (mbsf)	Bottom interval (mbsf)	*Globorotalia menardii*	*Globorotalia tumida* (left)	*Globorotalia tumida* (right)	*Globorotalia tumida flexuosa*	*Pulleniatina obliquiloculata*	*Globigerinoides ruber* (white)	*Globigerinoides ruber* (pink)	*Globorotalia hexagonus*	*Neogloboquadrina dutertrei*	*Globorotalia trilobus trilobus*	*Globorotalia inflata*	*Globorotalia truncatulinoides* (left)	*Globorotalia truncatulinoides* (right)	*Globigerina bulloides*	*Globigerinoides trilobus sacculifer*	*Globigerinella aequilateralis*	*Orbulina universa*	*Globigerinita glutinata*	*Globigerinoides conglobatus*	*Globoquadrina conglomerata*	*Neogloboquadrina pachyderma* (right)	*Neogloboquadrina pachyderma* (left)	*Globigerina quinqueloba*	*Globigerina rubescens*	*Globorotalia scitula*	Vivianite nodules	Other planktonic foraminifers	Overall foraminifer abundance	Preservation	Abundance of benthic foraminifers	Ericson Zone	Age
38X-4, 96–98	349.86	349.88	B	C	B	B	F	C	R	B	C	F	B	B	C	B	B	B	R	B	B	B	B	B	B	B	B	R	B	C	G	R	?	mid. Pleist.
38X-CC, 42–51	355.71	355.80	B	C	B	B	C	C	R	B	C	C	B	B	C	B	B	B	B	B	B	B	B	B	B	B	B	B	B	C	M	F	?	mid. Pleist.
39X-CC, 46–35	361.65	361.74	C	C	B	B	F	C	B	B	C	R	R	C	B	B	R	B	B	B	B	B	B	B	B	B	B	B	B	F	M	R	?	mid. Pleist.
40X-CC, 34–43	372.36	372.45	B	A	B	B	B	C	B	B	C	B	B	B	B	B	B	B	B	B	B	B	B	B	B	B	B	A	B	F	G	R	?	mid. Pleist.
41X-CC, 12–21	381.14	381.23	B	B	B	B	B	B	B	B	B	B	B	B	B	B	B	B	B	B	B	B	B	B	B	B	B	A	B	B	P	B	—	—
42X-CC, 14–23	391.98	392.07	B	R	B	B	B	B	B	B	B	B	B	B	B	B	B	B	B	B	B	B	B	B	B	B	B	A	B	B	P	R	—	—
43X-CC, 24–33	402.52	402.63	B	B	B	B	B	B	B	B	B	B	B	B	B	B	B	B	B	B	B	B	B	B	B	B	B	A	B	B	P	B	—	—
44X-CC, 45–54	411.76	411.85	B	B	B	B	B	B	B	B	B	B	B	B	B	B	B	B	B	B	B	B	B	B	B	B	B	A	B	B	P	B	—	—
45X-CC, 30–39	418.10	418.19	B	B	B	B	B	B	B	B	B	B	B	B	B	B	B	B	B	B	B	B	B	B	B	B	B	A	B	B	P	B	—	—
155-931C-																																		
1H-1, 10–20	0.10	0.20	F	F	B	R	R	C	R	B	C	C	B	B	F	B	C		R	B	B		B	B	B	B	B		C	C	G	B	Z	Holocene
1H-CC, 2–10	4.00	4.10	B	F	B	B	B	C	R	B	C	C	B	B	C	B	R		B	B	B		B	B	B	B	B		F	C	G	B	Z	Holocene
2H-CC, 22–32	13.83	13.93	B	B	B	B	B	C	B	B	C	C	B	B	F	B	R		B	B	B		B	B	B	B	B		B	R	M	B	Y	late Pleist.
3H-CC, 18–28	23.81	23.91	B	B	B	B	B	A	B	B	A	C	B	B	C	B	B		B	B	B		B	B	B	B	B		B	R	M	B	Y	late Pleist.
4H-CC, 17–27	33.15	33.25	B	B	B	B	B	C	F	B	C	C	B	B	C	B	F		B	B	B		B	B	B	B	B		B	R	G	B	Y	late Pleist.

Note: A blank entry in the table indicates that the taxon was not recorded.

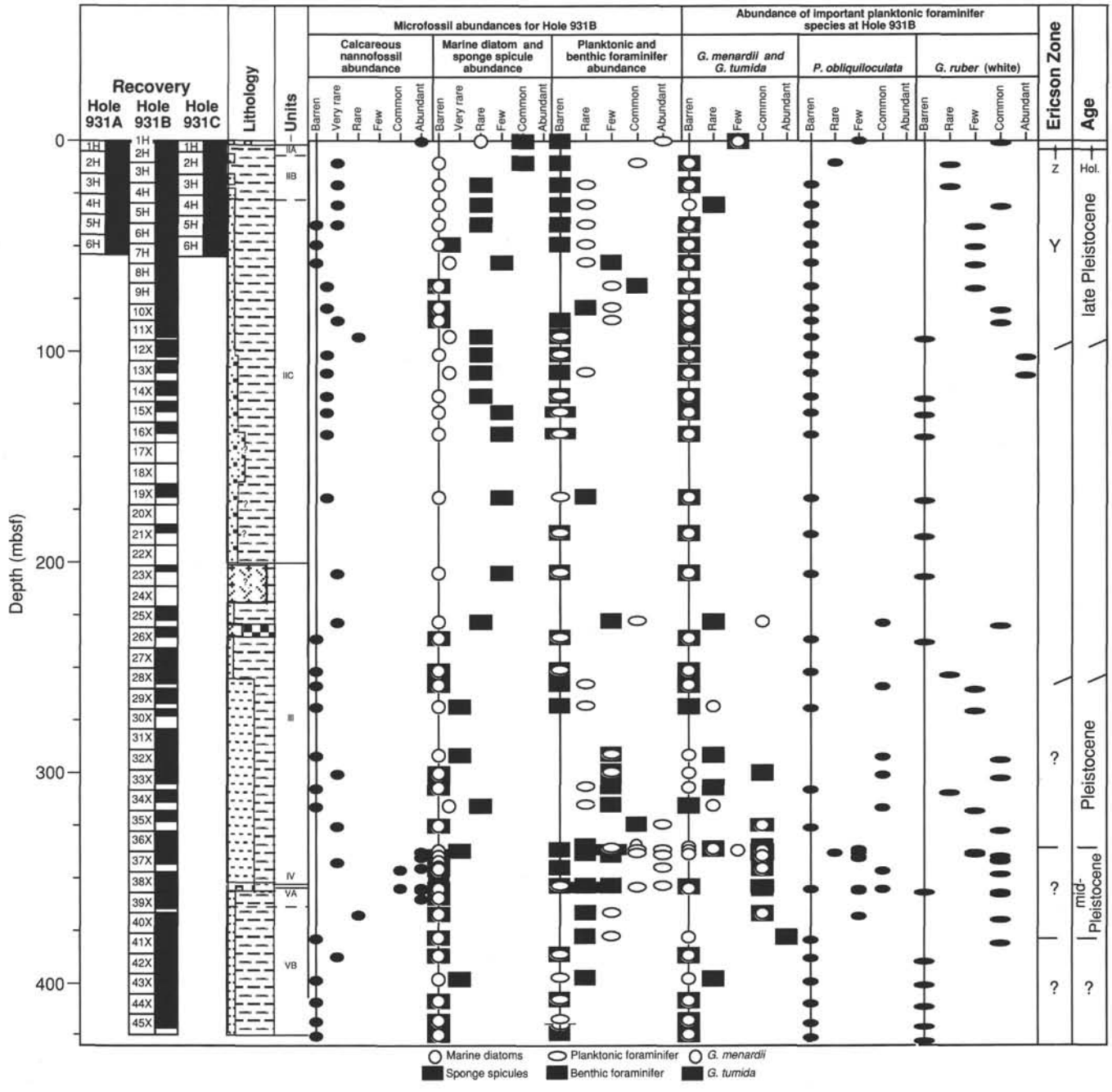

Figure 14. Biostratigraphic summary for Site 931.

decreases from approximately 50% to 40%, and wet-bulk density increases from about 1.90 to 2.15 g/cm^3. As with the water content profile, profiles of porosity and wet-bulk density are more uniform in Unit V. Over this interval, porosity decreases gradually (53%–44%) and wet-bulk density increases (≈1.90–2.10 g/cm^3).

Wet-bulk density values determined by the GRAPE are typically 0.2 to 0.4 g/cm^3 less than the wet-bulk densities determined by discrete-sample measurements. In the uppermost 100 m of Hole 931B, gas-induced sediment expansion is primarily responsible for the underestimation of wet-bulk density by the GRAPE. Below 100 mbsf, remolded sediment and incomplete filling of the core liner also contribute to the lower densities. Although the GRAPE bulk density is low, the general pattern of density variation in Hole 931B is reflected in the data.

The average grain density of sediment recovered at Site 931 varies about a mean of 2.76 g/cm^3, with the bulk of the values between 2.70 and 2.85 g/cm^3 (Fig. 23). The samples were taken primarily from silty clays and clays; however, 14 muddy sand intervals were sampled for grain density. The mean grain density of the sand, 2.77 g/cm^3, is not significantly different from that of the more clay-rich sediment, 2.76 g/cm^3.

Overall, the sediment index properties at Site 931 display patterns typical for the self-consolidation of fine-grained terrigenous sediment. Low water content and porosity and high bulk density of the sediment in Unit III are consistent with the interpretation that this unit is a debris-flow deposit and that some of this sediment possibly underwent consolidation before being transported downslope. Sediment of Unit V displays variations in water content, porosity, and bulk den-

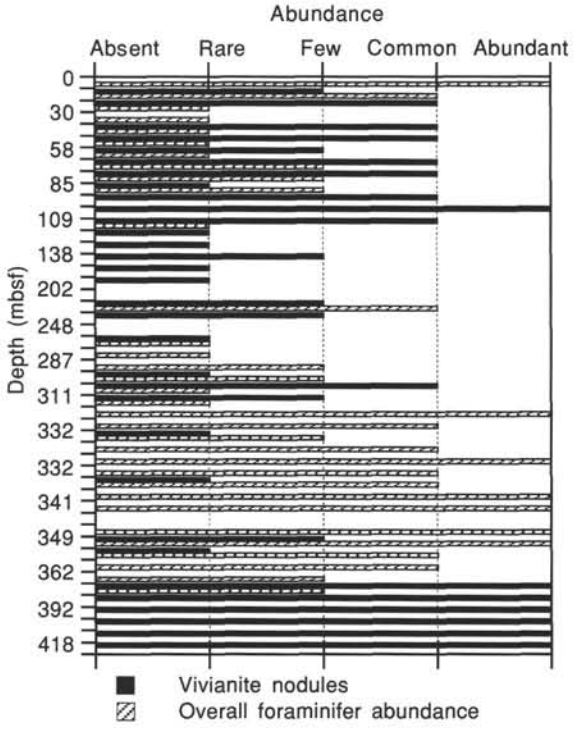

Figure 15. Vivianite and planktonic foraminifer abundances for Hole 931B.

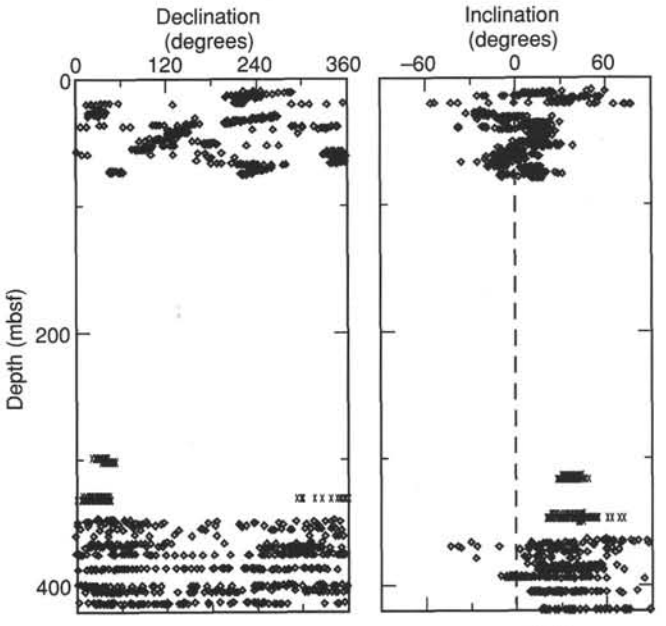

Figure 16. Declination and inclination vs. depth for archive-half core sections from Hole 931B. Diamonds = AF demagnetizations to 25 mT; X = AF demagnetizations to 10 mT. Declinations have not been corrected to Tensor tool azimuths.

sity typical of self-consolidation, similar to sediment in the upper part of the section at Site 931. The slightly higher water content of these sediments (for their present burial depth) suggests that rapid deposition of the overlying, thick debris-flow deposits has inhibited sediment dewatering.

Compressional-wave Velocity

Gas-expansion-induced fractures in sediment of the upper part of Site 931 and the pervasive biscuiting and drilling disturbance in sediment from the lower part of Hole 931B limited compressional-wave velocity measurements to those obtained by the PWL in the upper 6 m of the sediment column. The PWL measurements gave an average corrected in-situ velocity of 1485 m/s for the interval 0–6 mbsf.

Shear Strength

Undrained shear strength was measured on Core 931A-1H and most of the Hole 931B cores using the motorized shear vane (Table 13). Below 162 mbsf, measurements of unconfined compressive strength also were made to provide a comparison with undrained

Table 5. Spore and pollen abundance data for Holes 931A and 931B.

Core, section, interval (cm)	Top interval (mbsf)	Bottom interval (mbsf)	Pollen and spores			Dinocysts	Wood/ carbonized particles	Ericson Zone (inferred from forams)	Age (inferred from forams)
			Abundance	Preservation	Major types recorded				
155-931A-									
1H-Ml, 0–0	0.00	0.00	r	m	SP, Monosulcus	c	f	Z	Holocene
1H-1, 50–54	0.50	0.54	b			f	f	Z	Holocene
1H-CC, 14–15	6.14	6.15	b			f	r	?Y	late Pleist.?
155-931B-									
1H-CC, 83–84	0.83	0.84	r	m	Monolete (psilate) spore	b	f	Z	Holocene
2H-4, 33–3	5.63	5.65	a	m	Proteaceae, TCP, Trilete spore, *Alnus*	b	c	Y	late Pleist.
2H-6, 17–19	8.47	8.49	c	m	Ericaceae, Cyperaceae, Cyatheaceae, *Cecropia*	b	a	Y	late Pleist.
2H-7, 36–38	10.16	10.18	c	m	Gramineae, TC (psilate), TCP (reticulate)	b	c	Y	late Pleist.
3H-1, 52–54	10.82	10.84	f	m	Cyperaceae, monolete (psilate) spore	b	a	Y	late Pleist.
4H-2, 30–32	12.10	12.12	c	g	Cyperaceae, monolete (psilate) spore, Cyatheaceae, Monosulcus (scabrate)	b	a	Y	late Pleist.
3H-2, 119–121	12.99	13.01	c	g	Rhizophoraceae, SP	b	c	Y	late Pleist.
3H-3, 34–36	13.64	13.66	f	m	TC (scabrate), Gramineae	c	f	Y	late Pleist.
3H-4, 13–15	14.93	14.95	b			b	r	Y	late Pleist.
12X-CC, 32–33	100.65	100.66	b			b	a	?	?
25X-4, 74–76	224.34	224.36	b			b	f	?	Pleist.
35X-3, 31–33	318.81	318.83	r	p	Cyperaceae	b	f	?	Pleist.
36X-5, 100–102	332.10	332.12	c	p	TCP (scabrate), Gramineae, monolete (psilate) spore	b	f	?	Pleist.
36X-5, 115–117	332.25	332.27	b			r	a	?	Pleist.
37X-1, 30–34	335.10	335.14	a	p	Cyatheaceae, monolete (psilate) spore	b	c	?	Pleist.
38X-CC, 51–52	353.80	353.81	b				f	?	mid Pleist.
43X-CC, 33–34	402.63	402.64	c	m	Cyatheaceae, monolete (psilate) spore	b	f	—	—

Notes: TC = triporate; TCP = tricolporate; SP = stephanoporate.

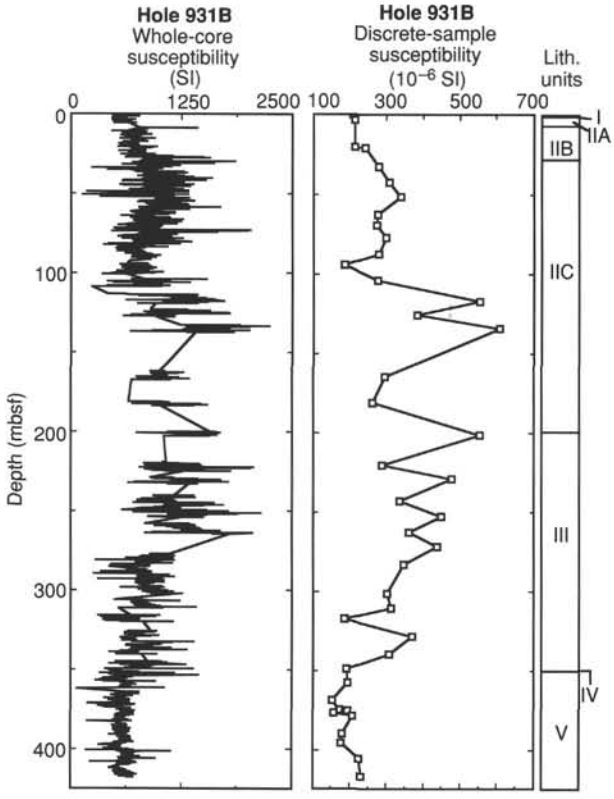

Figure 17. Whole-core and discrete-sample magnetic susceptibility results, compared to the lithostratigraphic units.

shear strength in anticipation that shear strengths would eventually exceed the capacity of the motorized shear vane. Sediment between 300 and 350 mbsf was too stiff to measure with the shear vane. Adjacent measurements of undrained shear strength and assumed undrained shear strength derived from unconfined compressive strength correlate well (Fig. 24).

The shear-strength profile can be divided into five parts. From 0 to 83 mbsf, shear strength gradually increases with depth to 40 kPa at about 69 mbsf. Below 69 mbsf, the trend reverses and the strength decreases to 20 kPa at 83 mbsf. Very little scatter of values occurs within this interval. From 83 to 235 mbsf, shear strength increases from 30 kPa to 100 kPa with increasing variability downhole. Below 235 mbsf, shear strength is highly variable and commonly increases with depth within individual cores, suggesting that the coring process has affected the strength. This lower part of the shear-strength profile is divided into three parts by the occurrence of sediment between 297 and 348 mbsf that is too stiff to test with the shear vane. The capacity of the pocket penetrometer (220 kPa) was routinely exceeded in this sediment.

Resistivity

Longitudinal and transverse resistivity were determined for intervals coinciding with those sampled for index properties (Table 14). Distinct breaks in the longitudinal resistivity profile coincide with the lithologic unit boundaries at Site 931 (Fig. 25). Within the upper part of Unit II, two intervals of rapid increase in resistivity with depth end with an abrupt decrease in resistivity. From the base of the lower interval (approximately 83 mbsf) to the base of Unit II, there is little change in resistivity. The change in resistivity at 83 mbsf roughly coincides with the transition from thinly laminated silty clays to more thickly bedded silty clays and sand intervals (Fig. 5). Resistivity is highly variable in the interval of mass-transport deposits in the upper 65 m of Unit III.

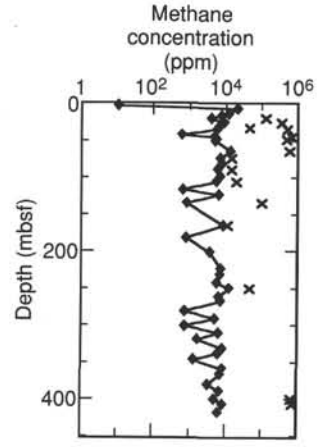

Figure 18. Methane concentrations at Site 931. Headspace (diamond) and vacutainer (×) samples are plotted.

Table 6. Gas concentrations in sediments from Site 931.

Core, section, interval (cm)	Depth (mbsf)	Sed. temp.* (°C)	Methane HS (ppm)	Methane VAC (ppm)
155-931A-				
1H-4, 0–5	4.50	2	0	
2H-8, 0–5	15.31	3	11,721	
3H-5, 0–5	21.60	3	3,888	132,395
4H-7, 0–5	34.10	3	6,219	45,588
5H-7, 0–5	43.56	4	597	
6H-6, 0–5	51.30	4	5,133	
155-931B-				
2H-6, 0–5	8.30	2	21,388	
3H-6, 0–5	17.80	3	7,639	
4H-6, 0–5	27.30	3	9,148	359,570
5H-6, 0–5	36.10	4	5,596	514,638
6H-6, 0–5	46.30	4	4,900	706,902
7H-2, 0–5	49.80	4	5,404	494,974
8H-6, 0–5	65.30	5	13,596	612,098
9H-6, 0–5	74.80	5	7,159	14,820
10X-5, 0–5	82.25	5	7,974	
11X-5, 0–5	90.30	6	5,760	14,820
12X-5, 0–5	99.90	6	7,116	
13X-3, 0–5	106.50	6	5,420	19,392
14X-4, 0–5	117.56	7	640	
15X-2, 0–5	124.30	7	6,655	
16X-3, 0–5	135.50	8	829	101,601
19X-4, 0–5	166.00	9	8,700	10,800
21X-2, 0–5	182.20	10	791	
23X-2, 0–5	201.30	10	3,627	
25X-4, 0–5	223.60	11	7,261	
26X-3, 0–5	231.70	12	7,096	
27X-4, 0–5	242.90	12	5,614	
28X-3, 0–5	249.97	12	12,676	47,275
29X-4, 0–5	262.20	13	6,510	
30X-CC, 14–15	267.44	13	7,330	
31X-4, 0–5	281.40	14	756	
32X-4, 0–5	291.10	14	5,144	
33X-4, 0–5	300.70	15	753	
34X-4, 0–5	310.30	15	6,498	
35X-3, 0–5	318.50	15	1,694	
36X-5, 0–5	331.10	16	8,149	
37X-3, 0–5	337.80	16	6,098	
38X-2, 0–5	345.90	17	1,319	
39X-4, 0–5	358.60	17	8,071	
40X-3, 0–5	365.96	17	7,230	
41X-5, 0–5	379.40	18	3,364	
42X-5, 0–5	388.90	18	7,038	
43X-6, 0–5	399.47	19	5,062	694,800
44X-5, 0–5	406.38	19	8,666	762,777
45X-5, 0–5	417.60	20	6,536	

Notes: HS = headspace; VAC = vacutainer. Geothermal gradient = 42°C/km. Bottom-water temperature = 2°C. *See "In-situ Temperature Measurements" section, this chapter.

Table 7. Elemental and organic carbon compositions of sediments from Site 931.

Core, section, interval (cm)	Depth (mbsf)	IC (%)	$CaCO_3$* (%)	TC (%)	TOC (%)	TN (%)	TS (%)	[C/N]a
155-931A-								
1H-1, 4–5	0.04	4.65	38.7	5.11	0.46	0.06	0.14	9
1H-1, 27–28	0.27	5.89	49.1	6.10	0.21	0.03	0.09	7
1H-1, 64–65	0.64	1.77	14.7	2.28	0.51	0.06	0.12	9
1H-1, 89–90	0.89	1.34	11.2	1.79	0.45	0.07	0.10	8
155-931B-								
2H-2, 14–15	2.44	0.11	0.9	0.71	0.60	0.07	0.13	10
2H-4, 32–33	5.62	0.10	0.8	0.94	0.84	0.07	0.28	13
2H-4, 35–36	5.65	0.23	1.9	0.84	0.61	0.06	7.02	12
2H-6, 35–36	8.65	0.19	1.6	0.90	0.71	0.08	6.54	10
3H-4, 34–35	15.14	0.26	2.2	1.31	1.05	0.10	0.31	12
3H-6, 40–43	18.20	0.23	1.9	1.29	1.06	0.13	0.19	10
4H-1, 12–13	19.92	0.25	2.1	1.24	0.99	0.11	0.11	10
4H-3, 50–51	23.30	0.33	2.7	1.27	0.94	0.10	0.08	11
4H-4, 108–109	25.38	0.33	2.7	1.41	1.08	0.11	0.06	12
5H-1, 13–14	29.43	0.35	2.9	1.31	0.96	0.10	0.07	12
5H-4, 50–51	34.30	0.34	2.8	1.14	0.80	0.09	0.07	10
5H-7, 54–55	38.14	0.37	3.1	1.33	0.96	0.11	0.07	10
6H-3, 33–34	42.13	0.35	2.9	1.36	1.01	0.11	0.06	11
6H-4, 32–33	43.62	0.35	2.9	1.19	0.84	0.09	0.05	11
6H-6, 49–50	46.79	0.32	2.7	1.33	1.01	0.10	0.15	11
6H-7, 65–66	48.45	0.28	2.3	1.30	1.02	0.10	0.08	12
7H-1, 46–47	48.76	0.31	2.6	1.24	0.93	0.09	0.00	12
7H-4, 30–31	53.10	0.26	2.2	1.21	0.95	0.09	0.07	12
7H-6, 55–56	56.35	0.33	2.7	1.25	0.92	0.09	0.05	12
8H-2, 16–17	59.46	0.34	2.8	1.27	0.93	0.10	0.05	11
8H-4, 88–89	63.18	0.51	4.2	1.48	0.97	0.09	0.04	12
9H-2, 7–8	68.87	0.32	2.7	1.35	1.03	0.15	0.04	8
9H-3, 49–50	70.79	0.30	2.5	1.27	0.97	0.10	0.13	11
9H-4, 80–81	72.60	0.31	2.6	1.24	0.93	0.08	0.08	14
9H-6, 46–47	75.26	0.33	2.7	1.27	0.94	0.14	0.08	8
10X-3, 7–8	79.87	0.16	1.3	0.55	0.39	0.03	0.00	17
10X-3, 10–11	79.90	0.41	3.4	1.36	0.95	0.12	0.06	9
11X-4, 98–99	89.78	0.39	3.2	1.38	0.99	0.10	0.00	11
11X-5, 50–51	90.80	0.44	3.7	1.42	0.98	0.16	0.05	7
12X-1, 67–68	94.57	0.41	3.4	1.34	0.93	0.14	0.00	8
12X-1, 105–106	94.95	0.43	3.6	1.33	0.90	0.12	0.04	8
12X-4, 7–8	98.47	0.45	3.7	1.41	0.96	0.13	0.00	9
13X-1, 43–45	103.93	0.27	2.2	0.95	0.68	0.07	0.14	11
13X-3, 37–38	106.87	0.28	2.3	1.25	0.97	0.11	0.12	10
14X-4, 47–48	118.03	0.26	2.2	1.01	0.75	0.06	0.05	13
15X-1, 135–136	124.15	0.35	2.9	1.35	1.00	0.10	0.07	11
16X-2, 120–121	135.20	0.17	1.4	0.29	0.12	0.03	0.01	5
16X-3, 60–61	136.10	0.21	1.7	0.86	0.65	0.07	0.03	12
19X-3, 116–117	165.66	0.37	3.1	1.36	0.99	0.11	0.06	10
19X-4, 111–112	167.11	0.34	2.8	1.91	1.57	0.13	0.15	14
21X-2, 38–39	182.58	0.06	0.5	0.16	0.10	0.03	0.02	4
21X-2, 113–114	183.33	0.28	2.3	1.18	0.90	0.10	0.07	10
23X-1, 74–75	200.54	0.25	2.1	0.68	0.43	0.04	0.00	13
25X-2, 53–54	221.13	0.19	1.6	0.97	0.78	0.10	0.04	9
25X-2, 83–84	221.43	0.34	0.0	0.76	0.42	0.05	0.00	9
25X-3, 34–35	222.44	1.05	0.0	1.80	0.75	0.11	0.02	8
26X-2, 77–78	230.97	0.08	0.0	0.44	0.36	0.04	0.20	11
26X-3, 23–24	231.93	0.04	0.0	0.09	0.05	0.01	0.00	4
27X-1, 10–11	238.50	0.29	2.4	1.07	0.78	0.09	0.16	10
27X-4, 83–84	243.73	0.31	2.6	1.19	0.88	0.10	0.15	10
28X-3, 111–112	251.08	0.21	0.0	0.56	0.35	0.04	0.00	11
28X-4, 91–92	252.38	0.23	1.9	0.87	0.64	0.07	0.06	11
29X-4, 96–97	263.16	0.35	2.9	1.20	0.85	0.09	0.06	11
29X-5, 35–36	264.05	0.07	0.6	0.14	0.07	0.02	0.01	4
31X-1, 58–59	277.48	0.31	2.6	1.12	0.81	0.09	0.05	10
31X-4, 30–31	281.70	0.30	2.5	1.19	0.89	0.10	0.05	10
32X-4, 39–40	291.49	0.36	3.0	1.17	0.81	0.10	0.05	9
32X-5, 99–101	293.59	0.29	2.4	1.14	0.85	0.10	0.04	10
32X-6, 80–81	294.90	0.48	4.0	0.99	0.51	0.06	0.13	11
33X-1, 88–89	297.08	0.26	2.2	1.15	0.89	0.11	0.12	10
33X-3, 38–39	299.58	0.31	2.6	1.13	0.82	0.09	0.09	11
34X-1, 31–32	306.11	0.25	2.1	0.84	0.59	0.09	0.21	8
34X-4, 69–70	310.99	0.16	1.3	0.92	0.76	0.09	0.09	10
35X-1, 20–21	315.70	1.85	15.4	2.51	0.66	0.09	1.53	9
35X-1, 54–55	316.04	0.13	1.1	0.78	0.65	0.11	1.14	7
35X-3, 105–106	319.55	0.39	3.2	1.02	0.63	0.08	0.13	9
36X-5, 99–100	332.09	3.73	31.1	4.07	0.34	0.07	0.01	6
36X-5, 137–138	332.47	0.42	3.5	1.05	0.63	0.09	0.07	8
37X-2, 96–98	337.26	0.44	3.7	1.10	0.66	0.09	0.32	9
37X-3, 130–132	339.10	1.53	12.7	2.04	0.51	0.12	0.12	5
38X-4, 29–30	349.19	0.56	4.7	1.14	0.58	0.10	0.29	7
38X-4, 40–41	349.30	2.31	19.2	2.54	0.23	0.11	0.04	3
38X-4, 75–76	349.65	0.77	6.4	1.34	0.57	0.10	0.17	7
38X-CC, 19–20	353.48	1.35	11.2	1.85	0.50	0.09	0.29	6
39X-4, 68–69	359.28	0.17	1.4	0.83	0.66	0.10	0.25	7
39X-5, 100–101	361.10	0.17	1.4	0.60	0.43	0.06	0.53	8
40X-2, 18–19	364.64	0.34	2.8	1.15	0.81	0.10	0.08	10
40X-3, 94–95	366.90	0.34	2.8	1.15	0.81	0.10	0.00	10
40X-3, 108–109	367.04	0.43	3.6	1.28	0.85	0.10	0.04	10
41X-3, 49–50	376.89	0.23	1.9	1.18	0.95	0.12	0.05	9
41X-6, 49–50	381.39	0.35	2.9	1.24	0.89	0.12	0.05	9
42X-4, 90–91	388.30	0.45	3.7	1.38	0.93	0.11	0.08	10

Table 7 (continued).

Core, section, interval (cm)	Depth (mbsf)	IC (%)	$CaCO_3$* (%)	TC (%)	TOC (%)	TN (%)	TS (%)	[C/N]a
42X-4, 127–128	388.67	0.37	3.1	1.21	0.84	0.12	0.05	8
43X-3, 103–105	396.00	0.90	7.5	1.75	0.85	0.09	0.29	11
43X-4, 110–111	397.57	0.26	2.2	1.15	0.89	0.11	0.09	9
44X-3, 106–107	404.87	0.27	2.2	1.15	0.88	0.10	0.05	10
44X-5, 12–13	406.50	0.31	2.6	1.13	0.82	0.10	0.04	9
45X-2, 40–41	413.50	0.33	2.7	1.12	0.79	0.10	0.04	9
45X-4, 38–39	416.48	0.30	2.5	1.05	0.75	0.10	0.05	9
45X-4, 133–134	417.43	0.36	3.0	1.06	0.70	0.09	0.03	9

*Calculated assuming all IC is calcite.

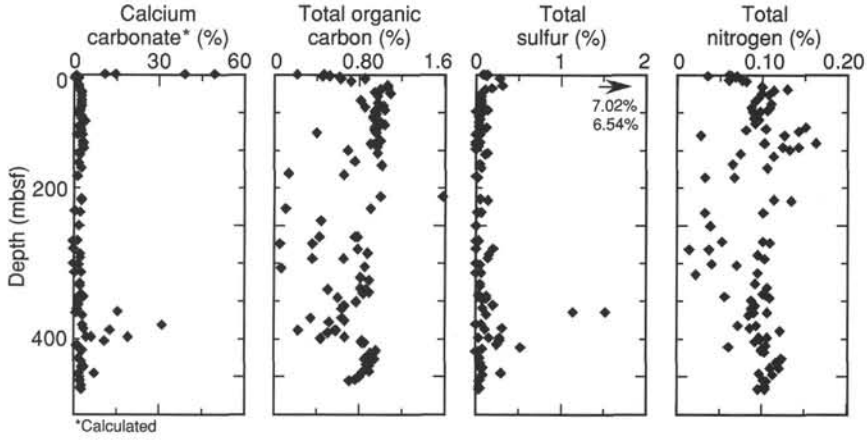

Figure 19. Concentration profiles of carbonate, total organic carbon, total sulfur, and total nitrogen in Holes 931A and 931B.

Table 8. HI values derived from Rock-Eval pyrolysis of selected samples from Site 931.

Core, section, interval (cm)	Depth (mbsf)	HI (mg HC/g TOC)	TOC (%)
155-931A-			
1H-1, 64–65	0.64	115	1.08
155-931B-			
4H-4, 108–109	25.38	28	0.52
6H-7, 65–66	48.45	100	1.03
9H-2, 7–8	68.87	80	1.03
15X-1, 135–136	124.15	87	1.00
19X-4, 111–112	167.11	83	1.57
35X-1, 20–21	315.70	27	0.66

Resistivity anisotropy is characterized by wide scatter of values (Fig. 25). However, the thinly laminated silty clay intervals of Unit II and Unit V are generally characterized by negative anisotropy. The prominent negative peak in anisotropy coincides with the local longitudinal resistivity maximum in laminated sediment at 50 mbsf in Unit II.

The crossplot of resistivity and porosity (Fig. 26) shows that the lithologic units cluster in distinct groups. These groups reflect the general decrease in porosity with increasing burial depth, with two exceptions. In Unit IIC, porosity decreases uniformly with depth; however, there are three different trends in the resistivity profile, and as a consequence greater scatter on the resistivity/porosity crossplot. In Unit III, the lower, more clay-rich interval of uniform porosity plots along the trend of increasing resistivity with decreasing porosity. In contrast, the upper part of Unit III, with more lithologic variation, is characterized by more scatter in the resistivity and porosity data.

It is assumed that resistivity varies in sediment as a function of sediment structure and pore-water salinity. Because there is little change in the salinity of the pore waters (Fig. 20), the variation in resistivity is most likely a result of differences in sediment fabric. The pattern of relatively consistent negative anisotropy coinciding with well-bedded intervals of Units II and V and the wide resistivity variation in the debris-flow deposit of Unit III support the inference that changes in sediment structure are primarily responsible for variation in sediment resistivity.

Thermal Conductivity

Thermal conductivity displays a general inverse relationship with porosity (Fig. 27; Table 15). The correlation between thermal conductivity and porosity is weak (R = 0.66) because of the large variation in the conductivity data. The scatter in the conductivity data is most likely the result of gas-induced sediment expansion resulting in poor contact between the sediment and the conductivity probes. The general trend and variability of the conductivity and porosity data at Site 931 is similar to that observed at Site 930.

DOWNHOLE LOGGING

Logging Operations and Quality of Logs

At Site 931, we acquired a complete suite of logging data with the Quad-combination, Formation MicroScanner (FMS), geochemical logging (GLT), and geological high-sensitivity magnetic (GHMT-A) tool strings (see "Explanatory Note" chapter, this volume). The Lamont-Doherty temperature tool (TLT) was attached to the bottom of the Quad-combination and GLT tool strings. The borehole of Hole 931B was conditioned with sepiolite drilling mud mixed with seawater before we drilled the last two cores. The base of the bottom-hole assembly (BHA) was set at 93 mbsf. The Quad-combination tool string failed during the logging run down the drill pipe. After retrieving it, we discovered that both the NGT and array-sonic tools had flooded

Table 9. Interstitial water chemistry, Site 931.

Core, section, interval (cm)	Depth (mbsf)	Salinity	pH	Alkalinity (mM)	Cl^- (mM)	Mg^{2+} (mM)	Ca^{2+} (mM)	K^+ (mM)	HPO_4^{2-} (μM)	SO_4^{2-} (mM)	NH_4^+ (mM)	H_4SiO_4 (μM)	Na^+ (mM)	Fe^{2+} (μM)	Mn^{2+} (μM)
155-931C-															
1H-1, 20–30	0.20	35.0	7.63	4.19	553	54.5	12.2	12.4	10.4	26.33	0.00	289	464	9.9	2.5
1H-1, 145–150	1.45	35.0	7.70	8.45	553	52.3	11.0	12.9	13.8	22.31	0.33	235	466	29.3	63.3
1H-2, 145–150	2.95	34.0	7.63	13.02	550	47.8	9.5	12.3	15.4	15.76	0.87	222	467	33.1	33.9
1H-3, 93–98	3.93	34.0	7.58	16.65	553	47.7	9.1	11.9	31.7	12.21	1.14	248	468	19.7	29.6
2H-1, 145–150	5.55	34.0	8.01	27.05	556	41.9	7.3	10.8	273.2	1.75	2.22	235	476	7.3	14.4
2H-2, 145–150	7.05	34.0	7.73	25.41	557	43.1	7.4	10.7	108.7	0.20	2.29	330	469	8.5	14.3
2H-3, 145–150	8.55	34.0	7.65	23.34	557	43.8	7.0	10.6	34.0	0.10	3.07	323	465	21.5	8.7
2H-4, 145–150	10.05	33.0	7.78	21.81	561	42.1	6.3	10.8	20.5	0.08	2.99	375	473	45.4	6.0
2H-5, 145–150	11.55	33.0	7.63	20.50	560	43.2	6.4	11.2	35.8	0.00	3.98	357	466	104.4	4.5
2H-6, 145–150	13.05	33.0	7.60	19.08	560	42.6	6.6	10.1	13.3	0.14	3.91	325	467	85.9	3.3
3H-1, 145–150	15.38	32.5	7.62	13.49	561	42.1	5.4	9.8	12.1	0.70	5.37	283	466	90.0	2.0
3H-2, 145–150	16.88	33.0	7.58	14.48	560	42.2	5.2	9.7	11.7	0.91	5.32	250	466	39.2	2.2
3H-3, 145–150	18.38	32.5	7.60	13.56	562	40.5	4.9	9.3	10.0	0.52	3.80	238	473	23.5	2.9
3H-5, 145–150	21.38	32.5	7.50	12.21	560	41.8	5.0	9.7	8.6	1.81	6.06	302	467	24.8	2.0
3H-7, 145–150	23.91	32.0	7.50	11.99	562	40.5	4.9	8.6	10.9	0.09	6.43	337	468	29.0	3.3
4H-1, 145–150	25.69	32.5	7.46	11.44	561	43.1	5.0	8.3	17.8	0.37	6.53	434	462	24.9	3.0
4H-3, 145–150	28.69	33.0	7.62	10.71	562	43.9	5.3	8.2	10.3	1.21	6.07	282	462	32.1	3.6
4H-5, 145–150	31.69	33.0	7.55	11.26	563	43.3	5.0	8.0	9.7	0.00	7.52	307	462	27.6	2.7
155-931B-															
2H-5, 140–150	8.20	33.0	7.61	23.75	560	48.4	5.9	10.0	40.9	0.00	3.25	375	462	58.9	6.4
3H-5, 140–150	17.70	32.5	7.53	13.59	559	44.7	5.9	8.8	12.7	0.02	5.66	386	457	62.0	2.3
4H-5, 140–150	27.20	34.0	7.66	12.55	559	41.3	5.6	9.0	9.7	0.05	7.03	351	462	20.6	3.1
5H-5, 70–80	36.00	33.0	7.66	12.23	559	42.9	5.6	9.4	21.7	0.01	7.73	399	457	120.9	2.9
8H-5, 140–150	65.20	32.5	7.66	12.91	557	43.0	6.1	9.3	12.6	0.00	8.93	433	454	51.9	3.1
11X-3, 140–150	88.70	32.2	7.56	11.30	549	40.1	5.0	8.6	37.5	1.26	7.86	455	456	141.6	2.9
14X-3, 140–150	117.96	32.5	7.51	14.79	558	46.5	6.3	7.6	35.4	1.98	8.83	476	455	97.8	2.9
19X-2, 140–150	164.40	32.0	7.46	11.05	552	39.7	4.8	7.7	14.1	1.47	7.13	456	462	86.7	2.6
23X-1, 142–150	201.22	32.5	7.61	11.85	537	40.4	5.2	8.9	11.9	2.03	6.43	370	446	29.2	2.7
26X-2, 140–150	231.60	32.0	7.71	13.31	542	35.6	4.2	8.4	11.9	0.31	7.60	363	460	18.7	2.4
29X-3, 140–150	262.10	32.2	7.58	11.20	549	34.4	4.1	8.1	9.8	1.62	8.93	300	469	20.3	3.3
32X-3, 140–150	291.00	32.0	7.72	11.04	550	38.1	5.6	7.2	7.5	1.74	7.06	480	463	127.3	4.1
35X-2, 140–150	318.40	32.0	7.83	18.66	546	35.3	4.9	7.2	9.5	1.30	4.09	314	476	10.7	2.3
38X-2, 135–150	347.25	32.0	7.78	12.65	547	32.1	4.5	8.7	12.2	0.91	4.69	286	475	8.0	2.3
41X-4, 140–150	379.30	33.0	7.49	15.08	558	36.0	6.1	7.2	7.6	1.63	7.56	421	477	39.6	2.7
44X-6, 106–121	408.80	33.0	7.60	25.21	553	36.4	6.8	6.5	7.7	0.41	9.03	246	477	11.5	2.2

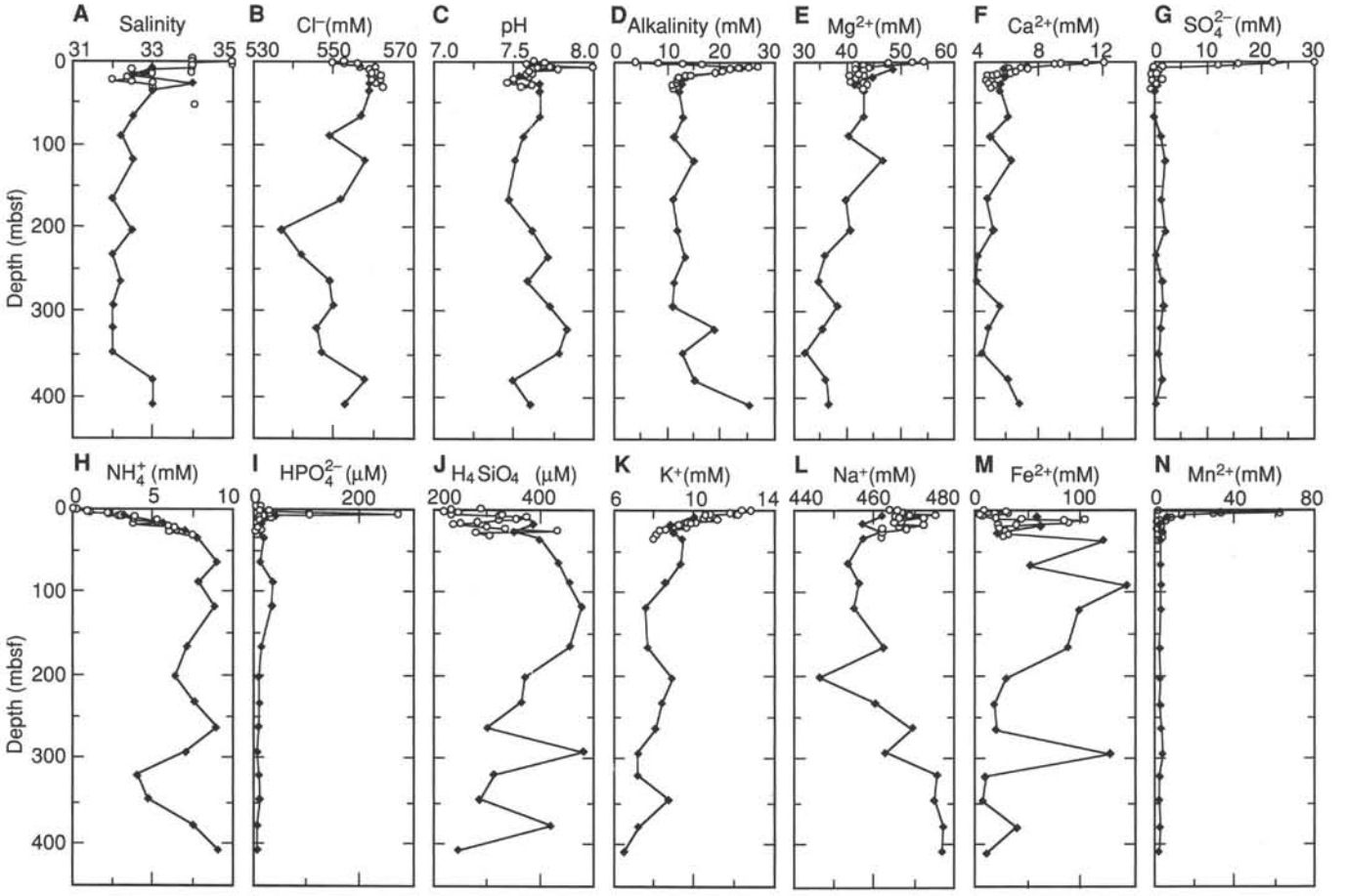

Figure 20. Downhole variation in pore-water chemistry: **A.** Salinity. **B.** Chloride. **C.** pH. **D.** Alkalinity. **E.** Magnesium. **F.** Calcium. **G.** Sulfate. **H.** Ammonium. **I.** Phosphate. **J.** Silica. **K.** Potassium. **L.** Sodium. **M.** Iron. **N.** Manganese. Open circles = samples from Hole 931C; solid diamonds = samples from Hole 931B.

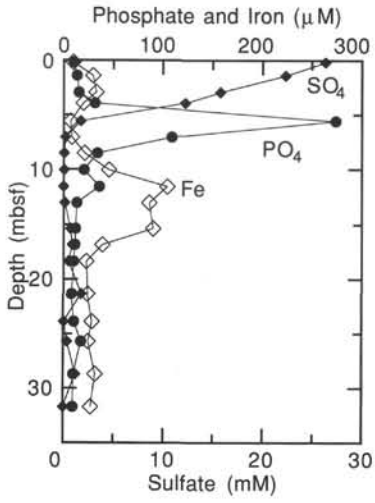

Figure 21. Pore-water concentrations of sulfate, phosphate, and iron from 0 to 32 mbsf.

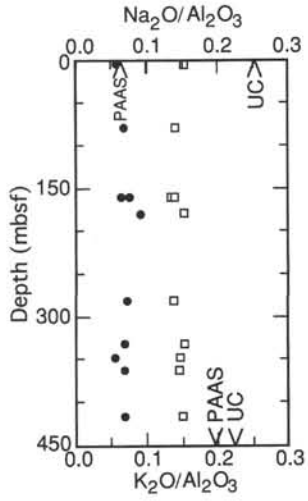

Figure 22. Depth profile of K_2O/Al_2O_3 (open squares) and Na_2O/Al_2O_3 (solid circles) for mud samples. Post-Archean average shale (PAAS; $K_2O/Al_2O_3 = 0.196$, $Na_2O/Al_2O_3 = 0.063$) and average upper crust (UC; $K_2O/Al_2O_3 = 0.224$, $Na_2O/Al_2O_3 = 0.257$) are plotted for reference (from Taylor and McLennan, 1985).

with seawater. The array-sonic tool (SDT) was replaced by the long-spaced sonic (LSS) tool, and the NGT by a spare.

We lowered the Quad combination again, and encountered a bridge below a drill-pipe measurement (DPM) of 3738.3 mbrf (251.6 mbsf). After several unsuccessful attempts to pass the tool string through this bridge, we were able to log the upper 250 mbsf of the hole. In Table 16, we summarize the intervals logged with each tool string. Two runs were done with the Quad-combination/TLT string and data was recorded moving both up and down the hole. For the first run, the base of the BHA was set at 93 mbsf. During the repeat run, the BHA was set at 71 mbsf. The upgoing logs are of good overall quality, except over a few intervals, where the caliper measurements indicate borehole washouts (>16 in.) (Fig. 28).

The FMS tool string provided high-resolution resistivity images of the borehole wall, as well as measurements of the three vector components of the local magnetic field, borehole inclination, deviation, and diameter in two orthogonal directions. Within a few small, washed-out intervals, where the borehole diameter exceeded 15 in. (38 cm), only two of the FMS pads maintained contact with the borehole wall.

The GLT provided two uphole recordings (Table 16). The resulting logs are of good quality in the open-hole section (Fig. 29) and reveal distinct lithologic variations.

Table 10. Major element composition (wt%) of sediment samples, Site 931.

Core, section, interval (cm)	Depth (mbsf)	Lithology	SiO_2	TiO_2	Al_2O_3	Fe_2O_3	MnO	MgO	CaO	Na_2O	K_2O	P_2O_5	Total	LOI
155-931A-														
1H-4, 50–55	5.00	Mud	60.22	1.09	21.88	8.05	0.09	2.25	1.33	1.26	3.28	0.19	99.62	7.42
155-931B-														
10X-3, 12–17	79.92	Mud	62.09	1.19	20.89	7.98	0.12	2.12	0.87	1.40	2.89	0.16	99.71	12.76
19X-1, 41–46	161.91	Mud	60.03	1.09	22.64	8.61	0.12	2.16	0.80	1.44	3.02	0.20	100.11	8.88
19X-1, 61–66	162.11	Mud	63.37	1.02	20.73	7.62	0.11	2.08	0.87	1.53	2.85	0.20	100.37	7.84
21X-1, 25–30	180.95	Mud	66.33	1.02	17.83	6.79	0.10	1.81	0.96	1.59	2.69	0.17	99.29	6.15
31X-5, 23–27	283.13	Mud	61.74	1.14	21.15	8.03	0.10	2.12	0.94	1.50	2.92	0.18	99.80	7.90
36X-5, 142–147	332.52	Mud	61.96	1.03	20.49	7.43	0.09	2.02	2.76	1.36	3.11	0.14	100.37	8.10
38X-4, 70–71	349.60	Mud	57.65	0.99	22.50	8.47	0.08	2.09	3.35	1.19	3.26	0.14	99.69	9.11
40X-2, 13–16	364.59	Mud	62.04	1.14	22.11	8.38	0.10	2.29	0.85	1.47	3.18	0.16	101.71	7.74
45X-4, 126	417.36	Mud	60.87	1.15	22.26	8.51	0.11	2.21	0.79	1.48	3.27	0.17	100.80	7.79

Notes: Total iron is reported as Fe_2O. LOI = loss on ignition.

Table 11. Trace element composition (ppm) of sediment samples, Site 931.

Core, section, interval (cm)	Depth (mbsf)	Lithology	Ba	Ce	Cr	Cu	Nb	Ni	Rb	Sr	V	Y	Zn	Zr
155-931A-														
1H-4, 50–55	5.00	Mud	505	104	65	35	20	35	141	155	85	34	126	186
155-931B-														
10X-3, 12–17	79.92	Mud	487	110	64	30	23	33	126	150	76	39	125	238
19X-1, 41–46	161.91	Mud	472	113	69	35	23	34	131	148	91	37	131	216
19X-1, 61–66	162.11	Mud	493	101	62	31	22	35	123	157	84	36	125	229
21X-1, 25–30	180.95	Mud	471	86	55	25	22	29	114	167	77	40	108	317
31X-5, 23–27	283.13	Mud	486	105	65	29	22	32	123	147	78	37	124	221
36X-5, 142–147	332.52	Mud	499	95	64	30	21	34	131	205	97	35	121	224
38X-4, 70–71	349.60	Mud	467	115	74	47	21	42	136	218	113	32	129	171
40X-2, 13–16	364.59	Mud	513	116	70	32	23	34	133	148	87	37	127	220
45X-4, 126	417.36	Mud	531	108	69	34	23	34	137	144	87	38	126	210

Table 12. Index properties at Site 931.

Core, section, interval (cm)	Depth (mbsf)	Water content (%)	Wet-bulk density (g/cm^3)	Grain density (g/cm^3)	Dry-bulk density (g/cm^3)	Porosity (%)	Void ratio
155-931A-							
1H-1, 12–14	0.12	51.2	1.51	2.74	0.74	73.7	2.80
1H-3, 52–54	3.52	46.1	1.60	2.95	0.86	71.1	2.46
155-931B-							
2H-1, 84–86	1.64	45.0	1.63	2.84	0.89	69.4	2.27
2H-2, 76–78	3.06	45.2	1.60	2.84	0.88	69.5	2.28
2H-3, 88–90	4.68	43.4	1.64	2.78	0.93	67.5	2.08
2H-5, 42–44	7.22	43.5	1.66	2.80	0.94	67.8	2.11
2H-6, 12–14	8.42	42.3	1.65	2.81	0.95	66.9	2.02
2H-7, 27–29	10.07	41.8	1.67	2.79	0.97	66.2	1.95
3H-1, 129–131	11.59	43.2	1.63	2.77	0.93	67.3	2.06
3H-2, 94–96	12.74	40.3	1.66	2.71	0.99	64.1	1.79
3H-3, 77–79	14.07	40.0	1.71	2.81	1.03	64.7	1.83
3H-4, 110–112	15.90	38.2	1.75	2.80	1.08	62.9	1.69
3H-5, 22–24	16.52	39.5	1.70	2.79	1.03	64.0	1.78
3H-6, 112–114	18.92	36.6	1.75	2.78	1.11	61.0	1.56
3H-7, 75–77	20.05	39.2	1.71	2.78	1.04	63.6	1.75
4H-1, 36–38	20.16	37.9	1.74	2.80	1.08	62.5	1.67
4H-2, 33–35	21.63	37.3	1.75	2.80	1.10	61.9	1.63
4H-3, 57–59	23.37	38.1	1.71	2.78	1.06	62.6	1.68
4H-4, 14–16	24.44	37.4	1.74	2.75	1.09	61.6	1.60
4H-5, 39–41	26.19	35.6	1.77	2.70	1.14	59.3	1.46
4H-6, 36–38	27.66	33.8	1.83	2.80	1.22	58.2	1.39
4H-6, 40–42	27.70			2.83			
4H-7, 35–37	29.15	34.8	1.78	2.74	1.16	58.8	1.43
4H-7, 44–46	29.24			2.79			
5H-1, 32–34	29.62	36.0	1.75	2.73	1.12	60.0	1.50
5H-1, 41–43	29.71			2.88			
5H-2, 32–34	31.12	33.1	1.83	2.79	1.22	57.5	1.35
5H-3, 32–34	32.62	33.5	1.83	2.83	1.22	58.1	1.39
5H-4, 35–37	34.15	35.0	1.81	2.80	1.18	59.5	1.47
5H-5, 31–33	35.61	33.7	1.80	2.74	1.20	57.6	1.36
5H-6, 37–39	36.47	32.8	1.79	2.72	1.21	56.5	1.30
5H-6, 80–82	36.90			2.84			
5H-7, 27–29	37.87	33.8	1.82	2.72	1.21	57.6	1.36
6H-1, 28–30	39.08	32.3	1.78	2.73	1.21	56.0	1.27
6H-2, 15–17	40.45	33.5	1.83	2.77	1.22	57.6	1.36
6H-3, 50–52	42.30	32.3	1.87	2.81	1.26	56.6	1.31
6H-4, 28–30	43.58	32.3	1.85	2.80	1.25	56.7	1.31
6H-5, 33–35	45.13	32.6	1.83	2.72	1.24	56.2	1.28
6H-6, 6–8	46.36			2.74			
6H-6, 35–37	46.65	31.6	1.86	2.69	1.27	54.8	1.21
6H-7, 63–65	48.43	32.5	1.83	2.72	1.23	56.1	1.28
7H-2, 13–15	49.93	31.7	1.85	2.81	1.27	56.0	1.27
7H-3, 101–103	52.31	31.9	1.82	2.70	1.24	55.3	1.24
7H-4, 36–38	53.16	30.7	1.90	2.75	1.31	54.3	1.19
7H-5, 25–27	54.55	30.4	1.92	2.77	1.34	54.1	1.18
8H-1, 29–31	58.09	30.2	1.89	2.78	1.32	54.0	1.17
8H-2, 44–46	59.74	31.3	1.86	2.83	1.28	55.7	1.26
8H-3, 29–31	61.09	30.0	1.89	2.78	1.33	53.7	1.16
8H-3, 143–145	62.23			2.78			
8H-4, 37–39	62.67	30.4	1.87	2.80	1.30	54.5	1.20
8H-5, 121–123	65.01	29.5	1.89	2.73	1.33	52.7	1.11
8H-6, 123–125	66.53	27.1	1.95	2.77	1.43	50.1	1.01
8H-7, 80–82	67.60	29.7	1.89	2.78	1.33	53.4	1.15
9H-1, 36–38	67.66	30.4	1.89	2.80	1.32	54.5	1.20
9H-2, 30–32	69.10	30.3	1.87	2.75	1.30	53.9	1.17
9H-3, 36–38	70.66	29.8	1.90	2.81	1.33	53.9	1.17
9H-4, 36–38	72.16	30.6	1.87	2.74	1.30	54.1	1.18
9H-4, 125–127	73.05			2.78			
9H-5, 134–136	74.64	29.9	1.89	2.77	1.33	53.6	1.15
9H-6, 37–39	75.17	29.1	1.91	2.80	1.35	52.9	1.12
9H-7, 76–78	77.06	28.9	1.92	2.80	1.37	52.7	1.11
10X-1, 112–114	77.92	30.1	1.87	2.69	1.31	53.2	1.13
10X-2, 116–118	79.46	31.3	1.86	2.68	1.28	54.4	1.19
10X-3, 23–25	80.03	31.6	1.85	2.72	1.26	55.1	1.23
10X-4, 88–90	82.18	32.0	1.85	2.71	1.26	55.5	1.25
10X-5, 110–112	83.35	31.6	1.87	2.75	1.28	55.4	1.24
11X-1, 74–76	85.04	30.7	1.86	2.76	1.29	54.4	1.19
11X-2, 75–77	86.55	31.4	1.85	2.70	1.27	54.6	1.20
11X-3, 76–78	88.06	31.5	1.86	2.70	1.27	54.8	1.21
11X-4, 75–77	89.55	30.6	1.87	2.70	1.30	53.7	1.16
11X-5, 77–79	91.07	29.9	1.89	2.67	1.32	52.6	1.11
12X-1, 79–81	94.69	31.1	1.85	2.70	1.27	54.3	1.19
12X-2, 78–80	96.18	31.6	1.83	2.71	1.25	55.0	1.22
12X-3, 79–81	97.69	29.9	1.86	2.67	1.30	52.7	1.11
12X-4, 39–41	98.79	28.8	1.92	2.73	1.36	51.9	1.08
12X-5, 15–17	100.05	28.1	1.92	2.69	1.38	50.7	1.03
13X-1, 78–80	104.28	26.8	1.92	2.69	1.40	49.0	0.96
13X-2, 96–98	105.96	30.1	1.88	2.70	1.31	53.1	1.13
13X-3, 78–80	107.28	29.8	1.89	2.70	1.32	52.8	1.12
13X-4, 34–36	108.34	29.2	1.89	2.72	1.34	52.3	1.10
14X-1, 114–116	114.34	28.3	1.91	2.69	1.37	50.9	1.04
14X-3, 50–52	116.56	28.0	1.90	2.70	1.37	50.6	1.02
15X-1, 96–98	123.76	29.1	1.90	2.71	1.34	52.1	1.09
15X-3, 90–92	126.70			2.71			
16X-1, 74–76	133.24			2.75			

Table 12 (continued).

Core, section, interval (cm)	Depth (mbsf)	Water content (%)	Wet-bulk density (g/cm^3)	Grain density (g/cm^3)	Dry-bulk density (g/cm^3)	Porosity (%)	Void ratio
16X-3, 78–80	136.28	26.8	1.95	2.72	1.43	49.3	0.97
19X-1, 82–84	162.32	30.3	1.93	2.75	1.34	53.9	1.17
19X-2, 77–79	163.77	28.6	1.92	2.72	1.37	51.6	1.07
19X-3, 80–82	165.30	29.6	1.89	2.72	1.33	52.8	1.12
19X-4, 95–97	166.95	28.7	1.91	2.71	1.36	51.6	1.07
21X-1, 89–91	181.59	28.9	1.90	2.73	1.35	52.0	1.08
21X-2, 89–91	183.09	25.3	2.01	2.79	1.50	48.0	0.92
23X-1, 1–3	199.81			2.74			
23X-2, 23–25	201.53			2.74			
25X-1, 90–92	220.00	27.2	1.91	2.72	1.39	49.8	0.99
25X-2, 86–88	221.46	27.9	1.92	2.77	1.39	51.2	1.05
25X-3, 76–78	222.86	26.3	1.98	2.79	1.46	49.3	0.97
25X-4, 33–35	223.93	25.2	2.01	2.79	1.50	47.9	0.92
26X-1, 59–61	229.29	21.0	2.09	2.77	1.65	41.7	0.72
26X-2, 35–37	230.55	18.9	2.15	2.74	1.74	38.5	0.63
26X-3, 3–5	231.73	23.6	2.02	2.75	1.55	45.3	0.83
27X-1, 77–79	239.17	18.9	2.14	2.76	1.73	38.5	0.63
27X-2, 69–71	240.59	21.9	2.10	2.76	1.64	43.1	0.76
27X-3, 73–75	242.13	18.6	2.16	2.76	1.76	38.1	0.62
27X-4, 73–75	243.63	21.8	2.09	2.72	1.63	42.5	0.74
27X-5, 108–110	245.48	21.6	2.10	2.74	1.65	42.4	0.74
27X-6, 75–77	246.65	19.8	2.15	2.70	1.72	39.5	0.65
27X-7, 36–38	247.76	19.6	2.17	2.81	1.75	40.1	0.67
28X-1, 66–68	248.66	21.6	2.12	2.77	1.66	42.7	0.75
28X-2, 14–16	249.51	21.1	2.07	2.72	1.63	41.5	0.71
28X-3, 74–76	250.71	18.7	2.12	2.70	1.73	37.8	0.61
28X-4, 74–76	252.21	17.8	2.18	2.75	1.79	36.7	0.58
28X-5, 71–73	253.68	19.3	2.10	2.75	1.69	39.2	0.64
29X-1, 74–76	258.44	20.9	2.08	2.71	1.64	41.1	0.70
29X-2, 74–76	259.94	19.0	2.12	2.72	1.72	38.4	0.62
29X-3, 74–76	261.44	17.9	2.15	2.72	1.77	36.6	0.58
29X-4, 85–87	263.05	21.4	2.06	2.72	1.62	41.9	0.72
29X-5, 12–14	263.82	16.0	2.20	2.73	1.85	33.6	0.51
31X-1, 74–76	277.64	21.6	2.07	2.72	1.62	42.2	0.73
31X-2, 72–74	279.12	20.8	2.08	2.73	1.64	41.3	0.70
31X-3, 64–66	280.54	21.5	2.10	2.77	1.65	42.5	0.74
31X-4, 73–75	282.13	21.3	2.12	2.78	1.67	42.4	0.74
31X-5, 91–93	283.81	22.5	2.08	2.75	1.61	43.8	0.78
31X-6, 25–27	284.65	23.3	2.04	2.77	1.57	45.2	0.82
32X-1, 62–64	287.22	21.7	2.09	2.80	1.64	43.1	0.76
32X-2, 66–68	288.76	22.1	2.10	2.78	1.63	43.5	0.77
32X-3, 58–60	290.18	21.7	2.11	2.78	1.65	43.0	0.75
32X-4, 73–75	291.83	21.0	2.08	2.76	1.64	41.7	0.71
32X-5, 58–60	293.18	20.6	2.09	2.71	1.66	40.7	0.69
32X-6, 59–61	294.69	21.0	2.08	2.71	1.64	41.3	0.70
33X-1, 79–81	296.99	20.9	2.08	2.72	1.65	41.3	0.70
33X-2, 91–93	298.61	21.1	2.10	2.72	1.65	41.5	0.71
33X-3, 91–93	300.11	20.4	2.10	2.73	1.67	40.7	0.69
33X-4, 82–84	301.52	19.7	2.14	2.74	1.72	39.7	0.66
34X-1, 74–76	306.54	20.9	2.08	2.74	1.64	41.3	0.70
34X-2, 113–115	308.43	19.8	2.13	2.79	1.71	40.1	0.67
34X-3, 116–118	309.96	20.6	2.11	2.72	1.67	40.8	0.69
34X-4, 54–56	310.84	21.4	2.09	2.72	1.64	42.0	0.72
35X-1, 51–53	316.01	23.5	2.03	2.73	1.55	45.0	0.82
35X-2, 66–68	317.66	18.6	2.17	2.71	1.77	37.7	0.60
35X-3, 78–80	319.28	18.9	2.15	2.71	1.75	38.1	0.62
36X-1, 99–101	326.09	22.4	2.05	2.73	1.59	43.5	0.77
36X-2, 88–90	327.48	21.9	2.06	2.70	1.61	42.6	0.74
36X-3, 94–96	329.04	21.8	2.08	2.73	1.63	42.6	0.74
36X-4, 77–79	330.37	21.8	2.07	2.72	1.61	42.5	0.74
36X-5, 67–69	331.77	21.7	2.05	2.73	1.60	42.6	0.74
36X-6, 56–58	333.16	21.5	2.04	2.73	1.60	42.2	0.73
37X-1, 52–54	335.32	21.6	2.06	2.73	1.62	42.4	0.74
37X-2, 59–61	336.89	20.8	2.10	2.75	1.66	41.4	0.71
37X-3, 55–57	338.35	21.2	2.08	2.73	1.64	41.7	0.72
37X-4, 61–63	339.91	19.7	2.13	2.74	1.71	39.7	0.66
38X-1, 80–82	345.20	22.7	2.07	2.80	1.60	44.5	0.80
38X-2, 59–61	346.49	17.1	2.23	2.78	1.85	35.8	0.56
38X-3, 60–62	348.00			2.73			
38X-4, 57–59	349.47			2.74			
38X-5, 81–83	350.75			2.73			
39X-1, 79–81	354.89	29.1	1.90	2.79	1.35	52.7	1.12
39X-2, 76–78	356.36	26.3	1.97	2.80	1.46	49.3	0.97
39X-3, 79–81	357.89	26.3	1.97	2.78	1.45	49.2	0.97
39X-4, 79–81	359.39	25.5	1.97	2.73	1.46	47.7	0.91
39X-5, 74–76	360.84	24.5	2.02	2.79	1.53	46.9	0.88
40X-1, 24–26	363.94	23.6	2.01	2.74	1.54	45.2	0.82
40X-2, 73–75	365.19	23.0	2.05	2.82	1.58	45.1	0.82
40X-3, 73–75	366.69	22.8	2.09	2.81	1.61	44.7	0.81
40X-4, 75–77	368.21	22.8	2.05	2.79	1.58	44.6	0.80
40X-5, 75–77	369.71	22.6	2.07	2.79	1.60	44.3	0.80
40X-6, 56–58	371.02	23.6	2.04	2.78	1.56	45.6	0.84
40X-7, 56–58	371.77	23.0	2.05	3.26	1.58	48.8	0.95
41X-1, 74–76	374.14	26.0	1.98	2.79	1.46	48.8	0.95
41X-2, 74–76	375.64	24.5	1.99	2.72	1.51	46.3	0.86
41X-3, 73–75	377.13	24.8	2.01	2.79	1.51	47.3	0.90
41X-4, 73–75	378.63	24.8	2.02	2.78	1.52	47.2	0.89
41X-5, 74–76	380.14	23.1	2.05	2.77	1.58	44.9	0.81

Table 12 (continued).

Core, section, interval (cm)	Depth (mbsf)	Water content (%)	Wet-bulk density (g/cm^3)	Grain density (g/cm^3)	Dry-bulk density (g/cm^3)	Porosity (%)	Void ratio
41X-6, 71–73	381.61	24.3	2.02	2.79	1.53	46.6	0.87
42X-1, 74–76	383.64	25.4	1.99	2.83	1.49	48.4	0.94
42X-2, 74–76	385.14	25.6	1.99	2.80	1.48	48.5	0.94
42X-3, 74–76	386.64	24.3	2.01	2.76	1.52	46.4	0.87
42X-4, 74–76	388.14	24.3	2.02	2.80	1.53	46.7	0.88
42X-5, 74–76	389.64	24.3	2.01	2.72	1.52	45.9	0.85
42X-6, 75–77	391.15	24.7	2.00	2.78	1.51	47.1	0.89
43X-1, 44–46	392.84	24.4	2.01	2.77	1.52	46.5	0.87
43X-2, 74–76	394.21	24.4	2.03	2.80	1.54	46.9	0.88
43X-3, 75–77	395.72	25.5	2.00	2.79	1.49	48.2	0.93
43X-4, 106–108	397.53	23.9	2.04	2.78	1.55	46.0	0.85
43X-5, 76–78	398.73	23.8	2.02	2.73	1.54	45.3	0.83
43X-6, 78–80	400.25	23.4	2.04	2.79	1.57	45.5	0.83
43X-7, 78–80	401.75	22.5	2.09	2.80	1.62	44.2	0.79
44X-2, 14–16	402.51	22.6	2.08	2.79	1.61	44.3	0.79
44X-3, 70–72	404.51	22.8	2.07	2.82	1.60	44.9	0.82
44X-4, 48–50	405.79	22.7	2.05	2.74	1.58	44.0	0.79
44X-5, 47–49	406.85		2.11				
44X-6, 48–50	408.22	22.6	2.05	2.77	1.59	44.2	0.79
44X-7, 47–49	409.42	23.0	2.04	2.75	1.57	44.5	0.80
45X-1, 50–52	412.10	22.7	2.06	2.81	1.59	44.6	0.80
45X-2, 53–55	413.63	22.1	2.08	2.79	1.62	43.7	0.77
45X-3, 52–54	415.12	22.6	2.06	2.77	1.60	44.1	0.79
45X-4, 52–54	416.62	22.1	2.38	2.79	1.85	43.7	0.78

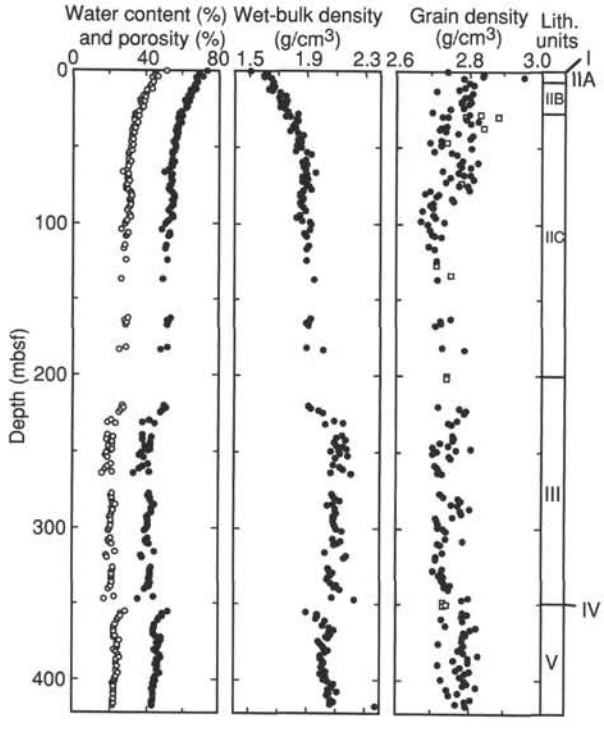

Figure 23. Water content (open circles), porosity (solid circles), wet-bulk density, and grain density in Holes 931A and 931B. Muddy sand units, sampled only for grain density, are represented by squares in the grain density profile.

Two runs of the GHMT-A provided high-quality upgoing logs of total magnetic field intensity and magnetic susceptibility (Table 16). Prior to logging, we anticipated possible problems with this tool because its outer diameter (OD) is 3.78 in. (9.6 cm), wider than the standard size of other logging tools that have a maximum OD of 3.6 in. (9.15 cm). The GHMT-A is closer to the same OD as the "go-devil" at 3.8 in. (9.65 cm), which is used to operate the lockable flapper valve (LFV) used in the APC-XCB BHA. We did not experience any problems reentering the drill pipe after logging. Because of the high sensitivity of the GHMT-A sensors to magnetic fields, this tool ideally should be used in the first logging run to avoid possible magnetic induction effects caused by the other logging tools. However, in the present configuration we are forced to recommend that this tool string be run last; otherwise, a go-devil must be pumped downhole after the GHMT-A run to ensure that the LFV is open prior to the next logging run. We suggest that, in the future, this tool be redesigned to conform with current ODP logging specifications regarding tool OD.

The borehole varied in diameter significantly, from approximately 11 in. (28 cm; minimum opening of the density tool caliper) to a maximum of 18 in. (46 cm). Borehole diameter gradually increased from 73 to 140 mbsf and then gradually decreased from 140 to 180 mbsf, with a few 0.5- to 3-m intervals that were washed out between 180 and 235 mbsf. Shore-based processed logs are shown in analog format at the end of this chapter. Digital files are available in the CD-ROM (back pocket).

Results

Logging results are useful for delineating lithostratigraphic boundaries at this site (Fig. 28). The lithostratigraphy between approximately 140 and 220 mbsf is not well known because of poor core recovery. The caliper log, useful here for determining the relative competency of the sediment, provided a qualitative index for differentiating between finer grained, relatively cohesive muds and coarser grained unconsolidated sand intervals. The Quad-combination and geochemical logging data correlate well with the magnetic susceptibility log recorded by the GHMT-A tool. We subdivided the logged section into four logging stratigraphic units (logging units), based on distinct trends in physical and chemical properties downhole.

Logging Unit 1 (71.3–157 mbsf) is characterized by an overall upward increase in gamma-ray counts, porosity, concentrations of Al and K, Fe yields, and by an upward decrease in velocity, density, magnetic susceptibility, and Si yields. The relatively high U content, indicated by the difference between computed gamma-ray (CGR) and spectral gamma-ray (SGR) values, suggests that this unit is clay-rich and may be enriched in organic matter. Logging Unit 1 is divided into two subunits. Above 113 mbsf, it is characterized by relatively high gamma-ray counts, high resistivity, downward-increasing values in velocity and density, and decreasing porosity. Al concentration

Table 13. Strength measurements at Site 931.

Core, section, interval (cm)	Depth (mbsf)	Unconfined compressive strength* (kPa)	Undrained shear strength (kPa)
155-931A-			
1H-1, 12	0.12		7.6
1H-3, 50	3.50		7.4
155-931B-			
2H-1, 84	1.64		7.4
2H-2, 77	3.07		6.5
2H-3, 90	4.70		6.8
2H-5, 43	7.23		7.4
2H-6, 13	8.43		5.7
2H-7, 27	10.07		6.8
3H-1, 130	11.60		11.0
3H-2, 95	12.75		9.6
3H-3, 78	14.08		9.6
3H-4, 111	15.91		9.3
3H-5, 23	16.53		9.6
3H-6, 113	18.93		9.3
3H-7, 76	20.06		9.1
4H-1, 37	20.17		12.7
4H-2, 32	21.61		11.9
4H-3, 58	23.38		11.3
4H-4, 15	24.45		12.4
4H-5, 40	26.20		11.0
4H-6, 37	27.67		15.8
4H-7, 36	29.16		13.0
5H-1, 33	29.63		16.7
5H-2, 33	31.13		15.6
5H-3, 33	32.63		16.1
5H-4, 36	34.16		15.0
5H-5, 32	35.62		19.5
5H-6, 38	36.48		27.2
5H-7, 28	37.88		23.8
6H-1, 29	39.09		18.4
6H-2, 16	40.46		26.0
6H-3, 51	42.31		21.8
6H-4, 29	43.59		22.9
6H-5, 34	45.14		30.0
6H-6, 36	46.66		28.3
6H-7, 64	48.44		19.0
7H-2, 14	49.94		30.6
7H-3, 102	52.32		25.7
7H-4, 37	53.17		24.0
7H-5, 26	54.56		21.5
7H-6, 12	55.92		33.9
8H-1, 30	58.10		28.8
8H-2, 45	59.75		36.0
8H-3, 30	61.10		38.6
8H-4, 38	62.68		32.9
8H-5, 122	65.02		26.7
8H-6, 124	66.54		28.8
8H-7, 81	67.61		21.6
9H-1, 37	67.67		37.0
9H-2, 31	69.11		41.1
9H-3, 37	70.67		23.7
9H-4, 37	72.17		19.0
9H-5, 135	74.65		27.3
9H-6, 38	75.18		38.1
9H-7, 77	77.07		36.5
10X-1, 112	77.92		26.7
10X-2, 116	79.46		24.2
10X-3, 23	80.03		31.4
10X-4, 88	82.18		20.1
10X-5, 110	83.35		28.3
11X-1, 74	85.04		21.6
11X-2, 75	86.55		29.8
11X-3, 76	88.06		47.3
11X-4, 75	89.55		37.5
11X-5, 77	91.07		48.3
12X-1, 79	94.69		18.5
12X-2, 79	96.18		21.1
12X-3, 80	97.70		31.9
12X-4, 39	98.79		51.9
12X-5, 16	100.06		54.0
13X-2, 96	105.96		22.1
13X-3, 78	107.28		60.7
13X-4, 34	108.34		45.3
14X-1, 115	114.35		30.3
16X-3, 78	136.28		51.9
19X-1, 94	162.44	98.0	
19X-2, 77	163.77	122.6	
19X-3, 80	165.30	171.6	
19X-4, 97	166.97	176.4	
21X-1, 90	181.60	49.0	25.2
21X-2, 90	183.10	98.0	92.1
25X-1, 91	220.01	122.6	51.4
25X-2, 87	221.47	107.8	66.3
25X-3, 77	222.87	215.6	82.3
25X-4, 34	223.94	186.2	82.3
26X-1, 60	229.30	121.6	88.3
26X-2, 36	230.56	152.0	93.7
26X-3, 4	231.74	161.8	94.6
27X-1, 78	239.18	201.0	105.2
27X-2, 70	240.60	348.0	135.3
27X-3, 34	241.74	383.2	229.8
27X-4, 74	243.64	352.8	183.0
27X-5, 109	245.49	352.8	147.6
27X-6, 76	246.65	411.6	202.4
27X-7, 37	247.77	441.0	272.3
28X-1, 67	248.67	176.4	74.3
28X-2, 15	249.52	279.4	145.9
28X-3, 75	250.72	215.6	104.3
28X-4, 75	252.22	299.0	137.0
28X-5, 75	253.72	367.6	
29X-1, 75	258.45	240.2	103.4
29X-2, 75	259.95	318.6	145.9
29X-3, 75	261.45	318.6	132.6
29X-4, 86	263.06	294.0	115.8
29X-5, 13	263.83	406.8	184.8
31X-1, 75	277.65	245.0	78.7
31X-2, 73	279.13	308.8	79.6
31X-3, 65	280.55	279.4	92.8
31X-4, 74	282.14	205.8	93.7
31X-5, 92	283.82	220.6	67.2
31X-6, 26	284.66	132.4	78.7
32X-1, 62	287.22	166.6	63.6
32X-2, 68	288.78	294.0	
32X-3, 60	290.20	284.2	
32X-4, 77	291.87	341.0	
32X-5, 60	293.20	392.0	
32X-6, 60	294.70	343.0	
33X-1, 79	296.99	343.0	320.0
33X-2, 90	298.60	392.0	
33X-3, 91	300.11	441.0	
33X-4, 79	301.49	382.2	
34X-1, 75	306.55	274.4	
34X-2, 113	308.43	441.0	
34X-3, 116	309.96	441.0	
34X-4, 55	310.85	416.6	
35X-1, 50	316.00	333.2	
35X-2, 66	317.66	421.4	
35X-3, 77	319.27	431.2	
36X-1, 102	326.12	323.4	
36X-2, 87	327.47	372.4	
36X-3, 94	329.04	362.6	
36X-4, 78	330.38	431.2	
36X-5, 68	331.78	441.0	
36X-6, 56	333.16	431.2	
37X-1, 53	335.33	401.8	
37X-2, 59	336.89	431.2	
37X-3, 55	338.35	416.6	
37X-4, 62	339.92	441.0	
38X-1, 80	345.20	441.0	
38X-2, 60	346.50	441.0	
38X-3, 61	348.01	441.0	
38X-4, 57	349.47	431.2	
38X-5, 81	350.75	274.4	
38X-7, 78	352.57	367.6	
39X-1, 80	354.90	132.4	51.3
39X-2, 77	356.37	220.6	79.6
39X-3, 80	357.90	245.0	96.4
39X-4, 80	359.40	299.0	143.2
39X-5, 75	360.85	333.2	141.4
40X-1, 25	363.95	357.8	134.4
40X-2, 74	365.20	392.0	131.7
40X-3, 74	366.70	387.2	276.7
40X-4, 76	368.22	441.0	
40X-5, 75	369.71	441.0	
40X-6, 57	371.03	441.0	
40X-7, 57	371.78	441.0	
41X-1, 75	374.15	181.4	69.8
41X-2, 75	375.65	372.4	156.5
41X-3, 74	377.14	308.8	105.2
41X-4, 74	378.64	235.2	131.7
41X-5, 75	380.15	294.0	129.1
41X-6, 72	381.62	357.8	344.8
42X-1, 75	383.65	137.2	60.1
42X-2, 75	385.15	240.2	77.8
42X-3, 75	386.65	250.0	108.7
42X-4, 75	388.15	318.6	133.5
42X-5, 75	389.65	372.4	152.9
42X-6, 76	391.16	328.4	130.0
43X-1, 45	392.85	338.2	93.7
43X-2, 75	394.22	318.6	135.3
43X-3, 70	395.67	259.8	136.1
43X-4, 108	397.55	328.4	107.9
43X-5, 77	398.74	362.6	142.3
43X-6, 79	400.26	397.0	160.9
43X-7, 79	401.76	441.0	
44X-2, 15	402.52	441.0	

Table 13 (continued).

Core, section, interval (cm)	Depth (mbsf)	Unconfined compressive strength* (kPa)	Undrained shear strength (kPa)
44X-3, 70	404.51	441.0	
44X-4, 49	405.80	441.0	
44X-5, 47	406.85	441.0	
44X-6, 49	408.23	441.0	
44X-7, 47	409.42	441.0	
45X-1, 50	412.10	313.6	
45X-2, 54	413.64	318.6	
45X-3, 54	415.14	441.0	
45X-4, 54	416.64	441.0	

Note: *Unconfined compressive strength (q_u) can be used to approximate undrained shear strength (S_u) by the relationship $q_u = 2S_u$.

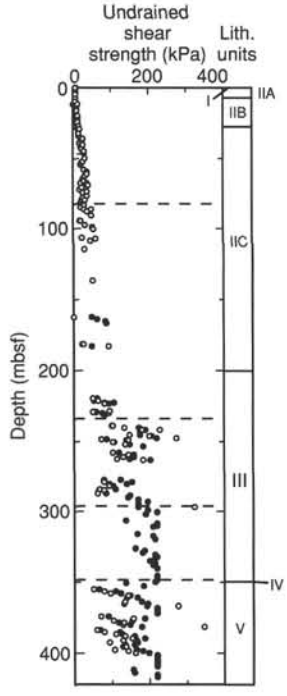

Figure 24. Undrained shear strength (open circles) and assumed undrained shear strength derived from unconfined compressive strength (solid circles) in Holes 931A and 931B. Shear strength values of 220 kPa estimated from the unconfined compressive strength represent minimum values. Dashed lines indicate boundaries of shear-strength divisions discussed in the text.

and Fe yields are relatively high and gradually increase downhole. Below 113 mbsf, a distinct shift to lower gamma ray, resistivity, and velocity is seen. Borehole diameter is greatest near 140 mbsf, where core recovery was lowest. Between 140 and 157 mbsf, the velocity, density, and porosity values fluctuate widely and are accompanied by peaks in Si yields, indicative of the presence of quartz-rich sand beds.

Logging Unit 2 (157–182 mbsf) is characterized by distinct boundaries at its base and top. A significant increase is observed in gamma-ray counts of 30 to 35 API units, compared with the units above and below. This increase is also accompanied by (1) an abrupt decrease in magnetic susceptibility, (2) sharp increases in resistivity, (3) decreasing values of sonic velocity, density, and porosity, (4) distinct increases in Al and K concentrations and Fe yields, and (5) decreasing Si. The relatively high uranium content, similar to that observed in logging Unit 1, suggests that this unit may also be high in organic matter.

Logging Unit 3 (182–220 mbsf) is characterized by a shift to logging values similar to those in logging Unit 1. There appears to be a series of three to four fining-upward subunits, based on the gamma-ray, sonic velocity, magnetic susceptibility, and Si yield logs. The sonic velocity, density, and porosity log values also fluctuate widely, as in the lower part of logging Unit 1, which indicates the possible presence of interbedded sandy intervals.

Logging Unit 4 (220–251.6 mbsf) is characterized by an abrupt increase in resistivity that gradually increases downhole to the highest values recorded at Hole 931B. The marked decline in resistivity between 207 and 212 mbsf may be the result of borehole washout. The top of logging Unit 4 also has a distinct increase in Al (%), and Ca and S yields show markedly lower relative concentrations. Magnetic susceptibility shifts to lower values, similar to logging Subunit 1A and Unit 2.

Formation MicroScanner (FMS) Tool

Preliminary shipboard processing and analysis suggest that the FMS produced good quality high-resolution data. All pads were in contact with the borehole wall, except in washed-out intervals, most of which were less than 1 m thick. A second pass was made, but unfortunately additional coverage was obtained only in the interval between 185 and 230 mbsf.

Orthogonal two-arm caliper pair data reveal the degree and orientation of borehole ellipticity (Fig. 30). From the top of the logged interval to approximately 157 mbsf, the borehole is distinctly elliptical in shape, with the long axis oriented north-northeast/south-southwest, approximately parallel to the regional bathymetric contours. Between approximately 185 and 230 mbsf, the borehole was nearly circular. The transition in borehole shape occurs at the boundary between logging Units 2 and 3. The slight borehole ellipticity between 185 and 230 mbsf indicates that the minimum horizontal stress is oriented west-northwest/east-southeast, approximately perpendicular to the regional bathymetric contours.

Temperature Tool

We first deployed the TLT on the Quad-combination string 7 hr after hole conditioning was completed; we measured temperatures between 5.2° and 5.4°C at 250 mbsf (Fig. 31). The second run of the tool, when attached to the GLT tool string, 9 hr after the first run, recorded an increased temperature of 6.5° to 6.6°C at 250 mbsf, revealing a rebound of borehole temperature.

Noticeable downhole changes were seen in the temperature gradient (Fig. 31). Four broad intervals (A, B, C, and D) have been defined on the basis of similar trends that were revealed in the two wireline and one in-situ temperature curves (see "In-situ Temperature Measurements" section, this chapter). Steps in the geothermal gradient show higher gradients in intervals A and C and lower gradients in intervals B and D. These may be related to downhole changes in thermal conductivity, or to advection of formation water into the borehole.

Geological High-sensitivity Magnetic Tool (GHMT-A) Results

Total induction and magnetic susceptibility were recorded, respectively, by the scalar magnetometer (NMRS) and the susceptometer (SUMS). Repeat logging runs allowed for the analysis of the different components of the borehole magnetic environment that affect the measurement of magnetization of the surrounding formation. A detailed review of these sensors and principles of magnetic logging are provided in the "Explanatory Notes" chapter (this volume). During the approximately 3-hr logging time, the total field and susceptibility logs were affected by time-dependent (transient variations in Earth's field, temperature drift) and time-invariant (magnetic mineral concentration, remanent magnetization) factors. Post-cruise data pro-

Table 14. Electrical resistivity at Site 931

Core, section, interval (cm)	Depth (mbsf)	Longitudinal resistivity (Ωm)	Transverse resistivity (Ωm)
155-931A-			
1H-1, 12	0.12	0.439	0.399
1H-3, 43	3.43	0.348	0.371
155-931B-			
2H-1, 84	1.64	0.446	0.402
2H-2, 77	3.07	0.422	0.408
2H-3, 90	4.70	0.460	0.462
2H-5, 43	7.23	0.401	0.417
2H-6, 13	8.43	0.423	0.436
2H-7, 27	10.07	0.442	0.424
3H-1, 130	11.60	0.444	0.448
3H-2, 95	12.75	0.461	0.461
3H-3, 78	14.08	0.452	0.455
3H-4, 111	15.91	0.483	0.427
3H-5, 23	16.53	0.424	0.412
3H-6, 113	18.93	0.461	0.466
3H-7, 76	20.06	0.454	0.483
4H-1, 37	20.17	0.439	0.436
4H-2, 32	21.62	0.476	0.456
4H-3, 58	23.38	0.472	0.486
4H-4, 15	24.45	0.498	0.466
4H-5, 40	26.20	0.471	0.488
4H-6, 37	27.67	0.493	0.498
4H-7, 36	29.16	0.453	0.467
5H-1, 33	29.63	0.457	0.412
5H-2, 33	31.13	0.509	0.484
5H-3, 33	32.63	0.499	0.456
5H-4, 36	34.16	0.560	0.496
5H-5, 32	35.62	0.502	0.463
5H-6, 38	36.48	0.560	0.445
5H-7, 28	37.88	0.574	0.493
6H-1, 29	39.09	0.525	0.506
6H-2, 16	40.46	0.580	0.543
6H-3, 51	42.31	0.626	0.491
6H-4, 29	43.59	0.590	0.476
6H-5, 34	45.14	0.593	0.463
6H-6, 36	46.66	0.618	0.612
6H-7, 64	48.44	0.649	0.532
7H-2, 15	49.95	0.716	0.528
7H-3, 102	52.32	0.661	0.520
7H-4, 37	53.17	0.546	0.494
7H-5, 26	54.56	0.536	0.498
7H-7, 12		0.509	0.430
8H-1, 30	58.10	0.521	0.488
8H-2, 45	59.75	0.569	0.516
8H-3, 30	61.10	0.560	0.523
8H-4, 38	62.68	0.587	0.510
8H-5, 122	65.02	0.574	0.618
8H-6, 124	66.54	0.554	0.500
8H-7, 81	67.61	0.599	0.626
9H-1, 37	67.67	0.537	0.486
9H-2, 31	69.11	0.502	0.512
9H-3, 37	70.67	0.596	0.589
9H-4, 37	72.17	0.626	0.536
9H-5, 135	74.65	0.568	0.534
9H-6, 38	75.18	0.565	0.539
9H-7, 77	77.07	0.619	0.587
10X-1, 112	77.92	0.674	0.651
10X-2, 116	79.46	0.784	0.736
10X-3, 23	80.03	0.777	0.678
10X-4, 88	82.18	0.767	0.738
10X-5, 110	83.35	0.469	0.518
11X-1, 75	85.05	0.458	0.463
11X-2, 75	86.55	0.463	0.451
11X-3, 76	88.06	0.572	0.586
11X-4, 75	89.55	0.505	0.461
11X-5, 77	91.07	0.478	0.469
12X-1, 79	94.69	0.500	0.487
12X-2, 79	96.19	0.481	0.444
12X-3, 80	97.70	0.510	0.499
12X-4, 39	98.79	0.504	0.484
12X-5, 15	100.05	0.484	0.472
13X-1, 80	104.30	0.451	0.460
13X-2, 96	105.96	0.470	0.479
13X-3, 78	107.28	0.485	0.482
13X-4, 34	108.34	0.484	0.464
14X-1, 115	114.35	0.501	0.488
15X-1, 96	123.76	0.450	0.480
16X-3, 78	136.28	0.507	0.504
19X-1, 79	162.29	0.469	0.518
19X-2, 78	163.78	0.517	0.499
19X-3, 80	165.30	0.486	0.529
19X-4, 97	166.97	0.512	0.504
21X-1, 90	181.60	0.637	0.516
21X-2, 90	183.10	0.790	0.748
25X-1, 91	220.01	0.659	0.719
25X-2, 87	221.47	0.624	0.676
25X-3, 77	222.87	0.755	0.626
25X-4, 34	223.94	0.605	0.753
26X-1, 60	229.30	0.831	0.691
26X-2, 36	230.56	0.888	0.901
26X-3, 4	231.74	0.807	0.729
27X-1, 78	239.18	1.180	1.015
27X-2, 70	240.60	0.869	0.815
27X-3, 74	242.14	1.352	0.867
27X-4, 74	243.64	0.858	0.787
27X-5, 109	245.49	1.025	0.836
27X-6, 75	246.65	1.009	0.943
27X-7, 37	247.77	0.923	1.051
28X-1, 67	248.67	0.704	0.822
28X-2, 15	249.52	0.752	0.837
28X-3, 75	250.72	0.890	0.697
28X-4, 75	252.22	0.906	0.806
28X-5, 75	253.72	0.987	0.889
29X-1, 75	258.45	0.677	0.683
29X-2, 75	259.95	0.678	0.702
29X-3, 75	261.45	0.778	0.897
29X-4, 86	263.06	0.668	0.729
29X-5, 13	263.83	0.967	1.141
31X-1, 75	277.65	0.715	0.806
31X-2, 73	279.13	0.678	0.759
31X-3, 65	280.55	0.815	0.872
31X-4, 74	282.14	0.834	0.755
31X-5, 92	283.82	0.799	0.733
31X-6, 26	284.66	0.581	0.635
32X-1, 62	287.22	0.623	0.601
32X-2, 66	288.76	0.594	0.601
32X-3, 58	290.18	0.602	0.614
32X-4, 75	291.85	0.600	0.602
32X-5, 58	293.18	0.599	0.610
32X-6, 58	294.68	0.602	0.587
33X-1, 79	296.99	0.599	0.610
33X-2, 90	298.60	0.621	0.642
33X-3, 91	300.11	0.600	0.624
33X-4, 79	301.49	0.630	0.635
34X-1, 75	306.55	0.619	0.563
34X-2, 113	308.43	0.576	0.586
34X-3, 116	309.96	0.605	0.629
34X-4, 55	310.85	0.616	0.555
35X-1, 52	316.02	0.576	0.604
35X-2, 66	317.66	0.647	0.641
35X-3, 77	319.27	0.724	0.691
36X-1, 98	326.08	0.641	0.677
36X-2, 87	327.47	0.590	0.677
36X-3, 94	329.04	0.604	0.599
36X-4, 78	330.38	0.565	0.620
36X-5, 68	331.78	0.626	0.604
36X-6, 56	333.16	0.566	0.575
37X-1, 53	335.33	0.642	0.676
37X-2, 59	336.89	0.693	0.650
37X-3, 55	338.35	0.650	0.663
37X-4, 62	339.92	0.668	0.663
38X-1, 80	345.20	0.580	0.542
38X-2, 60	346.50	0.691	0.799
38X-3, 61	348.01	0.733	0.711
38X-4, 57	349.47	0.524	0.489
38X-5, 81	350.75	0.494	0.478
38X-7, 78	352.57	0.669	0.667
39X-1, 80	354.90	0.564	0.513
39X-2, 77	356.37	0.605	0.602
39X-3, 80	357.90	0.640	0.559
39X-4, 80	359.40	0.642	0.600
39X-5, 75	360.85	0.652	0.624
40X-1, 25	363.95	0.882	0.678
40X-2, 75	365.21	0.749	0.663
40X-3, 74	366.70	0.857	0.814
40X-4, 76	368.22	0.768	0.871
40X-5, 75	369.71	0.731	0.712
40X-6, 57	371.03	0.624	0.618
40X-7, 57	371.78	0.674	0.703
41X-1, 75	374.15	0.613	0.534
41X-2, 75	375.65	0.628	0.759
41X-3, 75	377.15	0.713	0.681
41X-4, 73	378.63	0.643	0.559
41X-5, 75	380.15	0.588	0.588
41X-6, 72	381.62	0.619	0.598
42X-1, 75	383.65	0.624	0.527
42X-2, 75	385.15	0.631	0.640
42X-3, 75	386.65	0.632	0.559
42X-4, 75	388.15	0.678	0.653
42X-5, 75	389.65	0.622	0.706
42X-6, 76	391.16	0.628	0.589
43X-1, 45	392.85	0.666	0.590
43X-2, 75	394.22	0.567	0.528
43X-3, 75	395.72	0.587	0.649
43X-4, 107	397.54	0.763	0.638
43X-5, 77	398.74	0.673	0.714
43X-6, 75	400.22	0.618	0.597

Table 14 (continued).

Core, section, interval (cm)	Depth (mbsf)	Longitudinal resistivity (Ωm)	Transverse resistivity (Ωm)
43X-7, 79	401.76	0.758	0.902
44X-2, 15	402.52	0.793	0.706
44X-3, 70	404.51	0.737	0.634
44X-4, 49	405.80	0.639	0.568
44X-5, 47	406.85	0.640	0.600
44X-6, 49	408.23	0.653	0.621
44X-7, 47	409.42	0.545	0.512
45X-1, 50	412.10	0.555	0.567
45X-2, 54	413.64	0.575	0.629
45X-3, 54	415.14	0.635	0.638
45X-4, 54	416.64	0.629	0.587

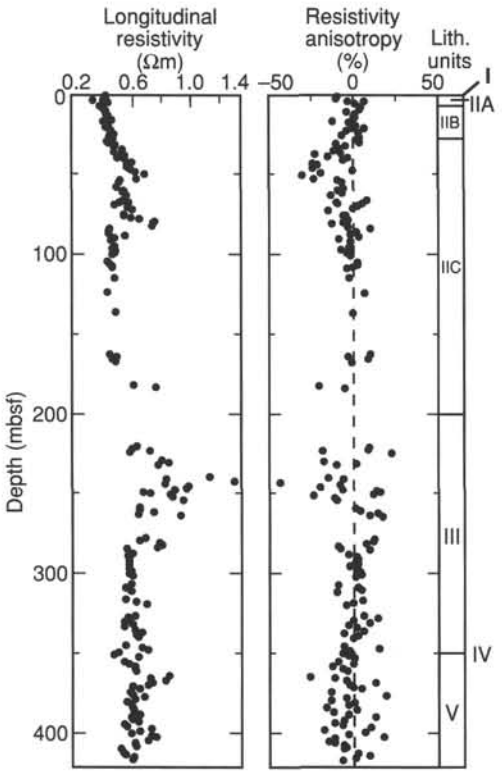

Figure 25. Longitudinal resistivity and resistivity anisotropy in Holes 931A and 931B.

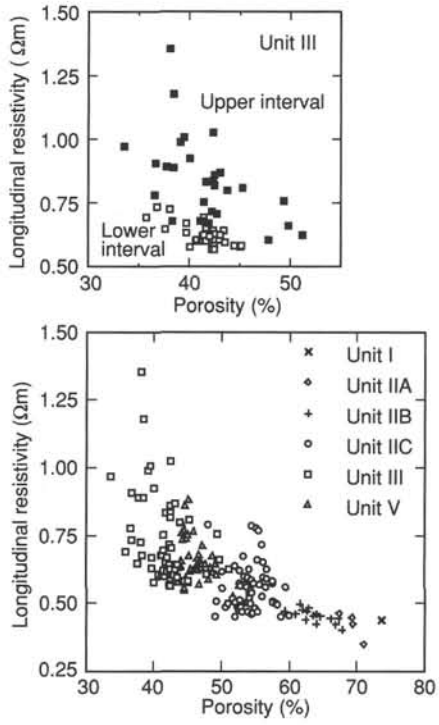

Figure 26. Porosity vs. longitudinal resistivity in Holes 931A and 931B. The range encompassing Unit III is expanded to show the variation in characteristics of the upper (solid squares) and lower (open squares) intervals of this unit. The boundary between these intervals is at approximately 265 mbsf.

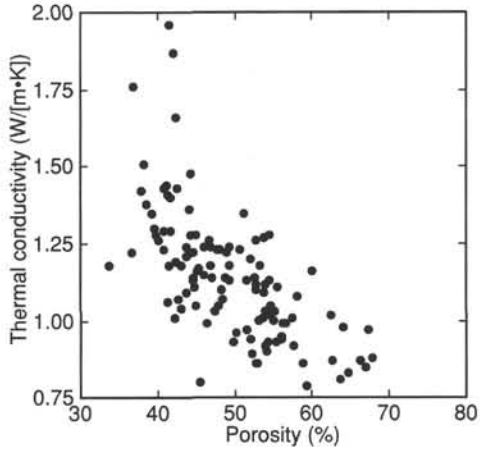

Figure 27. Porosity vs. thermal conductivity in Holes 931A and 931B.

cessing will isolate further and quantify these factors and may provide results about the orientation of the paleomagnetic field. We discuss the quality of magnetometer and susceptometer data below and compare these data with core susceptibility data and lithologic observations. Comparisons with core data from recovered intervals should allow for extrapolation of core susceptibility data to intervals of poor core recovery.

Total Induction Log

We removed the contribution of the Earth's inner dipole field induction, **Br**, from the total field **B**, measured by the magnetometer, using the local value of 29,614 nT and its gradient as a linear function of depth (approximately 22 nT/km). In Figure 32, we show the remaining local field $\mathbf{B}_L(z)$ for the two runs, which contain only local effects:

$\mathbf{B}_{L1}(z) = \mathbf{Bf}(z) + \mathbf{Ba}(z) + \mathbf{Bt1}(z, t)$ and $\mathbf{B}_{L2}(z) = \mathbf{Bf}(z) + \mathbf{Ba}(z) + \mathbf{Bt2}(z, t)$.

A shift toward high values, between 84 and 120 mbsf (first run) and between 114 and 130 mbsf (second run) is caused by the highly magnetic BHA (Fig. 32). Apart from several spikes, the interval between 130 and 245 mbsf has little magnetic variation with average values of the local fields $\mathbf{B}_{L1}$ and $\mathbf{B}_{L2}$ of about 100 nT. The true value of **Bf**, the magnetization component of the formation, can be obtained by evaluating the anomaly field **Ba** and the transient fields **Bt**1 and **Bt**2.

Table 15. Thermal conductivity at Site 931.

Core, section, interval (cm)	Depth (mbsf)	Thermal conductivity (W/[m·K])
155-931B-		
2H-5, 42	7.22	0.88
2H-6, 40	8.70	0.85
2H-7, 39	10.19	0.87
3H-1, 70	11.00	0.97
3H-3, 70	14.00	0.83
3H-5, 70	17.00	0.98
3H-7, 70	20.00	0.81
4H-1, 60	20.40	1.02
4H-3, 60	23.40	0.87
4H-5, 60	26.40	0.79
4H-7, 60	29.40	0.86
5H-1, 50	29.80	1.16
5H-2, 50	31.30	1.01
5H-3, 50	32.80	1.08
5H-5, 50	35.80	0.92
6H-1, 50	39.30	0.95
6H-3, 50	42.30	0.99
6H-5, 50	45.30	0.99
6H-7, 50	48.30	0.94
7H-1, 60	48.90	1.00
7H-3, 60	51.90	0.93
7H-5, 40	54.70	0.90
7H-6, 75	56.55	0.91
8H-1, 33	58.13	1.12
8H-3, 46	61.26	1.09
8H-5, 110	64.90	0.86
8H-6, 114	66.44	0.96
9H-1, 75	68.05	1.28
9H-3, 75	71.05	0.92
9H-5, 75	74.05	1.01
9H-6, 75	75.55	0.86
10X-1, 58	77.38	1.18
10X-2, 58	78.88	1.02
10X-3, 58	80.38	1.03
10X-4, 60	81.90	1.11
11X-1, 75	85.05	1.13
11X-2, 75	86.55	1.05
11X-4, 75	89.55	1.27
11X-5, 75	91.05	1.14
12X-1, 80	94.70	0.93
12X-2, 80	96.20	1.00
12X-3, 80	97.70	1.10
12X-5, 20	100.10	1.23
13X-1, 80	104.30	1.22
13X-2, 80	105.80	1.00
13X-4, 40	108.40	0.89
15X-1, 92	123.72	1.20
15X-2, 85	125.15	0.82
15X-3, 92	126.72	1.26
16X-1, 75	133.25	1.15
16X-2, 100	135.00	0.98
16X-3, 75	136.25	1.24
19X-1, 80	162.30	1.03
19X-2, 80	163.80	1.13
19X-3, 80	165.30	1.26
19X-4, 96	166.96	0.97
21X-1, 90	181.60	0.94
21X-2, 90	183.10	1.23
23X-1, 50	200.30	1.32
23X-2, 50	201.80	1.02
25X-1, 90	220.00	0.93
25X-2, 75	221.35	1.35
25X-3, 90	223.00	1.13
25X-4, 90	224.50	1.05
27X-1, 75	239.15	1.38
27X-3, 75	242.15	1.51
27X-5, 75	245.15	1.66
27X-6, 75	246.65	1.30
28X-1, 75	248.75	1.07
28X-3, 75	250.72	1.42
28X-4, 75	252.22	1.76
28X-5, 75	253.72	1.35
29X-1, 75	258.45	1.44
29X-3, 75	261.45	1.22
29X-4, 75	262.95	1.87
29X-5, 15	263.85	1.18
31X-1, 50	277.40	1.01
31X-2, 50	278.90	1.41
31X-3, 50	280.40	1.43
31X-5, 50	283.40	1.09
32X-1, 60	287.20	1.04
32X-3, 60	290.20	1.18
32X-4, 60	291.70	1.29
32X-5, 60	293.20	1.23
33X-1, 75	296.95	1.06
33X-2, 75	298.45	1.18
33X-3, 75	299.95	1.29
33X-4, 75	301.45	1.28
34X-1, 50	306.30	1.06
34X-2, 50	307.80	1.26
34X-3, 50	309.30	1.43
37X-1, 75	335.55	1.19
37X-2, 85	337.15	1.96
37X-3, 75	338.55	1.40
38X-1, 77	345.17	1.13
38X-3, 65	348.12	1.13
38X-5, 77	350.71	0.98
38X-7, 77	352.56	1.19
39X-1, 60	354.70	1.12
39X-3, 60	357.70	1.18
39X-4, 60	359.20	1.23
39X-5, 60	360.70	1.18
40X-2, 75	365.21	1.16
40X-3, 75	366.71	1.11
40X-4, 75	368.21	1.22
40X-5, 75	369.71	1.28
41X-1, 75	374.15	1.14
41X-3, 75	377.15	1.03
41X-5, 75	380.15	1.28
41X-6, 75	381.65	1.26
42X-1, 75	383.65	1.07
42X-3, 75	386.65	0.99
42X-5, 75	389.65	1.15
42X-6, 75	391.15	1.14
43X-2, 50	393.97	1.24
43X-3, 50	395.47	1.10
43X-4, 50	396.97	1.24
43X-5, 50	398.47	1.17
43X-6, 50	399.97	0.80
44X-2, 50	402.87	1.22
44X-3, 50	404.31	1.05
44X-5, 50	406.88	1.41
44X-6, 50	408.24	1.48
45X-1, 50	412.10	1.14
45X-2, 50	413.60	1.21
45X-3, 50	415.10	1.36
45X-4, 50	416.60	1.24

Table 16. Intervals logged and tools employed in Hole 931B.

String	Run	Open hole (mbsf)	Open hole (mbrf)	In pipe (mbsf)	In pipe (mbrf)	Tools
Quad	Down and up 1	251–93	3738–3580			NGT/LSS/CNT-G/HLDT/DITE/TLT
	Up 2	150–71	3637–3558			
FMS	Up 1	250–93	3737–3580			NGT/GPIT/FMS
	Up 2	250–93	3737–3580			
GLT	Up 1	250–72	3737–3559	72–0	3559–3487	NGT/CNTG/AACT/GST/TLT
	Up 2	113–100	3600–3587	100–0	3587–3487	
GHMT-A	Up 1	240–85	3727–3572			NGT/SUMS/NMRS
	Up 2	240–115	3727–3542			

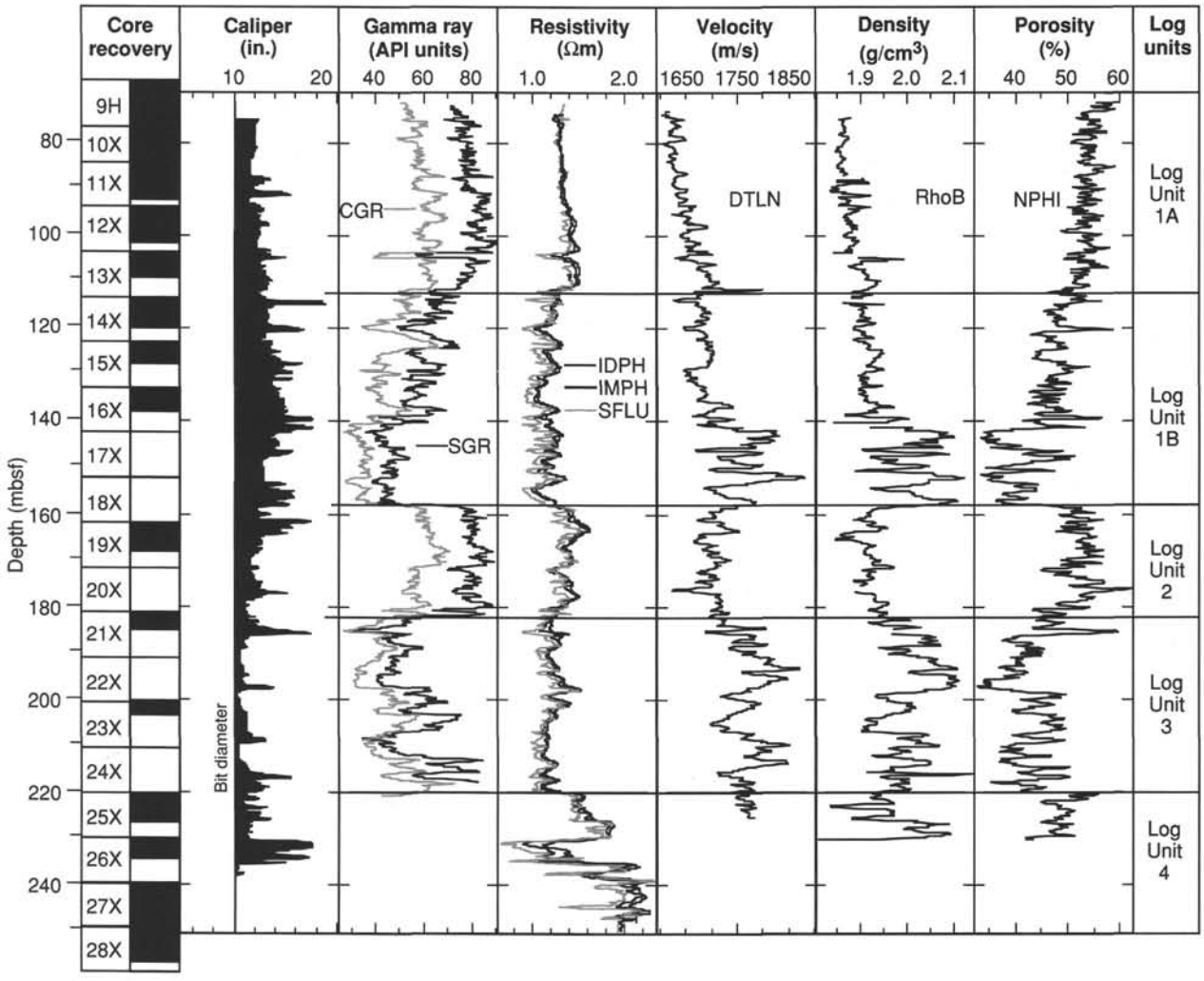

Figure 28. Hole 931B Quad-combination tool results. CGR (Th + K) = computed gamma ray, SGR = spectroscopy gamma ray, IDPH = deep-induction phasor resistivity, IMPH = medium-induction phasor resistivity, SFLU = shallow spherically focused resistivity, DTLN = short-spacing interval transit time converted to velocity, RhoB = bulk density, and NPHI = neutron porosity. The logged section has been divided into four logging units.

Analysis of the Components of the Magnetic Induction

In Figure 32, one can see that the difference of the "local" fields between the two runs ($\mathbf{B}_{L1} - \mathbf{B}_{L2}$) is very small, which is indicative of the absence of transient magnetic phenomena. The drift in difference ($\mathbf{B}_{L1} - \mathbf{B}_{L2}$) in the upper interval results from the lower position of the BHA during the repeat log, $\mathbf{B}_{L2}$. This perturbation can usually be removed, assuming a dipolar effect, and allows for data recovery up to about 10 m beneath the BHA. Discrete sharp variations in the difference ($\mathbf{B}_{L1} - \mathbf{B}_{L2}$) occur near zones where there is a steep gradient of the local B field; these variations correspond to small depth errors. Only low frequency variations ($\leq 5 \cdot 10^{-3}$ Hz, which is ≥30 m interval) affect the recorded values (skin effect), because these measurements were performed under more than 3000 m of conductive seawater.

In Figure 32, we illustrate an overall positive value of the remaining "local" field $\mathbf{B}_{L1}$, centered around 110 nT, below about 130 mbsf. This average value of **Bf** is slightly higher than expected. Average susceptibility and remanent intensity values from the core and sample measurements are, respectively, 10^{-3} SI and 10^{-2} A/m and imply a field of 45 nT [$\mathbf{Bf}(\text{nT}) = \mu_o(\text{Ji} + \text{Jr})$ (A/m)], with a corresponding average Koenigsberger ratio (Jr/Ji) of 0.4. Projected on the actual field direction (scalar magnetometer), the effect should be about 30 nT on the GHMT-A's total field sensor. Hole 931B is located in a positive anomaly field (**Ba** < 80 nT). However, the short record length (in depth) does not allow us to confirm an obvious positive trend superimposed on the sedimentary magnetic record. Precise estimation of **Ba** will require further analysis.

Analysis of Susceptibility Records

The magnetic susceptibility data in Hole 931B appear to be of good quality. In Figure 33, one can see the results of the two logging runs, as well as the difference between the two runs (k1 – k2). Good correlation is found between the records, indicating few measurement errors and little thermal drift of the measurement coils. A small and relatively constant difference of approximately 20 ppm is observed between the two runs. Thermal drift is a function of the external temperature measured at the receiving coil and the temperature difference between the active and receiving coils. Although the internal temperature of the tool increased during logging, temperature differences between the two runs remained within 1°C, which is consistent with the known thermal drift of the tool. Observed differ-

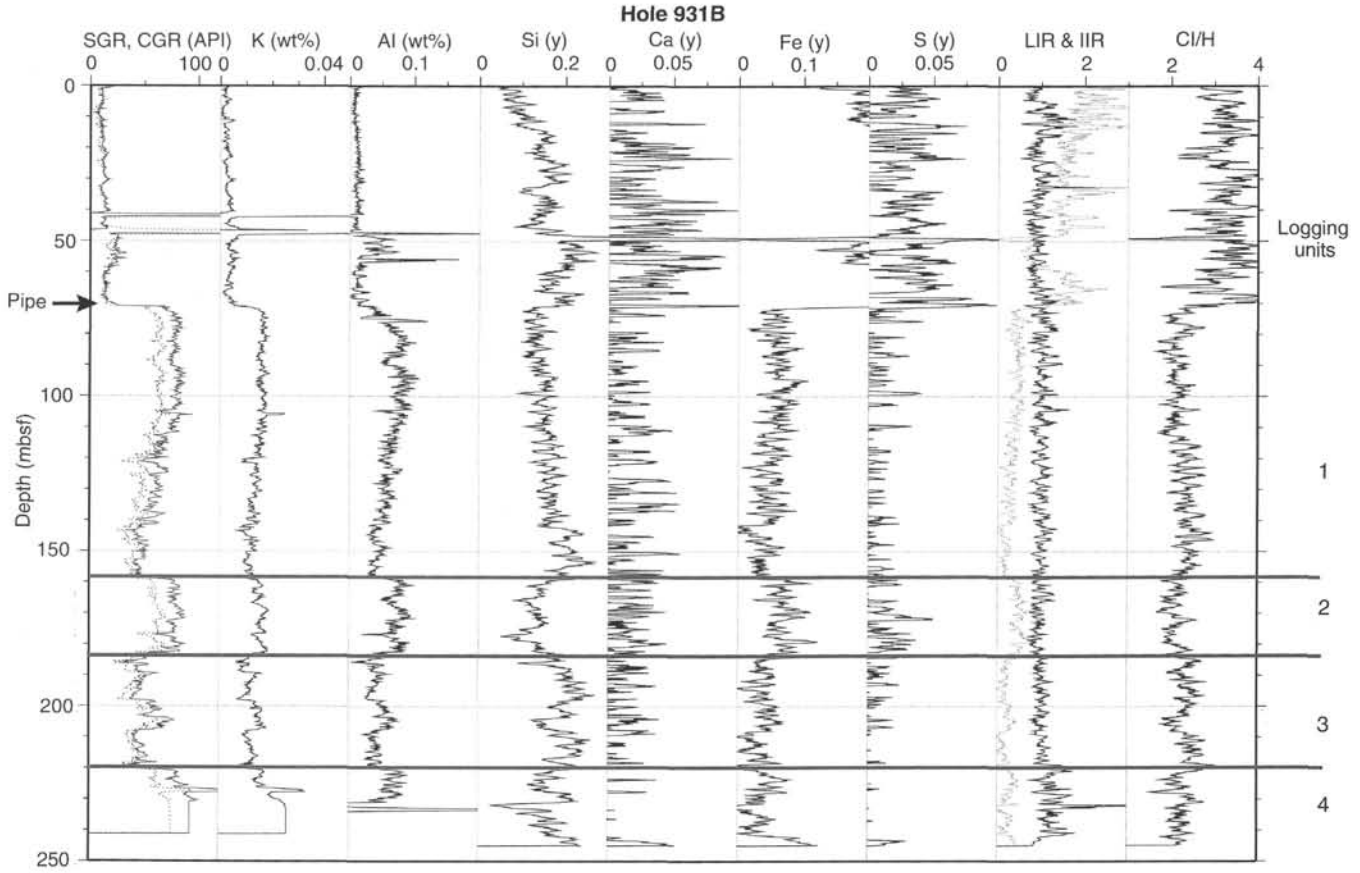

Figure 29. Geochemical logging tool data from Hole 931B for the entire logged interval. K and Al are concentrations (in wt%); elements of Si, Ca, Fe, and S are in relative yields; LIR and IIR are, respectively, the lithology and iron indicator ratios [Si/(Si+Ca) and Fe/(Si+Ca)]; Cl/H = the ratio of the yields of Cl and H; for other measurements see Figure 28. Note that the interval above 71 mbsf was logged in drill pipe.

ences between the runs (k1 – k2) appear to be associated with zones of high susceptibility gradients and may be related to small depth errors.

Comparison of Magnetic Logging with Core Data

In Figure 34, we compare the "local" **B** field, obtained from the first magnetometer run ($\mathbf{B}_{L1}$, in units of nT), with susceptibility (k1, in units of ppm), and with whole-core susceptibilities (in units of 10^{-6} SI). Despite poor core recovery in the logged interval, laboratory measurements have a finer vertical resolution as a result of the difference in sample volume that the tools measure. Core data are derived from a small (and usually variable) volume of material. In contrast, the GHMT-A's susceptibility sensor integrates a much larger volume of sediment, which lowers resolution (vertical resolution of the tool is related to its depth of investigation).

Comparison with Lithology

Logging Units 1 and 2 and the upper portion of logging Unit 3 correspond to lithostratigraphic Subunit IIC. The lower portion of logging Unit 3 and all of logging Unit 4 correspond to lithostratigraphic Unit III. The change in resistivity and gamma ray below 113 mbsf corresponds to pronounced downhole increase in sand content in the sediment. Thick and massive, quartz-rich sand beds are inferred to occur between 140 and 157 mbsf, based on the character of the gamma-ray, velocity, density, and porosity logs. Similar lithologies were obtained in Core 931B-19X and 931B-21X, but signatures are markedly different between the two intervals, which suggests a change in mineralogy. The increase in concentrations of K and Al, together with a decrease in Si yield, suggest a higher concentration of feldspars. Shipboard analyses indicate the presence of plagioclase within the interval of logging Unit 2; however, detailed shore-based analyses will be needed to confirm the mineralogical composition.

According to the lithostratigraphic interpretation, the upper interval of Unit III is composed of mass-flow units that overlie a thick debris flow below 225 mbsf. Logging responses indicate a change in gamma ray, velocity, density, and porosity at 198 mbsf (top of lithostratigraphic Unit III). We also observed a more significant change in resistivity and gamma ray at 220 mbsf (top of logging Unit 4) that is consistent with the apparent change in lithology suggested between Cores 931B-24X (no recovery) and -25X (see "Lithostratigraphy" section, this chapter).

Generally, lower magnetic susceptibilities and high gamma-ray counts tend to occur in clay-dominated intervals. The presence of hematite-staining, noted around coarse-sand grains, could be responsible for the higher magnetic susceptibility values in coarser grained intervals (e.g., between 118 and 159 mbsf).

CORE-SEISMIC INTEGRATION

Site 931 was positioned at 1410 UTC on 5 April 1994 on an 80-in.^{3} water-gun seismic reflection line obtained on Leg 155 (Fig. 35). Hole 931B was drilled to 421.3 mbsf through Channel-levee System

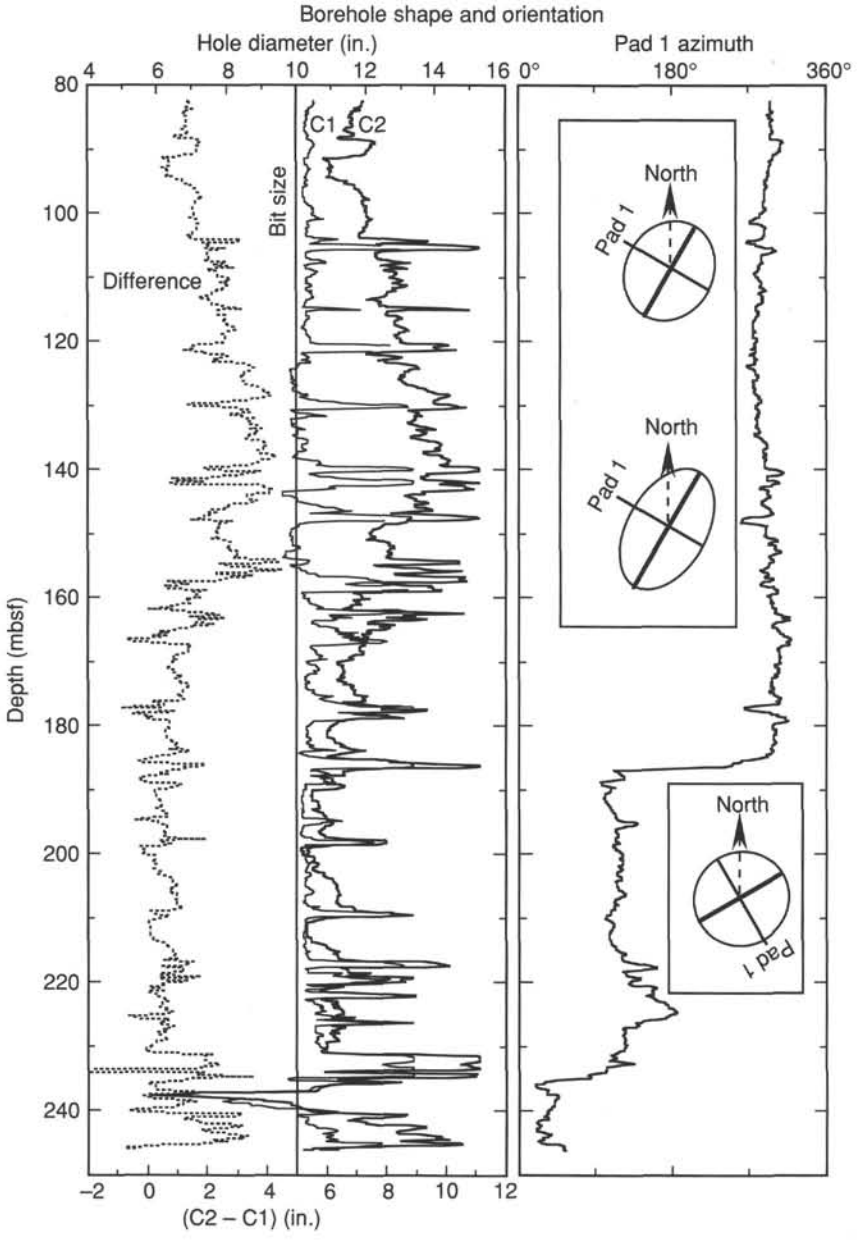

Figure 30. Data from the two FMS calipers (C1, C2) [maximum value = 15 in. (38 cm)] and the difference (C1 – C2) in Hole 931B. Borehole ellipticity and its azimuth are shown on the right.

5 (Damuth et al., 1983) and into a channel-levee system that is part of the Bottom Levee Complex (Manley et al., 1988).

Five moderate- to high-amplitude reflections mark the boundaries between six seismic-facies units and are identified at 20, 35, 180, 290, and 410 ms sub-bottom (Fig. 35). The 3.5-kHz echograms (Fig. 2) were used to classify seismic-facies Unit 1 between the seafloor and 20 ms sub-bottom and seismic-facies Unit 2 from 20 to 35 ms. Seismic-facies Unit 1 is characterized by continuous, parallel reflections. Seismic-facies Unit 2 is characterized by continuous, low-amplitude reflections, which diverge toward the axis of Channel 5. Low-amplitude, continuous, subparallel reflections compose seismic-facies Unit 3 (35–180 ms) within the flank of Channel-levee System 5. Seismic-facies Unit 4 (180–290 ms) is characterized by high-amplitude, continuous, parallel reflections. The top of Unit 4 correlates to a reflector that marks the top of a HARP unit associated with Channel-levee System 5. The distal flanks of two older channels (termed 5A and 5B by Damuth et al., 1983) located to the west of Site 931 are within this HARP unit. Seismic-facies Unit 5 is characterized by chaotic reflections and extends from 290 to 410 ms. Low-amplitude, discontinuous, parallel to convergent reflections characterize Unit 6 and extend to 550 ms.

Synthetic Seismogram

Velocity and density profiles were determined from downhole logging between 75 and 225 mbsf (Fig. 36). A function based on velocity and bulk density determined from these log data was used to extrapolate velocities from the discrete wet-bulk densities measured on the core. Good agreement occurs between the in-situ velocities and those calculated from the discrete bulk-density values. A time vs. depth relationship was then determined from these merged data (Fig. 37; Table 10 of "Explanatory Notes" chapter, this volume) and used for the core-seismic integration.

A synthetic seismogram (Fig. 38) was produced using a two-way traveltime to the first log data based on an average constant velocity of 1700 m/s between the seafloor and 75 mbsf. The water-gun source

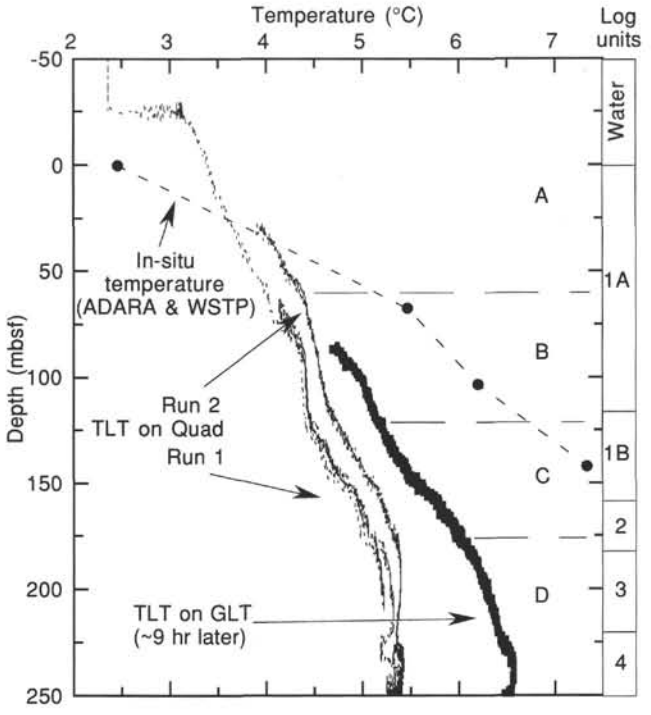

Figure 31. Data from two runs of the temperature logging tool in Hole 931B. A delay of 9 hr occurred between the two runs. Four broad intervals (A, B, C, and D) denote noticeable downhole changes in the temperature gradient. Logging units are shown on the right.

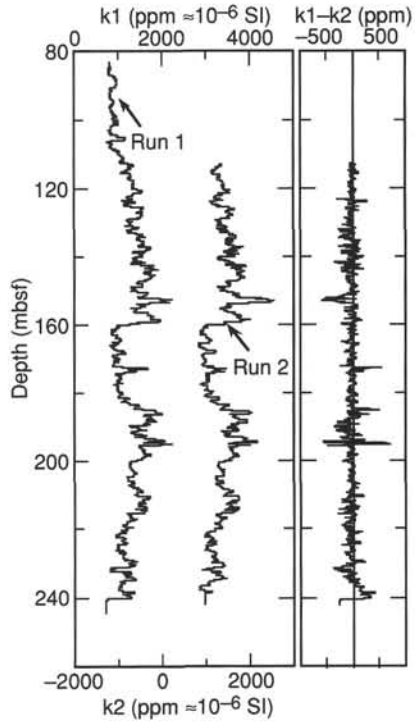

Figure 33. Downhole susceptibility in Hole 931B for the two runs and the difference, k1 – k2, between the two runs. The scale shift between runs is 2000 ppm.

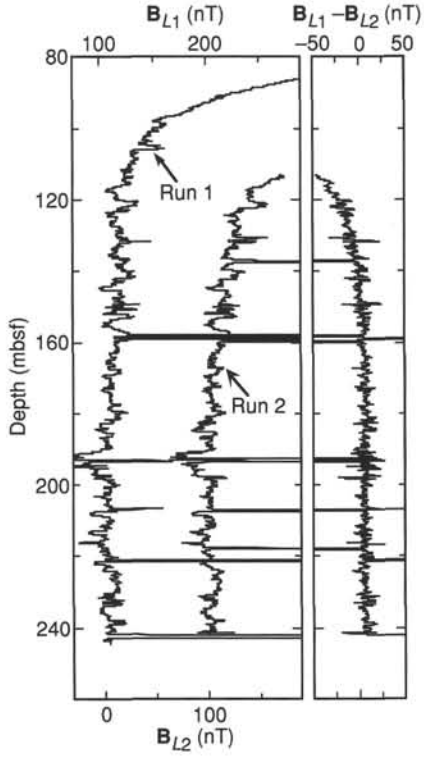

Figure 32. Hole 931B downhole local total induction for the two successive runs ($\mathbf{B}_{L1}$ and $\mathbf{B}_{L2}$), and the difference ($\mathbf{B}_{L1} - \mathbf{B}_{L2}$). Scale shift between runs is 100 nT.

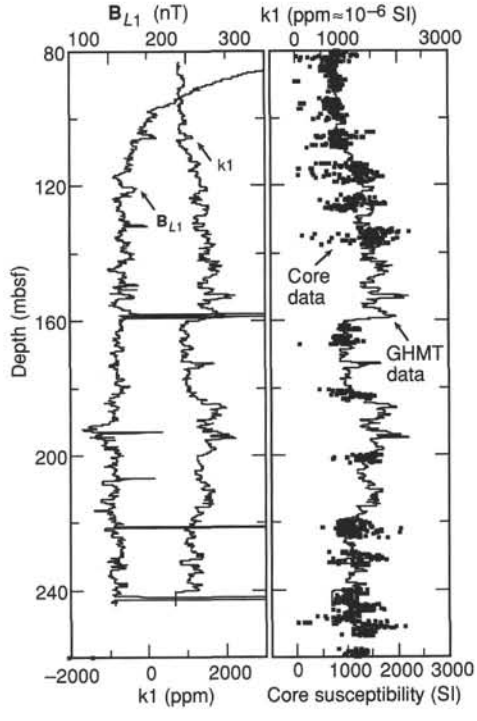

Figure 34. Local total induction B_{L1} and susceptibility k1 for the first run, and comparison between downhole susceptibility, k1, and susceptibility values obtained from core measurements.

signature was extracted by combining the near seafloor arrivals of 10 traces within the vicinity of the site. The synthetic seismogram shows the location of the prominent reflections at the top and bottom of seismic-facies Unit 5. The base of seismic-facies Unit 5 shows a reverse polarity with respect to the source signature. The section of poor core recovery (between 140 and 220 mbsf) is dominated by high-frequency reflections of intermediate to high amplitude (Fig. 38).

Core-seismic Correlation

Seismic-facies units correlate reasonably well with the defined lithostratigraphic units (Fig. 39). Seismic-facies Unit 1 correlates with lithologic Unit I, Subunit IIA, and the upper 8 m of Subunit IIB. Seismic-facies Unit 2 can be correlated to the lower part of lithologic Subunit IIB, and the subparallel reflections, which are divergent toward the levee crest, are probably returned from the thin silt laminae within the silty clay (Fig. 39). Seismic-facies Unit 3 is within the channel-levee flank, and the continuous reflections probably are associated with an increase in frequency and thickness of silt beds in lithologic Subunit IIC compared to Subunit IIB. The prominent reflection at 35 ms corresponds to the interface between lithostratigraphic Subunits IIB and IIC, which is also the interface between seismic-facies Units 2 and 3. The base of seismic-facies Unit 3 is the upper contact of the HARPs of Unit 4. Unfortunately, this interface was not recovered in the cores. Downhole log data suggest that this region consists of interbedded sand and clay (see "Downhole Logging" section, this chapter). This is in agreement with the high-frequency character seen on the synthetic seismogram. The prominent reflection between seismic-facies Units 4 and 5 at 290 ms occurs at 235 mbsf, some 35 m below the top of lithologic Unit III. The chaotic seismic facies of Unit 5 is associated with the mass-transport deposits of lithologic Unit III. Near the base of the hole, the color-banded silty-clay sediment with thin silt laminae, seen in lithologic Unit V, corresponds to the discontinuous, parallel reflections observed within the older buried levee flank.

IN-SITU TEMPERATURE MEASUREMENTS

Temperature gradients and heat flow were determined using three downhole measurements and the bottom-water (mud-line) temperature. An ADARA measurement was attempted in Hole 931B during Core 931B-6H (48.3 mbsf), but the tool failed. Another ADARA measurement was made during Core 931B-8H (67.3 mbsf) using instrument number 12. The mud-line temperature of 2.46°C measured from this instrument, obtained during Core 931B-6H, was used as the reference bottom-seawater temperature at Site 931. A successful measurement resulted in an extrapolated equilibrium temperature of 5.47°C. The WSTP tool was deployed at three depths in Hole 931B. A WSTP measurement was attempted before Core 931B-11X (84.3 mbsf), but the tool failed. Two WSTP measurements were made before Cores 931B-13X (103.5 mbsf) and -17X (142.2 mbsf) using probe thermistor number 108. These measurements provided high-quality data yielding extrapolated equilibrium temperatures of 6.2°C and 7.34°C, respectively. We applied a correction of +1286 Ω to the raw resistance values recorded by the WSTP data logger to correct for the difference in mud-line temperature recorded by the WSTP tool relative to that of the ADARA tool.

Equilibrium temperatures, extrapolated from synthetic curves constructed to fit transient temperature data, are plotted as a function of depth (mbsf) in Figure 40. Using the ADARA mud-line temperature, and the sub-bottom temperatures from the one ADARA and two WSTP measurements downhole, the geothermal temperature gradient can be approximated by a linear mean of 34°C/km. We calculated heat flow by adopting the constant geothermal temperature gradient of 34°C/km and a thermal conductivity, K (as determined by the physical properties analyses), of 1.25 ± 0.15 W/(m·K), which corresponds to the average depth of 100 mbsf. This results in a calculated heat flow of 42.5 mW/m^2.

Depending on which data points are used, the geothermal gradient varies. Using the ADARA mud-line temperature and the one ADARA measurement at 63.7 mbsf, the geothermal gradient is 44.7°C/km (Fig. 40). If we use the ADARA temperature at 63.7 mbsf, and the two lower temperatures from the WSTP measurements (Fig. 40), the geothermal gradient is 24.99°C/km.

SYNTHESIS AND SIGNIFICANCE

Stratigraphic Synthesis

Surficial Nannofossil-rich Clay (Unit I)

As at Site 930, 0.57 m of brown calcareous clay containing foraminifers and nannofossils (Fig. 41) overlies a brown diagenetic crust. The age and interpretation of this unit are discussed in the Site 930 chapter.

Mud and Turbidite Silt Overlying Channel-levee System 5 (Subunits IIA and IIB)

Subunit IIA (0.57–6.70 mbsf) consists of bioturbated and color-banded mud and overlies Subunit IIB (6.70–27.50 mbsf), which contains mud with <20% silt laminae, interpreted to be turbidites. These two subunits form a fining-upward sequence of sediment, and lithologically resemble Subunits IIA and IIB in Site 930. They correspond to the Amazon through Yellow Channel-levee System on the western part of the Amazon Fan.

Levee Crest of Channel-levee System 5 (Subunit IIC, Upper Part)

The upper part of Subunit IIC (27.50 to about 130 mbsf) corresponds to the crest of the levee of Channel-levee System 5 and comprises mud with thin to thick beds of silt and fine sand, which increase in frequency and thickness toward the base of the subunit. The gradual increase in sand from Subunit IIA to the base of the levee sequence is reflected in a gradual increase in magnetic susceptibility. The sediment in this interval shows at least two cycles of variation in resistivity, with sharp bases and a gradual upward decrease in resistivity that is probably related to sediment fabric.

HARP Sequences of Sand and Lesser Mud (Subunit IIC, Lower Part, and Unit III, Upper Part)

Seismic data indicate the presence of three HARP units, which correspond to zones of low recovery in the lower 70 m of Subunit IIC (130–199.8 mbsf) and the upper part of Unit III (199.8–(?)257.7 mbsf). The precise depth of the top of the underlying debris-flow deposit is uncertain. Sediment recovered in this interval includes abundant sand beds, the thickest of which contain mud clasts, interbedded with mud with silt laminae. Log data indicated two major sequences in which sand abundance decreases upward (fining-upward cycles), with their bases at 198 mbsf and 158 mbsf, and a third (lower) sequence without a pronounced grain size trend. Individual sand packets up to several meters thick appear separated by muddier units. Sand in the lower two sequences includes abundant wood fragments. Mud from the lowest sequence contains continental slope benthic foraminifers.

Mass-flow Deposit (Unit III, Lower Part)

The lower part of Unit III [(?)257.8–349.25 mbsf] consists of various types of overconsolidated mud. In places, these clearly occur as

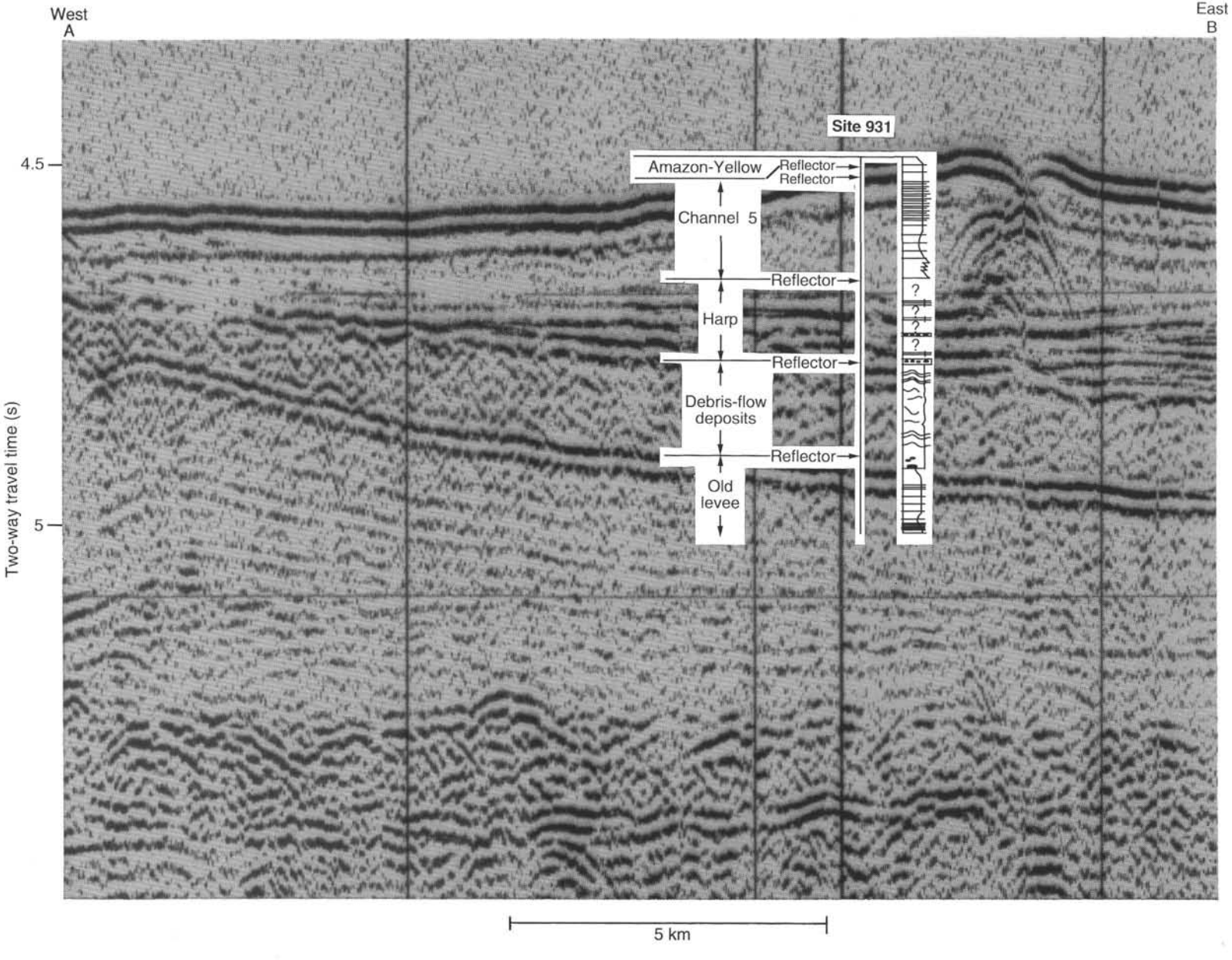

Figure 35. *JOIDES Resolution* single-channel seismic profile across Site 931 with corresponding lithostratigraphic section at Hole 931B. Location of profile in Figure 1 (see Fig. 3).

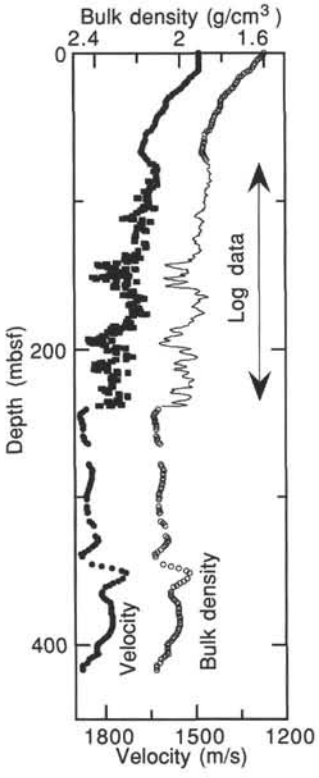

Figure 36. Composite (downhole log and laboratory) velocity and density.

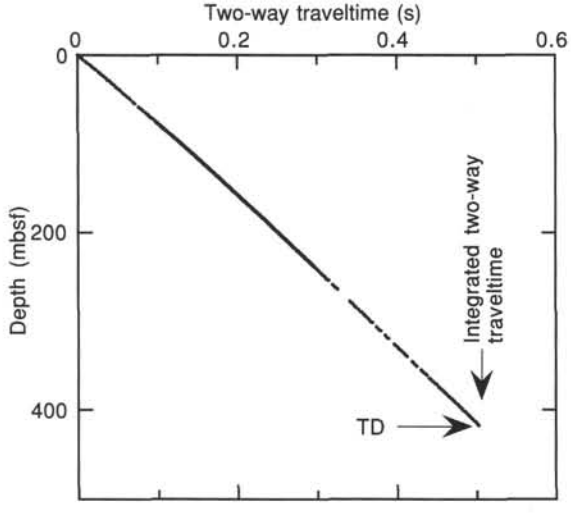

Figure 37. Velocity vs. depth plot for Hole 931B derived from the downhole log and discrete laboratory density measurements (see Table 10 of "Explanatory Notes" chapter, this volume).

clasts, some of which consist of foraminifer- and nannofossil-rich clay. The lowermost clasts in the mass-flow deposit have microfossil assemblages similar to those in the underlying Units IV and V. Unlike in the debris-flow deposit in Site 930, all benthic foraminifers are deep water species such as *Uvigerina*. The [C/N]a ratio in sediment from 300 to 349 mbsf is distinctly higher than elsewhere in the hole.

Middle Pleistocene Interglacial Foraminifer-Nannofossil Clay (Unit IV)

This thin unit (349.25–349.46 mbsf) consists of a highly bioturbated dark gray foraminifer-nannofossil clay with <35% carbonate. This unit contains warm-water foraminifers and may be analogous to the Holocene carbonate clay at the top of the hole, thus reflecting an earlier interglacial highstand of sea level.

Top of a Levee in the Bottom Levee Complex (Unit V)

Unit V (349.46–421.3 mbsf) consists of a sequence of sediment types similar to Subunits IIA and IIB, with bioturbated and color-banded mud (Subunit VA, to 360.87 mbsf) overlying mud with silt laminae (Subunit VB).

Implications

The Lake Mungo Excursion (about 30 ka) was detected at 76.5 mbsf. The first occurrence of *P. obliquiloculata* below the Holocene is at 238.4 mbsf, near the top of the Unit III debris-flow deposit, into which it may have been reworked. Furthermore, foraminifer abundances are very low from 90 to 238 mbsf, so the *P. obliquiloculata* zonal marker (about 40 ka) may not have been detected.

In autochthonous sediment of Unit IV and the upper 5 m of Unit V, the foraminiferal assemblage is interglacial. The nannofossils are of Zone CN14b (0.26–0.46 Ma).

Downhole variations in mud mineralogy (determined by XRD) are difficult to interpret because of grain-size effects. Clay-mineral abundance relative to quartz is lowest from 100 to 350 mbsf. High kaolinite/illite ratio occurs locally in Unit II between 30 and 100 mbsf, in a carbonate-rich clay clast in Unit III, and in Unit V.

Magnetic susceptibility data show a small-scale correlation with silt-mud alternations, but also show a longer-period variation over tens of meters that correlates with variations in illite to quartz ratio from XRD data. Susceptibility measured with the GHMT logging tool shows a strong correlation with log indicators of sand/mud ratio such as natural gamma radiation and aluminum content.

The sedimentological character of the turbidite sequences is similar to that discussed in detail at Site 930. At this site, evidence of cyclic deposition was clearer. Wireline logs suggest that the two fining-upward HARP units comprise fining-upward cycles, with the upper cycle continuing upward into the levee of Channel-levee System 5. This entire levee sequence forms the upper part of this cycle, with an overall decrease in the abundance and thickness of both sand and silt beds. Within this trend, there are some short intervals of coarser sediment (e.g., 8–10 and 70–76 mbsf). Other levee sites (e.g., Site 930) have also shown irregular fluctuations in the abundance of silt and sand. The relationship of these smaller-scale variations in turbidites to the resistivity variations noted in the upper 120 mbsf is unclear.

A detailed pore-water profile was made in Hole 931C. It showed pronounced peaks in alkalinity and phosphate at 6 mbsf, with phosphate decreasing to background values by 10 mbsf just below complete sulfate reduction. Pore-water iron concentration peaks at 12–16 mbsf. These distributions suggest that once iron is no longer being removed as sulfide, it is precipitated as vivianite (iron phosphate). Maximum methane concentrations were observed between 35 and 65 mbsf. Total organic carbon averages 1.0% in the upper part of the hole, steadily decreasing to about 0.8% near the base of the hole. High methane concentrations were also found in the bottom two cores of the hole. The C/N ratio is abruptly higher from about 300 to 349 mbsf, corresponding to the lower part of the mass-flow Unit III. As in Site 930, elevated total sulfur (>1%) occurs in some blocks in the mass-flow deposit (315–317 mbsf), but unlike Site 930, elevated total nitrogen values are not found.

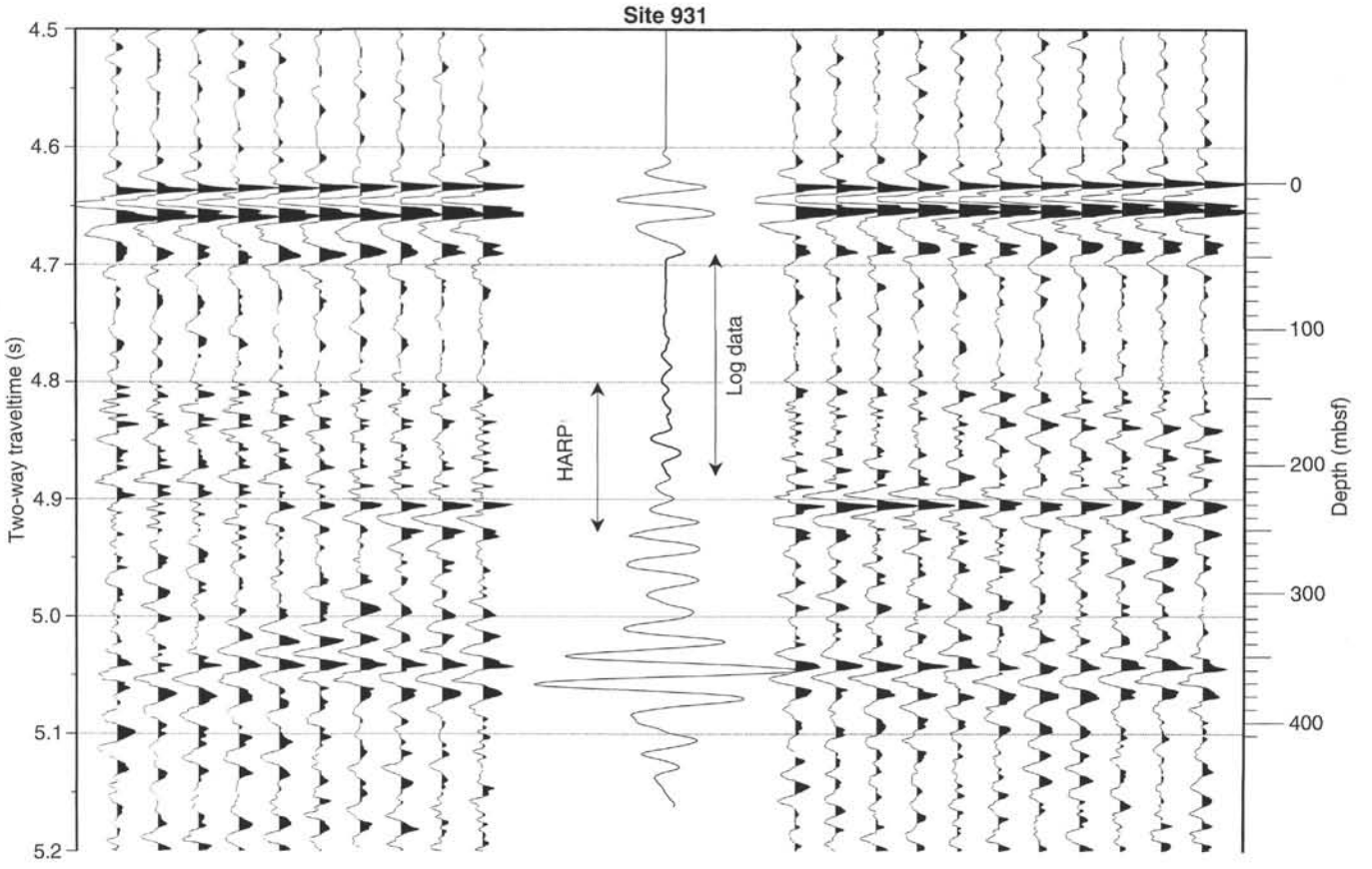

Figure 38. Synthetic seismogram for Site 931.

Units I and II show variations in porosity and bulk density that suggest normal consolidation. Many of the blocks in Unit III appear over-consolidated. Unit V shows profiles that suggest normal consolidation, but their water content is rather high for the depth of burial, which may indicate that the debris flow acted as a seal.

REFERENCES*

Damuth, J.E., 1977. Late Quaternary sedimentation in the western equatorial Atlantic. *Geol. Soc. Am. Bull.*, 88:695–710.

Damuth, J.E., Flood, R.D., Kowsmann, R.O., Belderson, R.H., and Gorini, M.A., 1988. Anatomy and growth pattern of Amazon deep-sea fan as revealed by long-range side-scan sonar (GLORIA) and high-resolution seismic studies. *AAPG Bull.*, 72:885–911.

Damuth, J.E., Kowsmann, R.O., Flood, R.D., Belderson, R.H., and Gorini, M.A., 1983. Age relationships of distributary channels on Amazon deep-sea fan: implications for fan growth pattern. *Geology*, 11:470–473.

Flood, R.D., Manley, P.L., Kowsmann, R.O., Appi, C.J., and Pirmez, C., 1991. Seismic facies and late Quaternary growth of Amazon submarine fan. *In* Weimer, P., and Link, M.H. (Eds.), *Seismic Facies and Sedimentary Processes of Submarine Fans and Turbidite Systems:* New York (Springer-Verlag), 415–433.

Manley, P.L., and Flood, R.D., 1988. Cyclic sediment deposition within Amazon deep-sea fan. *AAPG Bull.*, 72:912–925.

Manley, P.L., Pirmez, C., and Flood, R.D., 1988. Spatial depositional pattern for the Amazon deep-sea fan. *In* Nittrouer, C.A., and DeMaster, D.J. (Eds.), *Chapman Conference on the Fate of Particulate and Dissolved Components Within the Amazon Dispersal System: River and Ocean:* Washington (American Geophysical Union), 163–167.

Nesbitt, H.W., and Young, G.M., 1984. Prediction of some weathering trends of plutonic and volcanic rocks based on thermodynamics and kinetic considerations. *Geochim. Cosmochim. Acta*, 48:1523–1534.

Stein, R., 1991. *Accumulation of Organic Carbon in Marine Sediments:* Berlin (Springer).

Taylor, S.R., and McLennan, S.M., 1985. *The Continental Crust: Its Composition and Evolution:* Oxford (Blackwell Scientific).

*Abbreviations for names of organizations and publications in ODP reference lists follow the style given in *Chemical Abstracts Service Source Index* (published by American Chemical Society).

Ms 155IR-107

NOTE: For all sites drilled, core-description forms ("barrel sheets") and core photographs can be found in Section 4, beginning on page 703. Forms containing smear-slide data can be found in Section 5, beginning on page 1199. GRAPE, index property, magnetic susceptibility, and natural gamma data are presented on CD-ROM (back pocket).

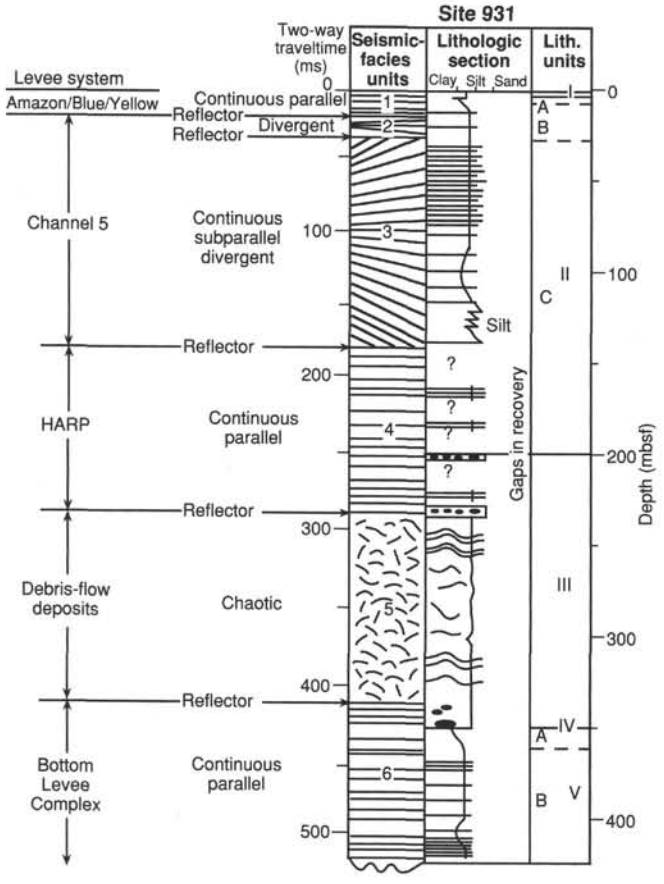

Figure 39. Correlation of lithostratigraphy with seismic-facies units and prominent reflections (arrows) at Site 931.

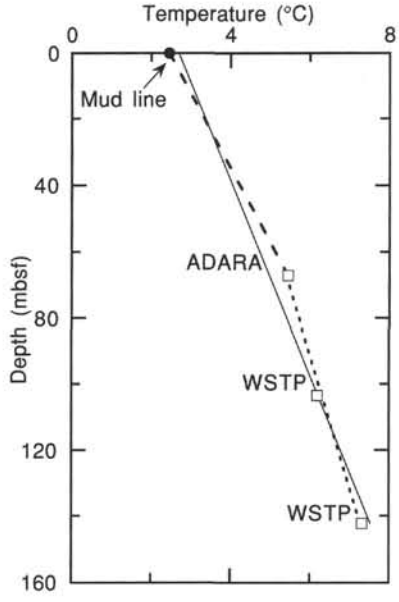

Figure 40. Estimated equilibrium temperatures in Hole 931B. A linear curve fit (solid line) through the data suggests that reliable equilibrium temperatures were acquired that indicate a geothermal gradient of 34.03°C/km. A geothermal temperature gradient of 44.7°C/km is calculated (dashed line) by using the ADARA mud-line temperature, and the one ADARA measurement at 63.7 mbsf. A geothermal temperature gradient of 24.99°C/km is calculated (dotted line) by using the one ADARA measurement at 63.7 mbsf and the two lower WSTP measurements.

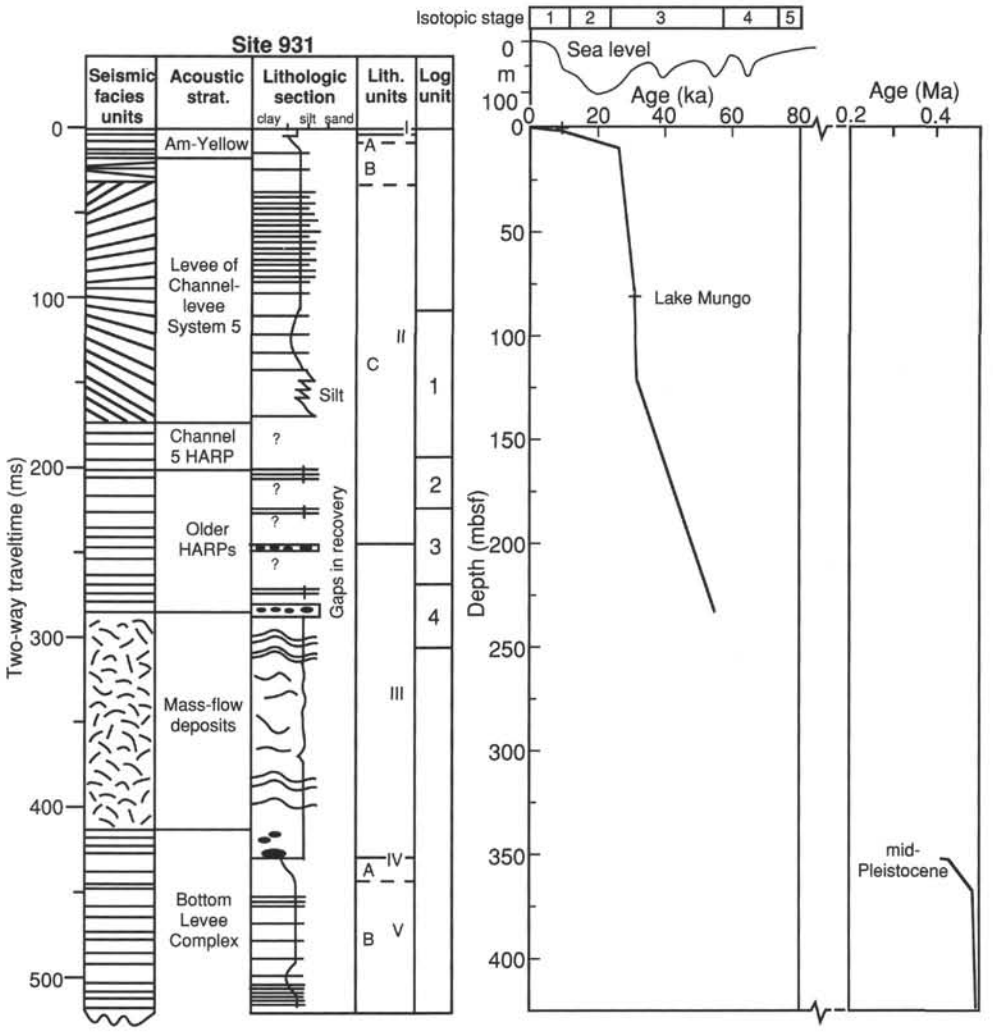

Figure 41. Summary of Site 931 showing seismic-facies units, acoustic stratigraphy, schematic lithologic column, lithologic units, log stratigraphic units, chronological picks, and interpreted age-depth curve.

SHORE-BASED LOG PROCESSING

HOLE 931B

Bottom felt: 3486.7 mbrf
Total penetration: 421.3 mbsf
Total core recovered: 296.05 m (70.3%)

Logging Runs

Logging string 1: DIT/LSS/HLDT/CNTG/NGT
Logging string 2: FMS/GPIT/NGT (two passes)
Logging string 3: ACT/GST/NGT
Logging string 4: GHMT/NGT (two passes)
Wireline heave compensator was used to counter ship heave.

Bottom-hole Assembly

The following bottom-hole assembly depths are as they appear on the logs after differential depth shift (see **Depth shift** section below) and depth shift to the seafloor. As such, there might be a discrepancy with the original depths given by the drillers on board. Possible reasons for depth discrepancies are ship's heave, use of wireline heave compensator, and drill-string and/or wireline stretch.

DIT/SDT/HLDT/CNTG/NGT: Bottom-hole assembly at 93 mbsf
ACT/GST/NGT: Bottom-hole assembly at 74 mbsf
FMS/GPIT/NGT: Bottom-hole assembly at 92 mbsf (main pass)
FMS/GPIT/NGT: Recorded open hole (repeat pass)
GHMT/NGT: Both passes recorded open hole

Processing

Depth shift: All original logs have been interactively depth shifted with reference to NGT from the ACT/GST/NGT run, and to the seafloor (–3483.5 mbrf). This value does not correspond to the drillers' water depth ("bottom felt") but to the depth of the seafloor as seen on the logs. A list of the amount of differential depth shifts applied at this hole is available upon request.

Gamma-ray processing: NGT data have been processed to correct for borehole size and type of drilling fluid.

Acoustic data processing: No processing necessary due to the good quality of the logs.

Geochemical processing: (For detailed explanation of the processing, please refer to the "Explanatory Notes" chapter, this volume, or to the "geochem.doc" file on the CD-ROM enclosed in the back pocket). The elemental yields recorded by the GST tool represent the relative contribution of only some of the rock-forming elements (iron, calcium, chlorine, silica, sulfur, hydrogen, gadolinium, and titanium—the last two computed during geochemical processing) to the total spectrum. Because other rock-forming elements are present in the formation (such as aluminum, potassium, etc.), caution is recommended in using the yields to infer lithologic changes. Instead, ratios (see "acronyms.doc" on CD-ROM) are more appropriate to determine changes in the macroscopic properties of the formation. A list of oxide factors used in geochemical processing includes the following:

$SiO_2 = 2.139$
$CaCO_3 = 2.497$
$FeO^* = 1.358$
$TiO_2 = 1.668$
$K_2O = 1.205$
$Al_2O_3 = 1.889$

FeO* computed using an oxide factor that assumes a 50:50 combination of Fe_2O_3 and FeO factors.

Quality Control

During the processing, quality control of the data is mainly performed by cross-correlation of all logging data. Large (>12 in.) and/or irregular borehole affects most recordings, particularly those that require eccentralization and a good contact with the borehole wall (CNTG, HLDT).

Hole diameter was recorded by the hydraulic caliper on the HLDT tool (CALI), and the caliper on the FMS string (C1 and C2).

Data recorded through bottom-hole assembly, such as the CNTG and NGT data above 93 mbsf, should be used only qualitatively because of the attenuation on the incoming signal.

Invalid gamma-ray spikes were recorded at 79 and 84–85 mbsf during the DIT/SDT/HLDT/CNTG/NGT run and at 44.5 and 50.5 mbsf during the ACT/GST/NGT run.

FACT = quality control curve in geochemical processing. Accuracy of the estimates is inversely proportional to the magnitude of the curve.

Note: Details of standard shore-based processing procedures are found in the "Explanatory Notes" chapter, this volume. For further information about the logs, please contact:

Cristina Broglia
Phone: 914-365-8343
Fax: 914-365-3182
Email: chris@ldeo.columbia.edu

Elizabeth Pratson
Phone: 914-365-8313
Fax: 914-365-3182
Email: beth@ldeo.columbia.edu

931B Geochemical Logging Data

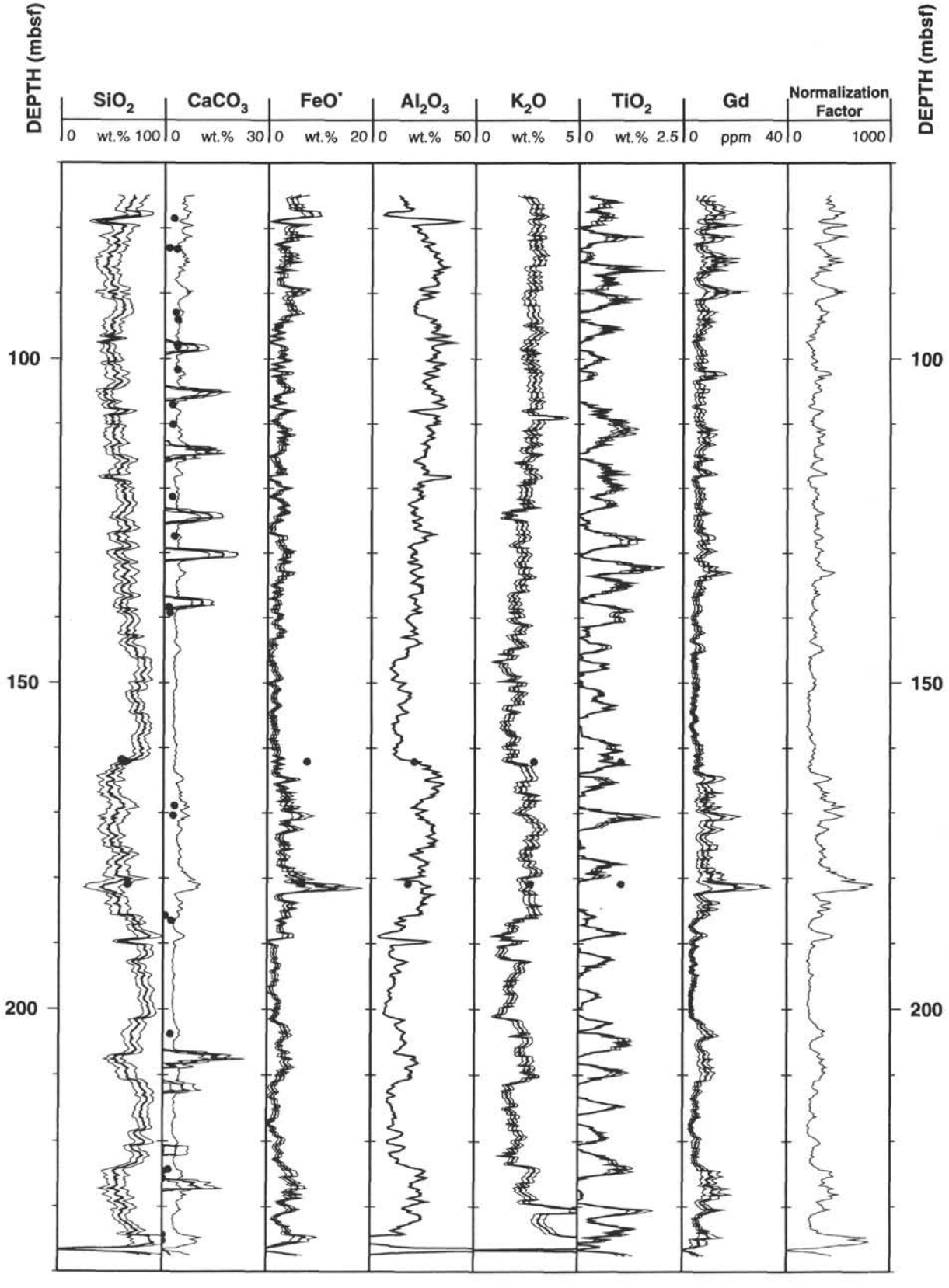

931B Natural Gamma Ray Logging Data

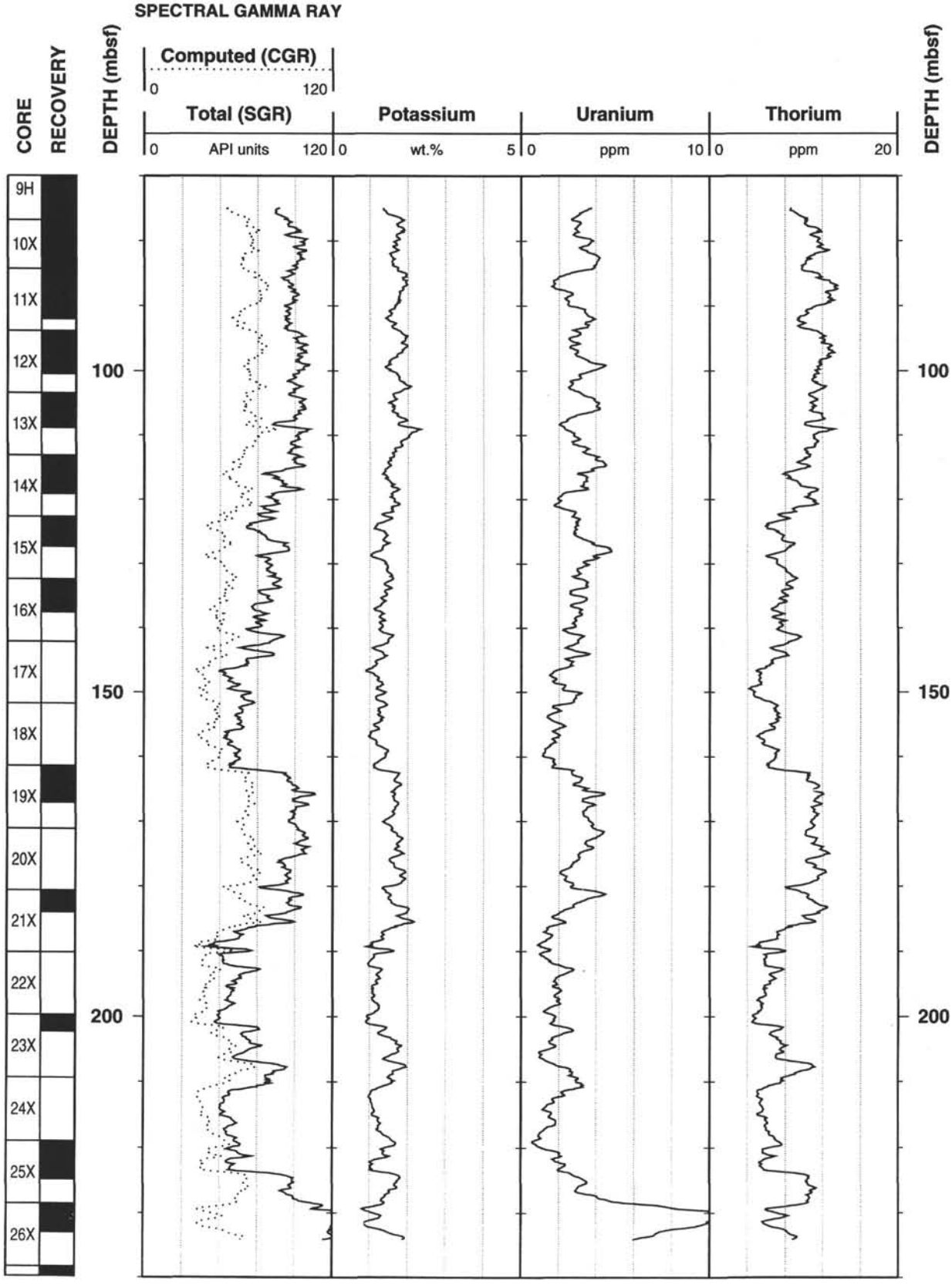

931B Natural Gamma Ray-Resistivity-Sonic Logging Data

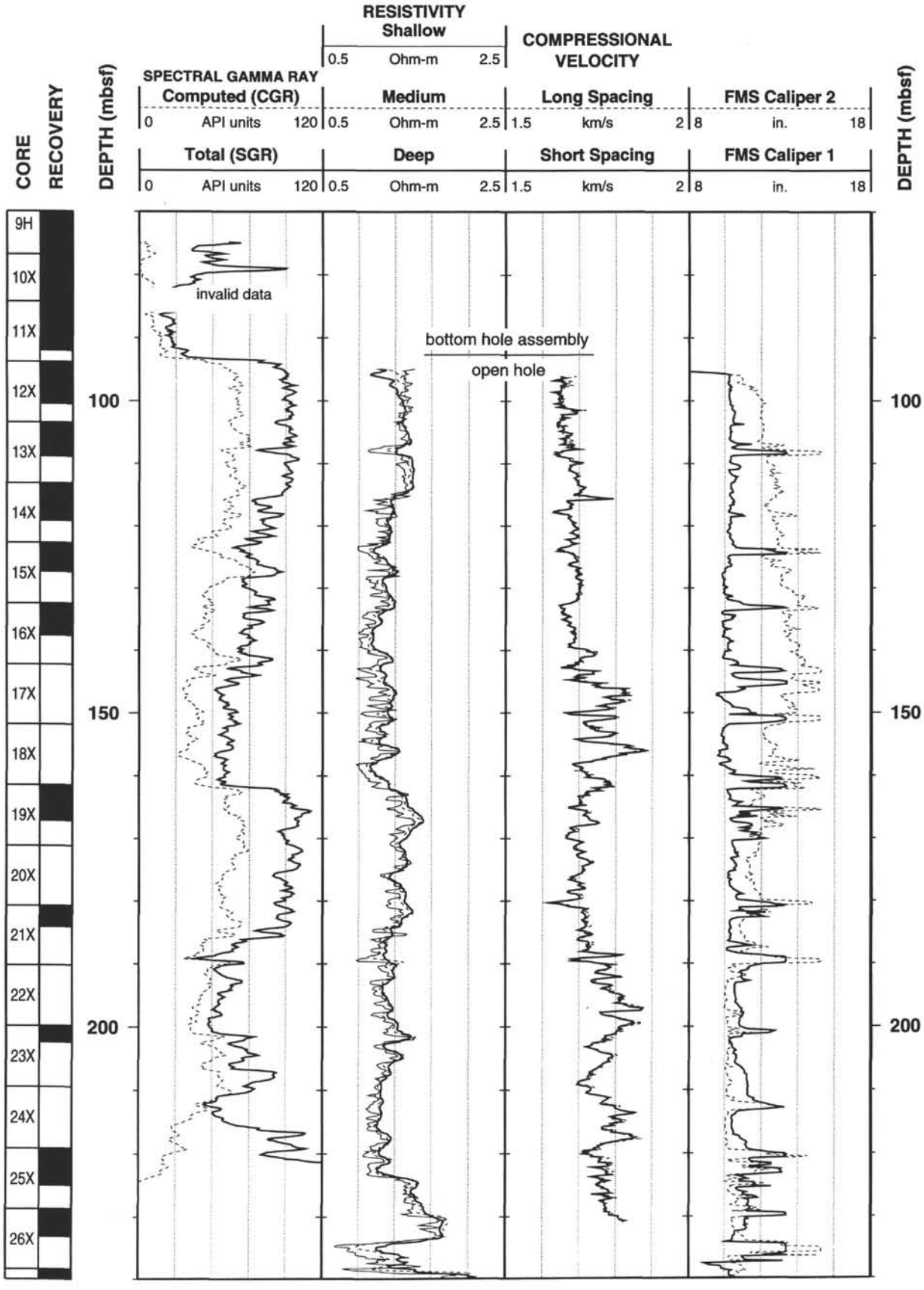

931B Natural Gamma Ray-Resistivity-Sonic Logging Data (cont.)

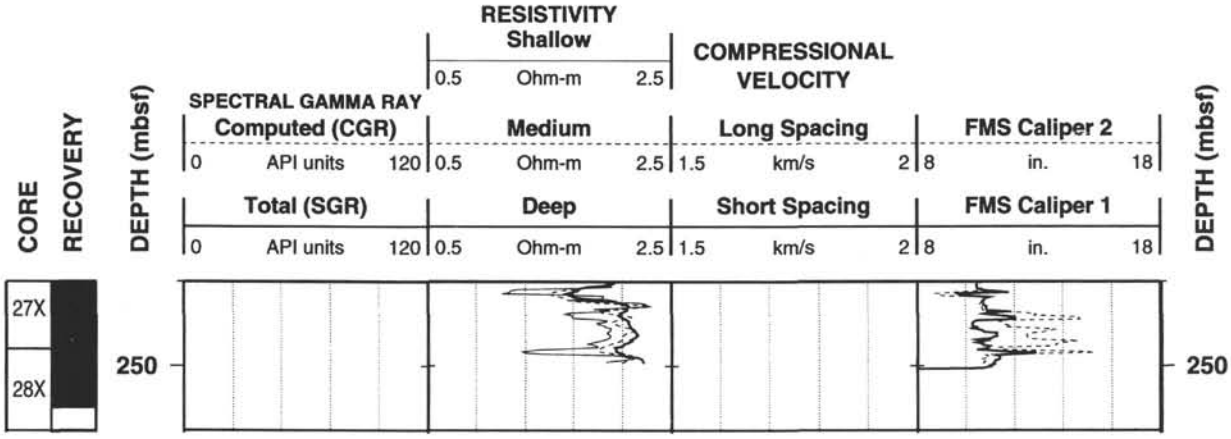

931B Natural Gamma Ray-Density-Porosity Logging Data